OPTICAL AND ELECTRICAL PROPERTIES OF ORGANIC SEMICONDUCTORS: EXPERIMENT AND SIMULATION

by

Xialing Chen

Bachelor of Science, University of Science and Technology of China, 2007

Submitted to the Graduate Faculty of

The Dietrich School of Arts and Sciences in partial fulfillment

of the requirements for the degree of

Doctor of Philosophy

University of Pittsburgh

2015

UNIVERSITY OF PITTSBURGH

Dietrich School of Arts and Sciences

This dissertation was presented

by

Xialing Chen

It was defended on

January 7th, 2014

and approved by

David Waldeck, Professor, Department of Chemistry

Alexander Star, Associate Professor, Department of Chemistry

Minhee Yun, Associate Professor, Department of Electrical and Computer Engineering

Dissertation Advisor: Geoffrey R Hutchison, Associate Professor, Department of Chemistry

**OPTICAL AND ELECTRICAL PROPERTIES OF ORGANIC SEMICONDUCTORS:
EXPERIMENT AND SIMULATION**

Xialing Chen, PhD

University of Pittsburgh, 2015

This dissertation focuses on the charge transport of organic semiconductors, particularly in the presence of traps and defects. Rather than attempting to ultimately pure materials, intentional mixtures were made and studied. The materials were characterized by electrochemistry, UV/Vis spectroscopy and computational studies using density functional theory (DFT) and time dependent DFT (TDDFT).

In experiment, the phthalocyanine films were prepared from solution. We explored how to improve the coatings of organic semiconductors on different substrates. Moreover, the effect of how intentionally introduced traps or barriers change the charge transport was studied using the spin-coated octabutoxy phthalocyanine and naphthalocyanine mixed films. It was found that the introduced barriers decreased the mobility. And a negative differential resistance was observed in the saturated region of the Field-effect-transistor (FET) measurements in the mixed films.

In simulation, density functional theory (DFT) and time-dependent density functional theory (TDDFT) calculations were performed to predict optical and electrical parameters of the semiconducting materials. In the calculations of phthalocyanine molecules with different metal or ligand substitutions, it was found that the electrical and optical properties of the phthalocyanine semiconductors could be tuned more with different organic ligands than by modifying the metal centers. For the mixed valence (MV) bipyridine bridged triarylamine systems, the simulation perfectly predicted the absorption of the spectra and the blue-shift of the spectra with different solvents reported by our collaborator in experiments.

TABLE OF CONTENTS

LIST OF TABLES

LIST OF FIGURES

PREFACE

I would never be able to finish my PhD without the professional guidance from my committee members, valuable advice from my research group and support from my family and my husband.

I would like to express my deep gratitude towards my advisor, the dearest Dr. Hutchison, for his excellent guidance, patience, caring, free but strict science research environment in the group. Whenever there was difficulty with a technique, he was always there willing to help. For a long time without progress, he did not blame but encouraged me to try and improve. He is such a good advisor that every one of us in the group likes him both as a research advisor and a dear friend. I would also like to thank Dr. Star and Dr. Yun for the advice and help on my research project. I could never finished one of my projects without the spin-coater from Dr. Star`s group. As for Dr. Yun, during the first year of my PhD, I went to his group several times to learn how to fabricate the semiconductor devices and got lots of useful advice from himself and several of his graduate students. A special thanks goes to Dr. Waldeck. He has been the committee member of all the milestones in my PhD: comprehensive, proposal and defense. He spent lots of time teaching me how to write a good grant proposal, which is a really valuable experience for me.

There is another faculty member I need to express my thanks: Professor Yuwu Zhong in Chinese Academy of Sciences, with whom we collaborated on the mixed valence project.

I would like to thank all the group members, especially to Xinfeng Quan, Adam G Gagorik and Paula B Hoffmann, with whom I collaborated some of the projects.

Personally, I have to thank my parents in China, who raised me up, financially supported me in college and have been always encouraging me and backing me up. I also want to thank my brother for his support to his sister and my husband Zhouchun Huang, an industrial engineering

1.0   INTRODUCTION

There has been tremendous interest in organic semiconductors since the 1970s[1] because of many applications in organic light emitting diodes (OLEDs),[2] thin film transistors (TFTs),[3] solar cells,[4] photovoltaic,[5] etc. Compared to inorganic semiconductors, organic materials have advantages in solution processability,[6] synthetic tailorability,[7] and flexibility, all of which makes it quite promising to be fabricated on flexible substrates from solution for cheaper and rollable electronic devices. At this moment, there have already been commercialized OLEDs[8] for displays, and organic photovoltaic[9] grids or stations to collect solar energy. Organic semiconducting materials are still under-developed compared to the inorganic counterparts, mainly because of the limited efficiency; however, the efficiency[10] has been greatly improved through the effect made in academia and industry. For example, as shown in Figure 1.1, the efficiency of the organic solar cells increases from 4% to 12% in the past 10 years, and it suggests continued improvement.

For inorganic crystalline semiconductors such as Si, Ge, GaAs, the crystal structure is formed through covalence versus ionic interactions, and the electronic structure consists of the valence band and conduction band separated by a forbidden gap as illustrated in Figure 1.2. Electrons constrained in the valence band cannot move freely until they are excited to the conduction band by thermal or photon assisted excitation. The example of some popular inorganic semiconductors and their bandgaps are listed in Table 1.1.
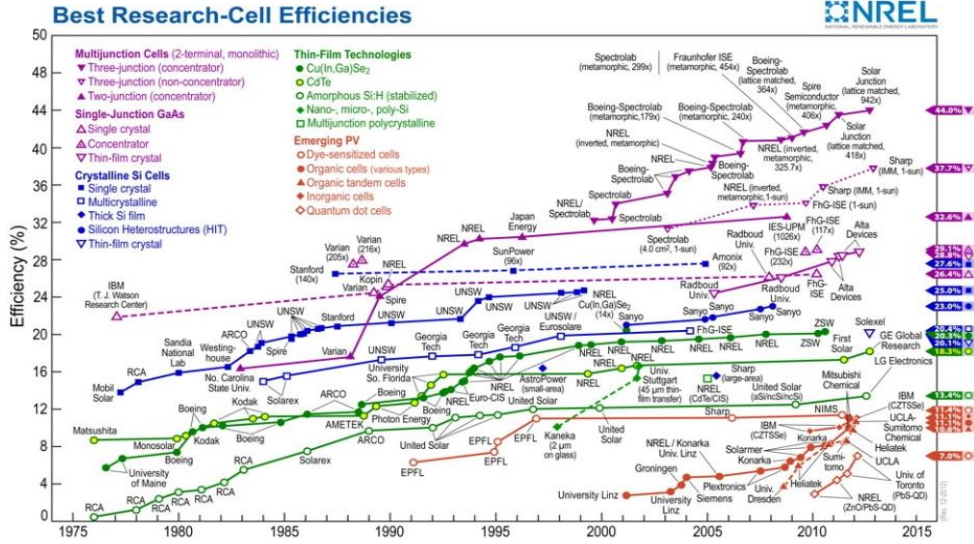
Figure 1.1. The summary of the different solar cell efficiency (from Ref. 9) reports given by National Center for Photovolatics in 2013.
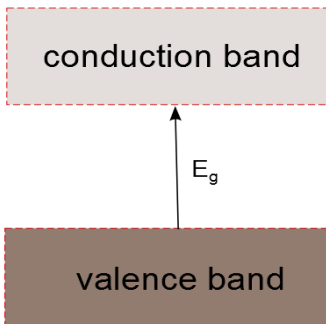
Figure 1.2 A schematic of the electronic band structure in a typical inorganic semiconductor. E_g is the band gap, or the energy an electron needs to jump from the valence band to the conduction band.

Table 1.1. Selected examples of inorganic semiconductors and their bandgaps.

Material	Bandgap (eV) @ 300K
Si	1.11
Ge	0.67
Se	1.74
GaAs	1.43
GaN	3.4
CdSe	1.73
ZnO	3.37

Compared to the well understood inorganic semiconductors, the mechanism of charge transport in organic semiconductors is still under-explored. In some organic semiconductor films such as pentacene[11] and rubrene, it was reported that they display bandlike transport mobility of $\mu \sim T^{-n}$ (n>0). However, this is only applicable to highly purified crystalline organic semiconductors of excellent charge transport efficiency with mobility greater than $10\ cm^2/(V.s)$. For most organic semiconductors, due to the weak van der Waals interaction and sensitivity to impurity, the mobility of charge transport is much smaller than the inorganic materials and deviate from the band theory.

Among the many theories, thermal assisted hopping is the most popular to describe how charge transports in organic semiconductors. In the disordered semiconductor films from solution, the charge carriers are assumed to be localized, and the energy distribution obeys a Gaussian law:

$$g(E) = \frac{N}{\sqrt{2\pi}\sigma}\exp(-\frac{E^2}{2\sigma^2})$$

, where N is the number of charge carriers, and σ is the standard deviation of the Gaussian distribution. It is called the Gaussian Disorder Model (GDM),[12] and the charge transport occurs

via hopping between the neighboring sites. The hopping rate v_{ij} for a charge to jump from site i to site j can be described using the Miller-Abrahams[12] formula:

$$v_{ij} = v_0 \exp(-2\gamma\Delta R_{ij}) \begin{cases} 1 & \varepsilon_j < \varepsilon_i \\ \exp(-\frac{\varepsilon_j-\varepsilon_i}{k_B T}) & \varepsilon_j > \varepsilon_i \end{cases} \tag{1.1}$$

, where v_0 is a prefactor; γ is the inverse localization length; R_{ij} is the distance between site i and j; ε_i and ε_j are the energy of the site i and j, respectively; k_B is the Boltzmann constant; and T is the temperature. The first exponential component depicts the tunneling contribution while the second term is for the thermal activation. If the electron or hole jumps from a high energy site to a low energy site, the probability is 1. Otherwise, an exponential Boltzmann correction would be needed. We can see from formula (1.1) that the hopping rate depends on both the positions and energies of the localized states, which means that the charge transport should be affected both by the crystal structure and the energetic distribution of the charge carriers.

A more commonly used formula is based on the classical Marcus Hush theory,[13] where the charge transfer rate is described in terms of the electronic coupling element V and reorganization energy λ.

$$k = \frac{V^2}{\hbar}[\frac{\pi}{\lambda k_B T}]^{1/2} exp[-\frac{(\varepsilon_j-\varepsilon_i+\lambda)^2}{4\lambda k_B T}] \tag{1.2}$$

In Equation 1.2, k_B is Boltzmann constant; T is the temperature; $\hbar$ is the Planck`s constant; and ε_i and ε_j are the energy of the site i and j, respectively,

Hopping is a thermal assisted charge transfer process and the mobility increases with temperature. This was observed in experiments[14] with a trend of $\ln\mu \sim (-\frac{1}{T})$ reported. One popular modification to hopping theory is the variable range hopping theory (VRH),[15] where the

path length (d_{VRH}) of the neighboring hopping sites varies with temperature as $d_{VRH} \sim T^{-1/4}$. It indicates that the charge transport can occur to non-nearest neighbors, but the probability of long-range jumps drops off exponentially with temperature.

However, it is interesting that in some single crystalline organic semiconductors, for example, the rubrene explored by Gershenson,[16] the mobility increases with temperature at low temperature and decreases at high temperature. They attributed the complex temperature behavior to the existence of impurities in the film. At first, there were significant amount of impurities in the film, and it showed the localized charge transport performance. However, after all the traps were filled in, the charge transports in a band-like way similar to the single crystal inorganic semiconductors.

Besides the temperature dependence, crystal structure is also critical in affecting the performance of organic semiconductors. For example, charge transport would be greatly enhanced if the film aligns with a closer crystal structure and better π-π interaction.[17] Moreover, the existence of impurities significantly affects the charge transport. There are two categories of impurities. One is not conductive and called defects. The other can transport charge carriers but is of different energy levels from the normal transport sites, and are called traps or barriers. Figure 1.3 depicts how the traps and barriers influence the charge transport in organic semiconductors. In the case of electron transfer, if the impurity site is of a higher Lowest Occupied Molecular Orbital (LUMO) than the normal transport site, there would be an energy barrier to be overcome, and this kind of impurity site is called barrier site. On the contrary, if the LUMO of the impurity site is lower than the normal transport site, after the electron jumps to the impurity site, it would be trapped there as there is also an energy barrier to be overcome if it wants to jump to the next normal transport site. It is termed trap site. For the hole transport, it is the Highest Occupied Molecular Orbital (HOMO) that matters. Therefore, the trap site is with higher HOMO energy level than the normal transport

site and vice versa for the barriers. Many research groups[18] have been working hard to try to purify[19] the materials to improve the charge transport efficiency of organic semiconductors.
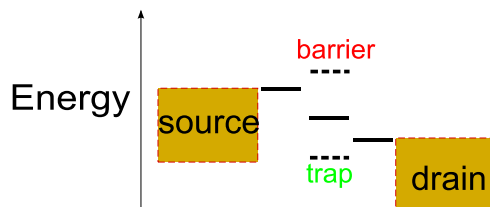
Figure 1.3. Schematic graph of how trap and barrier sites form in semiconductors

Other than the charge transport ability, we are also interested in the optoelectronic behaviors of organic semiconductors because of their vast applications in LEDs and solar cells. The efficiency η of an organic solar cell is $\eta = \frac{V_{oc} * J_{sc} * FF}{P} * 100\%$, where P is the input light intensity; V_{oc} and J_{sc} represent the open-circuit voltage and short-circuit current density, and FF is the fill factor. The open-circuit voltage is determined by the bandgap energy of the semiconductor material, and the short-circuit current is proportional to the amount of the hole-electron pairs generated. So the open-circuit voltage gets maximized with a semiconductor of big band gap, but a big bandgap always means less absorption of light and therefore a smaller current density. So a balance of these two is needed for an optimal performance and it is important to investigate the energy level and absorption spectra to predict and explore promising materials for organic LED and photovoltaic applications.

2.0 THEORETICAL STUDY OF ELECTRIC AND OPTICAL PROPERTIES OF PHTHALOCYANINES WITH DIFFERENT METAL AND LIGAND SUBSTITUTIONS

2.1 INTRODUCTION

Phthalocyanines are planar macrocyclic molecules with an aromatic phthalocyanine group. The delocalized 18π electron system makes it thermally and chemically stable. The phthalocyanines are attracting more and more interest because of the vast applications. For example, due to the strong absorption in the visible range of 600-800nm, they are widely used as a photosensitizer in photodynamic therapy[20] and dye-sensitized solar cells. [21] Moreover, the promising conductivity makes it useful in optoelectronics, such as nonlinear optical devices, [22, 23] field effect transistors, [24] thin film solar cells. [25] However, the most important reason people are interested in phthalocyanines is mainly because of two reasons. First, the unsubstituted phthalocyanines are not soluble in most solvents but with the proper peripheral substitution, they become soluble, [26] which enables low-cost solution deposition techniques. Second, the electrical[27, 28] and optical[29] behavior of the phthalocyanines can be tuned by the different metal and ligand substitutions. For example, in the work of Zhong, [28] they computationally studied the molecular orbitals, electronic absorption, IR and Raman spectra of phthalocyanines with substitutions of methoxyl or methylthio on α or β peripheral position. It was found that the electron donating methoxyl and methylthio introduction increase the HOMO and LUMO orbitals compared to the unsubstituted phthalocyanines, and the α substitution influenced the molecular structure and spectroscopic properties more than the β substitution. Meanwhile, there were also studies to elucidate the effect of modifying the metal center. For example, Chen[27] et.al theoretically studied the phthalocyanines with metals of Fe, Co,

Ni, Cu and it was reported that the metal center influences the internal reorganization and hence affects the charge transport rate. However, there has been no quantitatively work to compare the contribution of the metal and peripheral substitution.

The charge transfer rate for an electron/hole to jump to the neighboring site can be described by the Marcus Hush theory. [30] Based on equation 1.2, it can be seen that the electron transfer rate gets maximized with a large electronic coupling and small reorganization energy. The reorganization energy consists of the internal[31] contribution between neighboring transfer sites and the external contribution with the surrounding solvents and environment. In this section, we intend theoretically to understand how the internal reorganization energy is affected by different metal center and ligand substitutions in phthalocyanine and naphthalocyanine molecules. The process is depicted in Figure 2.1.

To theoretically explore the electrical and optical properties, DFT and TDDFT simulations were applied systematically to predict molecular orbitals, energy level, internal reorganization energy and electronic absorption spectra of phthalocyanines with different substitutions. In the end, the influence of metal and organic ligand substitutions is compared to discover which one tunes the electric and optical to the phthalocyanines to a larger extent. It is important and significant to guide to choose molecular candidates for applications in solar cells, LED and photovoltaics that require an extensive understanding of energy levels and optical spectra.

$$M + M^+ \rightarrow M^+ + M \hspace{4cm} (2.1)$$
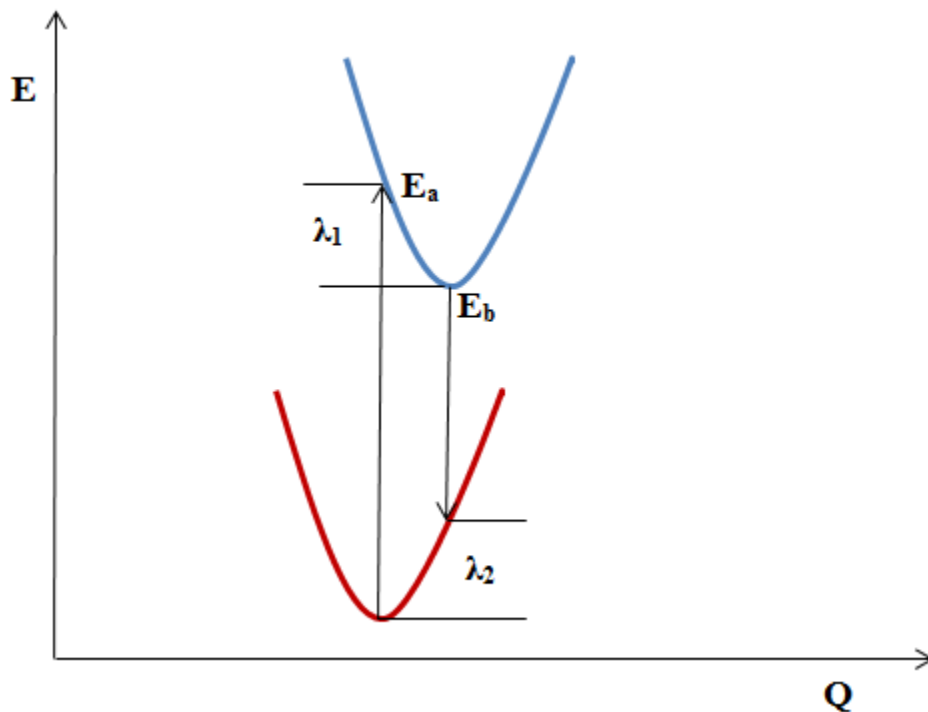
Figure 2.1. The scheme of how to calculate the internal reorganization energy of a hole transport process of Equation 2.1. The energy of point a (E_a) is the single point energy obtained from the excited state of the optimized neutral geometry. The energy of b (E_b) is the ground state energy of the optimized geometry of the +1 cationic specie. The reorganization component $\lambda_1 = E_a - E_b$. The similar scheme would be applied to calculate λ_2. The internal reorganization energy for reaction (2) will be the sum of λ_1 and λ_2.

2.2   COMPUTATIONAL METHODS
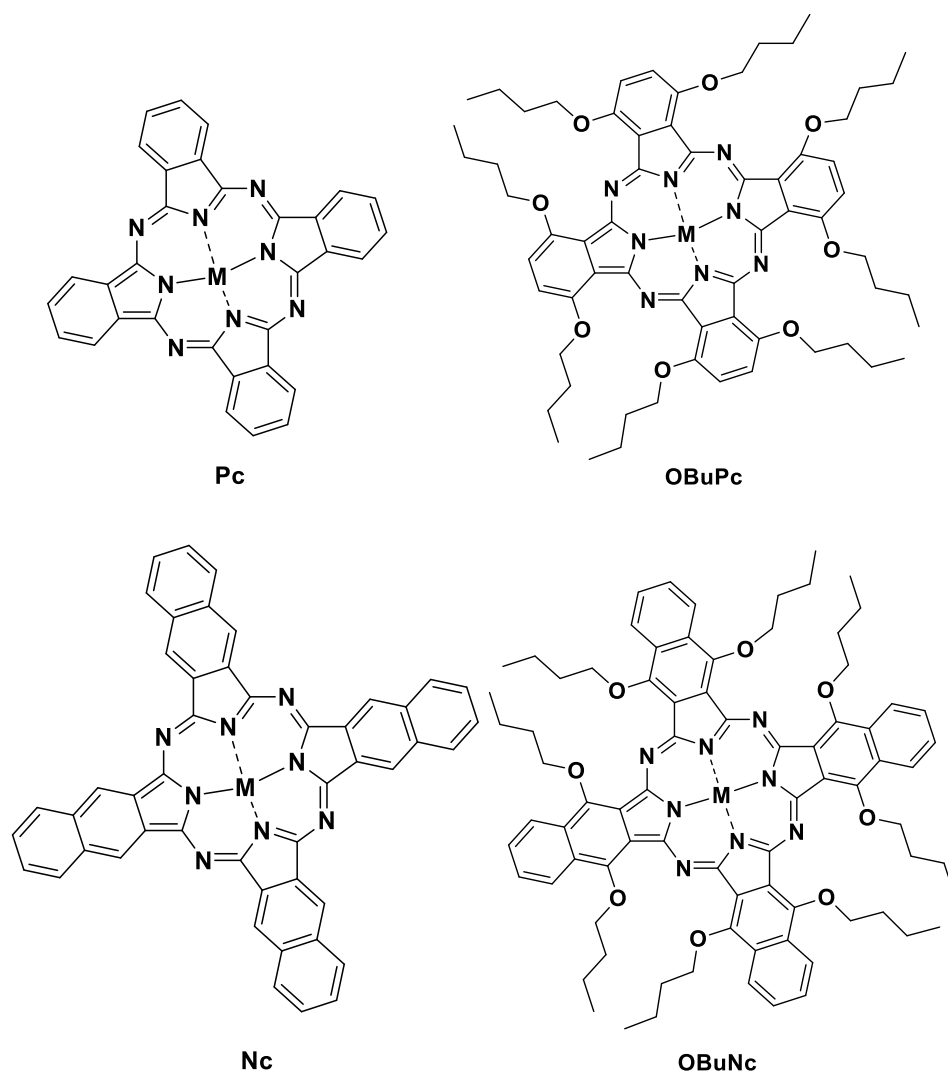
Figure 2.2 Chemical structure of phthalocyanine (Pc); 1,4,8,11,15,18,22,25-Octabutoxy-29*H*,31*H*-phthalocyanine (OBuPc); naphthalocyanine (Nc); 5,9,14,18,23,27,32,36-Octabutoxy-2,3-naphthalocyanine (OBuNc). M—metal or H$_2$

For all compounds studied, full geometry optimizations were performed using Gaussian 09, Revision D.01[32] with the B3LYP functional[33] of a 6-31G* basis set for light atoms, and the

LANL2DZ pseudopotential basis set[34] for metal atoms. An example Gaussian input file is displayed as supplementary material (Appendix A.1). Avogadro[35], version 1.0.3 was used to draw the molecules, generate input files for Gaussian simulations, and visualize the molecular orbitals. The UV-vis spectra were obtained using GaussSum[36] 3.0 by plotting the absorbance intensity with wavelength.

The energy level of HOMO, LUMO and band gap were obtained from the optimized neutral geometries. Reorganization energies were calculated as illustrated in Figure 2.1. TDDFT simulations were applied to the optimized neutral geometries to get the electronic absorption spectra. The energy level, reorganization energy and electronic absorption spectra of the phthalocyanines with various metal and ligand substitutions are examined to determine which has a bigger influence on the electrical and optical properties.

2.3   RESULTS AND DISCUSSIONS

It is found that the substitution of octabutoxy raises both the HOMO and LUMO energy level, and it is more obvious in phthalocyanine than naphthalocyanine. Naphthalocyanine is about 0.5 eV higher in HOMO energy level and 0.3 eV smaller LUMO-HOMO band gap than phthalocyanine. Different metal centers (Ni, Cu, Zn) do not tune the energy level much. They affect the LUMO energy level more than the HOMO and band gap. It agrees with the electrochemistry result reported by Arıcan, et.al[37] that different metal substitutions significantly affect the redox peaks. TiO and VO behave differently from the others and have a lower HOMO and LUMO energy levels compared to the other metals. To summarize, the metal centers do not tune the energy level as much as the ligand substitutions of phenyl or octabutoxy.

11

Visualization of the HOMO and LUMO molecular orbital (Table 2.1) can help interpret the observations. It is shown that the frontier molecular orbitals are mainly associated with the isoindole and phenyl aromatic rings, which explains why the ligand substitutions affect the energy level more than the metal centers in both the phthalocyanines and naphthalocyanines. Moreover, the VO substituted phthalocyanines have different molecular orbitals from the Cu, Ni, Zn and H_2 substituted phthalocyanines, therefore, the VO behaves differently from the other substituted phthalocyanines.
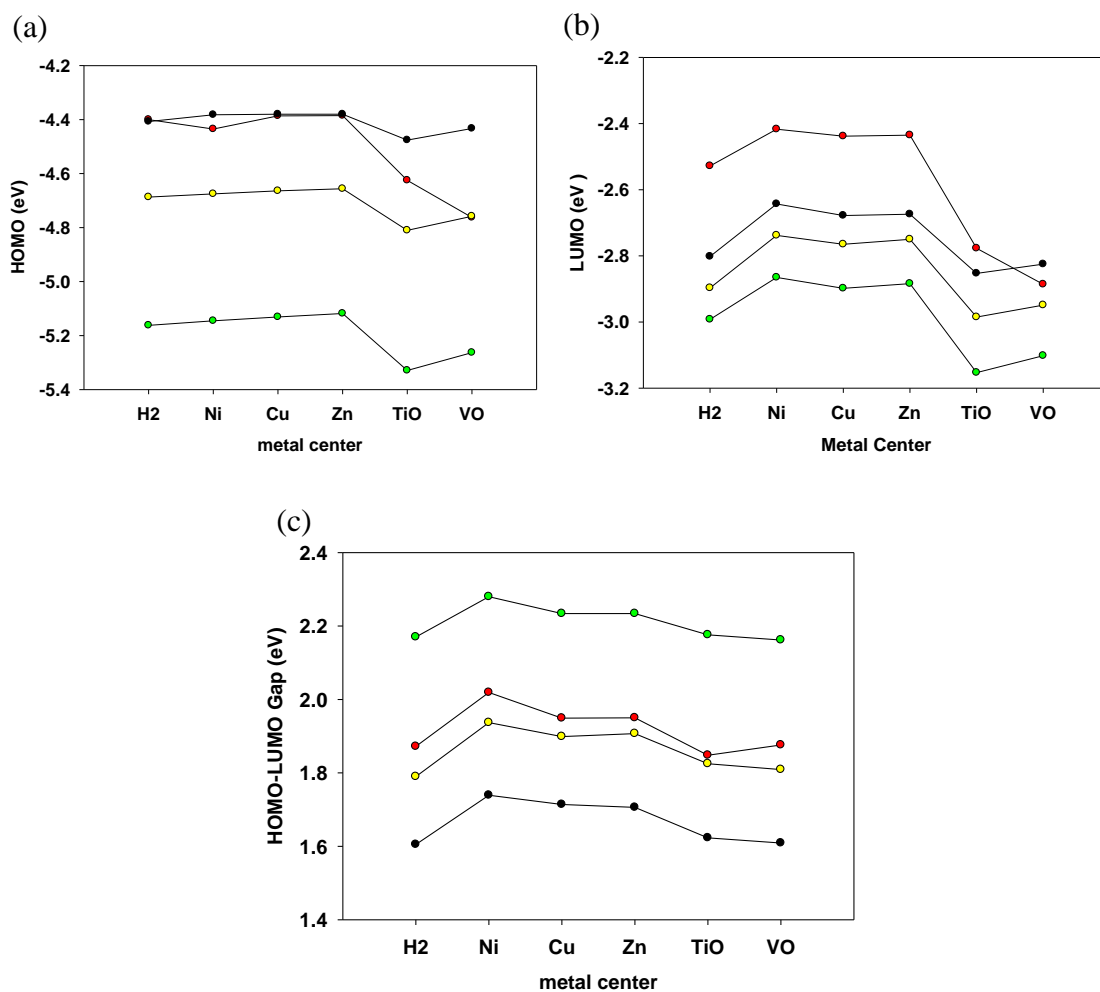
Figure 2.3. The energy level and band gap of the Pc, OBuPc, Nc and OBuNc with different metal centers. (a) HOMO energy level; (b) LUMO energy level; (c) HOMO-LUMO Gap. ──●── Pc, ──●── OBuPc, ──○── Nc and ──●── OBuNc

Table 2.1. The visualization of the HOMO and LUMO molecular orbital. (a) HOMO orbitals; (b) LUMO orbitals.

(a)
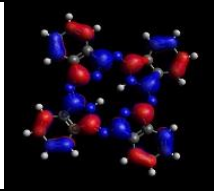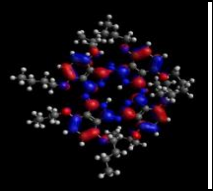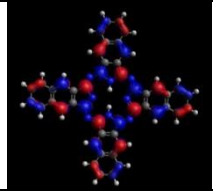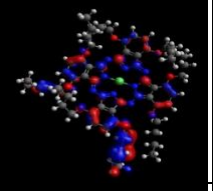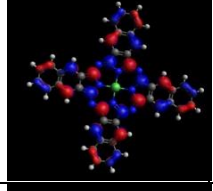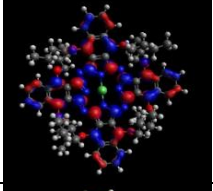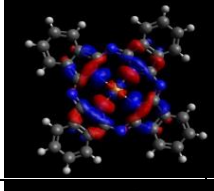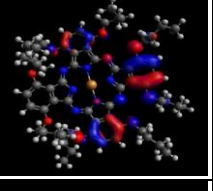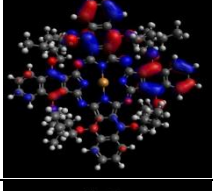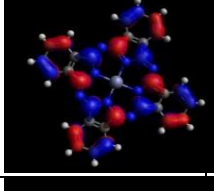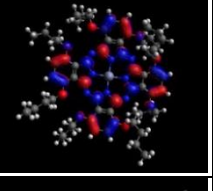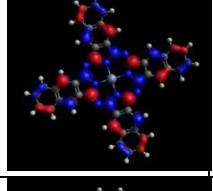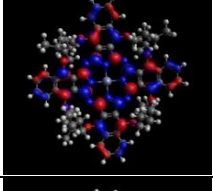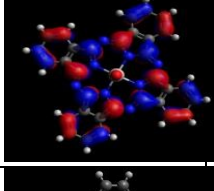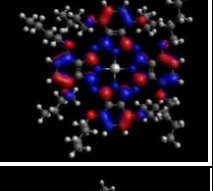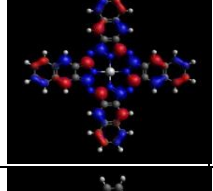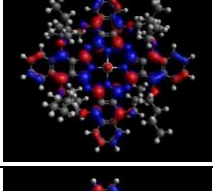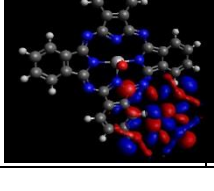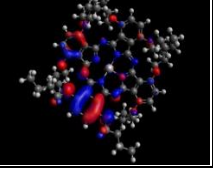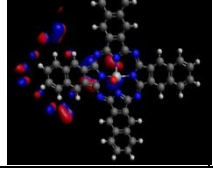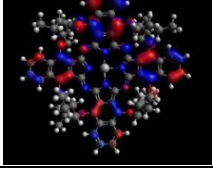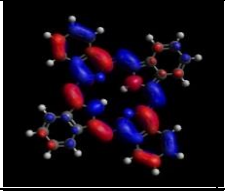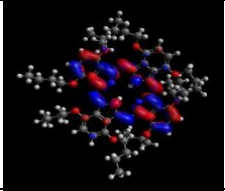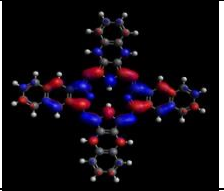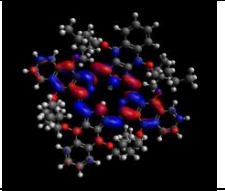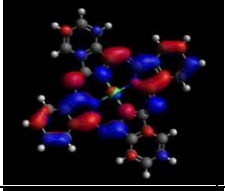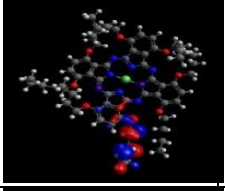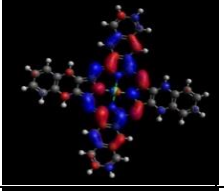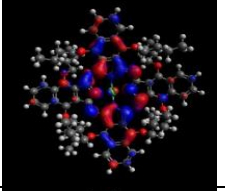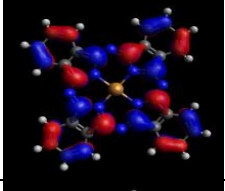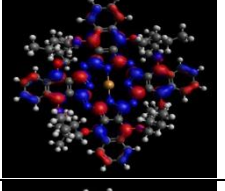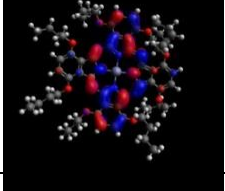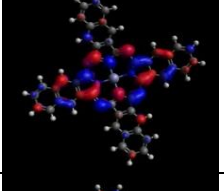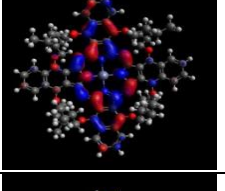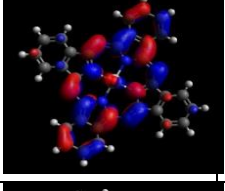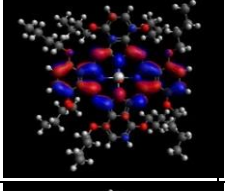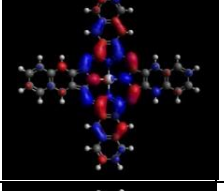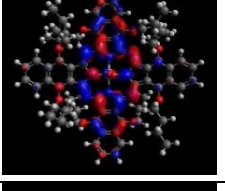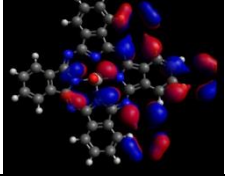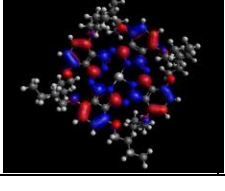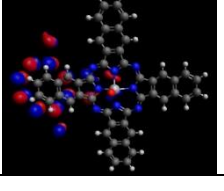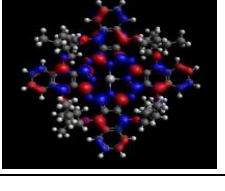
HOMO	Pc	OBuPc	Nc	OBuNc
H$_2$				
Ni				
Cu				
Zn				
TiO				
VO				

Table 2.1. Continued

(b)

LUMO	Pc	OBuPc	Nc	OBuNc
H$_2$				
Ni				
Cu				
Zn				
TiO				
VO				

(a)

(b)

Figure 2.4. The internal reorganization energy of the Pc, OBuPc, Nc and OBuNc with different metal centers. (a) electron transport; (b) hole transport. ⎯⦿⎯ Pc, ⎯⦿⎯ OBuPc, ⎯⦿⎯ Nc and ⎯⦿⎯ OBuNc

For the electron or hole charge transfer, the substitution of octabutoxy ligand significantly increases the internal reorganization energy. It can be understood by examining the molecular geometry of the octabutoxy substituted phthalocyanine and naphthalocyanine. As shown in Figure 2.5, the octabutoxy substitution makes the structure not planar and therefore it will be harder for the octabutoxy substituted molecules to distort and reorganize compared to the flat phthalocyanine molecules. There have been reported X-ray data that the octabutoxy substituted nickel phthalocyanine shows a strained saddle[38] structure instead of the planar structures in phthalocyanines, which agrees with our simulation results.
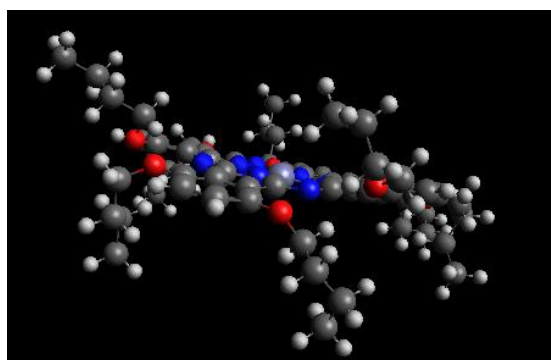
Figure 2.5. Optimized geometry of ZnOBuPc

After the DFT studies of band gap and reorganization energy, TDDFT simulations were conducted on the optimized geometries and the electronic absorption spectra were obtained.

A representative example of the UV-Vis spectrum is shown in Figure 2.6 (the others are included as the supplementary materials in Figure A.1.) and the assignment of the peaks are displayed in Table 2.3. The spectra with varying metal center or peripheral ligand are also plotted to determine how they tune the spectra.
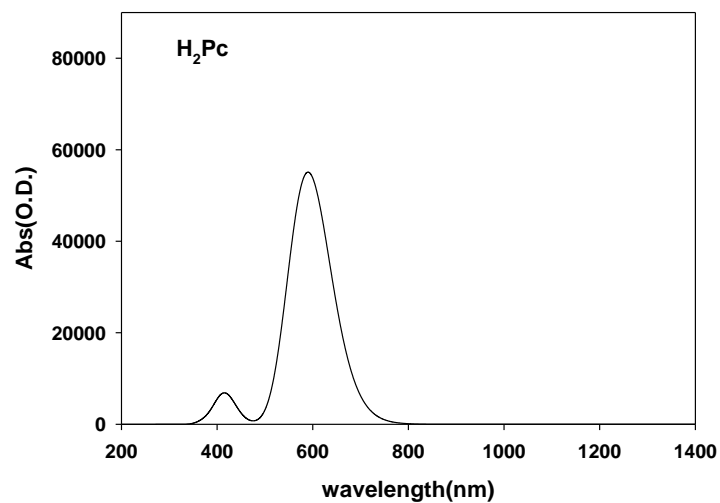
Figure 2.6. The calculated UV-VIS spectrum of the metal-free phthalocyanine molecule H_2Pc.
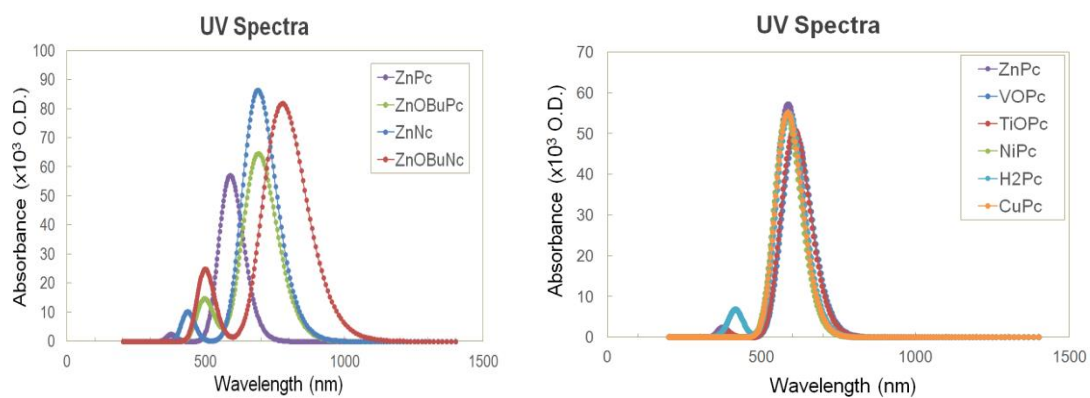
Figure 2.7. The calculated UV spectra by varying ligand or metal center

Table 2.2. The wavelengths (nm) of the absorption of the Pc, OBuPc, Nc and OBuNc with different metal centers.

Metal	Ligand	S_n	E/eV	E/nm	f	Dominant Transitions (configuration coefficient)
H$_2$	Pc	1	2.10	591.3	0.3277	HOMO$\rightarrow$ LUMO+1
		2	2.11	588.2	0.4332	HOMO$\rightarrow$ LUMO
		3	2.98	415.8	0.0923	HOMO$-1\rightarrow$ LUMO
	OBuPc	1	1.76	705.2	0.4584	HOMO$\rightarrow$ LUMO
		2	1.80	687.6	0.3950	HOMO$\rightarrow$ LUMO+1
		3	2.46	503.6	0.0962	HOMO$-1\rightarrow$ LUMO
		4	2.51	494.8	0.0400	HOMO$-2\rightarrow$ LUMO
		5	2.54	488.6	0.0378	HOMO$-1\rightarrow$ LUMO+1
	Nc	1	1.75	710.3	0.6275	HOMO$\rightarrow$ LUMO
		2	1.84	675.4	0.5399	HOMO$\rightarrow$ LUMO+1
		4	2.75	451.6	0.1449	HOMO$-2\rightarrow$ LUMO
	OBuNc	1	1.53	808.1	0.5749	HOMO$\rightarrow$ LUMO
		2	1.65	753.4	0.5319	HOMO$\rightarrow$ LUMO+1
		3	2.36	525.0	0.1467	HOMO$-1\rightarrow$ LUMO
		4	2.47	502.3	0.0211	HOMO$-3\rightarrow$ LUMO
		5	2.51	493.1	0.0337	HOMO$-2\rightarrow$ LUMO
Ni	Pc	2	2.13	580.9	0.3767	HOMO$\rightarrow$ LUMO
		3	2.13	580.9	0.3769	HOMO$\rightarrow$ LUMO+1
	OBuPc	1	1.84	672.4	0.4243	HOMO$\rightarrow$ LUMO
		2	1.87	664.4	0.4389	HOMO$\rightarrow$ LUMO+1
	Nc	1	1.81	684.9	0.5535	HOMO$\rightarrow$ LUMO
		2	1.81	684.7	0.5534	HOMO$\rightarrow$ LUMO+1
	OBuNc	1	1.60	776.4	0.4976	HOMO$\rightarrow$ LUMO
		2	1.63	762.9	0.5563	HOMO$\rightarrow$ LUMO+1
Cu	Pc	4	2.12	585.4	0.3805	HOMO$\rightarrow$ LUMO
		5	2.12	585.4	0.3804	HOMO$\rightarrow$ LUMO+1
	OBuPc	4	1.80	688.4	0.4192	HOMO$\rightarrow$ LUMO
		5	1.81	684.0	0.4434	HOMO$\rightarrow$ LUMO+1
	Nc	4	1.80	687.4	0.5697	HOMO$\rightarrow$ LUMO
		5	1.80	687.3	0.5695	HOMO$\rightarrow$ LUMO+1
	OBuNc	4	1.59	780.2	0.5165	HOMO$\rightarrow$ LUMO
		5	1.61	767.8	0.5712	HOMO$\rightarrow$ LUMO+1

Table 2.2. Continued

Zn	Pc	1	2.12	586.1	0.3950	HOMO→ LUMO
		2	2.12	586.1	0.3949	HOMO→ LUMO+1
		7	3.32	373.5	0.0168	HOMO−1→ LUMO
		8	3.31	373.5	0.0168	HOMO−1→ LUMO+1
	OBuPc	1	1.80	689.7	0.4340	HOMO→ LUMO
		2	1.81	686.1	0.4595	HOMO→ LUMO+1
		3	2.48	500.1	0.0898	HOMO−1→ LUMO
		4	2.53	490.3	0.0968	HOMO−1→ LUMO+1
		5	2.55	486.6	0.0202	HOMO−2→ LUMO+1
	Nc	1	1.81	685.9	0.5971	HOMO→ LUMO
		2	1.81	685.9	0.5971	HOMO→ LUMO+1
		5	2.87	432.7	0.1412	HOMO−1→ LUMO
	OBuNc	1	1.59	779.9	0.5447	HOMO→ LUMO
		2	1.61	769.8	0.5892	HOMO→ LUMO+1
		3	2.48	500.2	0.0502	HOMO−2→ LUMO
		4	2.50	496.3	0.1873	HOMO−1→ LUMO
TiO	Pc	1	2.04	606.5	0.3521	HOMO→ LUMO
		2	2.04	606.5	0.3522	HOMO→ LUMO+1
		6	3.26	380.1	0.0059	HOMO−3→ LUMO
	OBuPc	1	1.70	728.4	0.4094	HOMO→ LUMO
		2	1.74	711.5	0.3911	HOMO→ LUMO+1
		4	2.45	506.9	0.0489	HOMO−1→ LUMO
		5	2.48	499.3	0.0612	HOMO−2→ LUMO+1
	Nc	1	1.71	723.3	0.5194	HOMO→ LUMO
		2	1.71	723.3	0.5195	HOMO→ LUMO+1
	OBuNc	1	1.49	830.2	0.4564	HOMO→ LUMO
		2	1.52	814.5	0.5209	HOMO→ LUMO+1
		3	1.87	664.0	0.0128	HOMO→ LUMO+2
		5	2.41	513.4	0.2039	HOMO−1→ LUMO
VO	Pc	3	2.03	610.5	0.3447	HOMO→ LUMO
		4	2.03	610.5	0.3447	HOMO→ LUMO+1
	OBuPc	3	1.73	717.7	0.3887	HOMO→ LUMO
		4	1.74	711.0	0.3741	HOMO→ LUMO+1
	Nc	3	1.70	731.4	0.4984	HOMO→ LUMO
		4	1.70	731.4	0.4983	HOMO→ LUMO+1
	OBuNc	3	1.48	837.6	0.4506	HOMO→ LUMO
		4	1.49	831.6	0.4926	HOMO→ LUMO+1

For all the Pc, OBuPc, Nc and OBuNc studied, there is always an intense absorption around 580-800 nm which is mainly attributed to the transition from HOMO to LUMO and termed the Q band.[23, 39] There is an additional less stronger peak near 400 nm. It is called the Soret band[23, 39] and produced by transition from the deeper occupied molecular orbitals of HOMO-1, HOMO-2 or HOMO-3 to the LUMO or LUMO+1. By examining the difference of the spectra with various metal or ligand substitutions, we can draw a similar conclusion that the ligand substitutions tune the absorption of phthalocyanines more than the metal center. The introduction of octabutoxy and phenyl ligand makes the peaks red-shifted.

2.4   CONCLUSIONS AND DISCUSSIONS

Calculations were performed on phthalocyanines and naphthalocyanines by varying the metal and ligand substitutions. DFT was used to optimize the geometries and predict electronic properties of molecular orbital composition, energy level and internal reorganization energy. TDDFT was applied to simulate the UV-VIS absorption spectra. From both the electrical and optical calculation results, it was found that the substitution of ligand was more influential than the modification of the metal center. Consequently, one can expect a considerable difference in redox potential by ligand substitution, but subtle changes by modulating the metal site. We will use the calculations to tune the charge transport in the organic field effect transistor discussed in Chapter 4.

3.0 ELECTRONIC COUPLING BETWEEN TWO AMINE REDOX SITES

THROUGH THE 5,5'-POSITIONS OF METAL-CHELATING 2,2'-BIPYRIDINES

This work was published in Chemistry- A European Journal, 2012, 18,14497-1450 (Hai-Jing Nie, Xialing Chen, Chang-Jiang Yao, Yu-Wu Zhong, Geoffrey R. Hutchison, and Jiannian Yao) as **"Electronic Coupling between Two Amine Redox Sites through the 5,5'-Positions of Metal-Chelated 2,2'-Bipyridines". Xialing Chen conducted the simulation work under the supervision of Geoffrey R Hutchison.**

3.1 INTRODUCTION

The understanding of electron-transfer processes in conjugated donor–bridge–acceptor arrays is of fundamental importance for molecule-based electronic devices. Mixed- valence (MV) compounds provide a simple model for this purpose.[40-43] In a common MV compound with M^{n+}-L-$M^{(n+1)+}$ formulation,[44-51] and references cited there in the organometallic redox centers M^{n+} and $M^{(n+1)+}$ act as donor and acceptor, respectively, and L stands for an organic bridge. A special feature in MV systems is that the donor and acceptor component have the same composition but different oxidation state.

In addition to organometallic or inorganic redox centers, the use of organic redox components in MV systems has received considerable interest recently.[52-54] For example, hydra-

zine,[55-57] quinone,[58, 59] and nitrobenzene[60, 61] have been examined as the charge-bearing sites in a number of organic MV systems.

However, the most widely studied organic MV systems are those with triarylamines.[62-64] Triarylamines are extensively used as hole-injecting and hole-transporting materials in a wide range of optoelectronic devices,[65] such as photovoltaic cells,[66, 67] organic light-emitting diodes,[68] and electrochromic films.[69] The readily accessible N/N$^{\bullet+}$ redox process of triarylamines and good stability of the oxidized N$^{\bullet+}$ species are some advantages. Most reported triarylamine MV systems are bridged by a readily oxidizable organic bridge (Figure 3.1),[62, 63] for example, phenyl, anthracene, phenylalkynyl, phenylvinyl, platinum alkynyl, paracyclophane, oligofluor-ene, or oligothiophene. The design and study of triarylamine MV systems with new category of bridges is of interest. Information obtained in studies on charge transfer processes in these systems is useful for the design and synthesis of new optoelectronic materials.
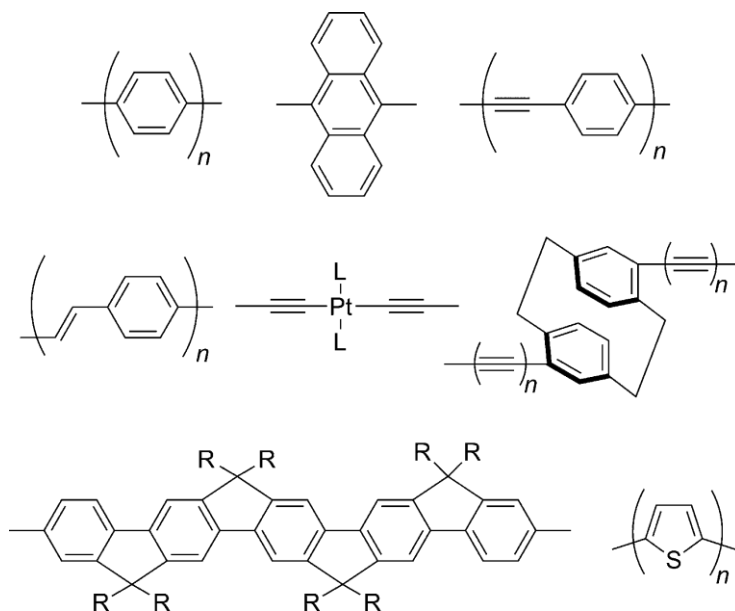
Figure 3.1. Representative organic bridges for triarylamine MV systems (n = 0–4).

According to the Robin and Day classification,[70] MV systems are characterized as Class I, II, or III depending on the strength of the electronic coupling between individual redox sites, which

22

ranges from essentially zero (class I), to moderate or strong (class II), and to very strong (class III). For a class II system, a single intervalence charge-transfer (IVCT) band in the near-infrared (NIR) region is frequently observed. This band is associated with the optically induced electron transfer between two redox sites. It is usually symmetric, broad, and of low energy and molar absorptivity. The energy of the IVCT band ($\tilde{v}_{max}$) of a class II system is equal to the total reorganization energy (λ) of the involved electron-transfer process and is solvent-dependent. In contrast, class III systems often exhibit narrow and asymmetric IVCT bands. These bands are solvent-independent and sometimes have distinct vibrational structures. Recently, a new intermediate MV system, namely, the borderline II/III class,[71, 72] has received considerable attraction, wherein the electron is localized but solvent is averaged.

On the other hand, transition metal complexes with polypyridine ligands often have rich redox and optical properties.[73-76] Incorporation of metal components into triarylamines would produce materials with appealing electronic properties. For example, some triarylamine containing ruthenium complexes have been reported to have enhanced light-harvesting strength and hole-transporting abilities and displayed promising performances in dye-sensitized solar cells.[77, 78]

However, the use of polypyridine complexes in organic MV systems has been rarely documented. In conjugation with our continued interest in the design of and studies on new MV systems with transition metal complexes,[2g–j] we recently reported the first organic MV system A bridged by a polypyridine metal component[50] (Figure 3.2; M = [Ru- (tpy)$_2$], tpy = 2,2';6', 2''-terpyridine). This complex displays an IVCT band at 1240 nm. However, it overlaps strongly with the Ru→N$^{\bullet+}$ transition at the lower-energy side. Following this report, we disclosed new organic triarylamine MV system B containing a polypyridine metal unit[79] (Figure 3.2 ; M = [Re(CO)$_3$Cl]). Systems A and B differ in that the two amine sites in A are bridged through the metal center,

while two di-p-anisylamino groups in B are connected through the 5,5'-positions of a laterally metal chelating 2,2'-bipyridine. However, the electronic properties of system B and the underlying charge transfer mechanism have not been addressed in depth. We present here a thorough study on system B by expanding the metal component to [Ru(bpy)$_2$] and [Ir(ppy)$_3$] (Scheme 3.1), where bpy is 2,2'-bi-pyridine and ppy is 2-phenylpyridine. The electronic proper- ties of diamine compounds 1–4 and newly prepared monoamine model compounds 5–8 were studied by structural, electrochemical, spectroscopic, and theoretical calculations. Corresponding one-electron-oxidized MV systems were interpreted by NIR transition analysis. In addition, frontier orbital calculations were performed on the one-electron-oxidized species in vacuum and various solvents to gain information on the spin-density population and charge-transfer mechanism.
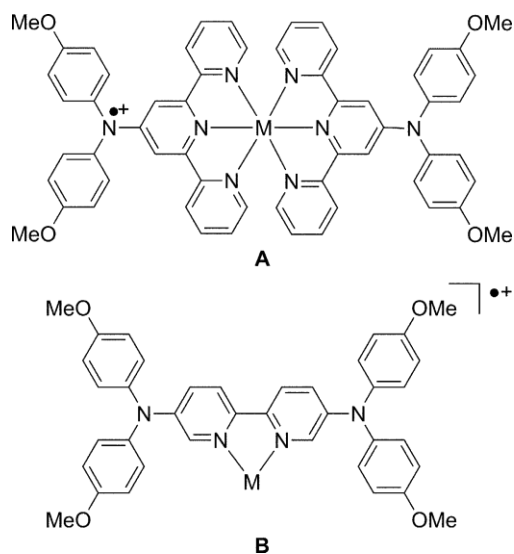
Figure 3.2. Triarylamine MV systems A and B. Counteranions are omitted.

24

3.2   EXPERIMENTAL SECTION

Spectroscopic measurements: All UV/Vis absorption spectra were obtained by using a TU-1810DSPC spectrometer from Beijing Purkinje General Instrument Co. Ltd. at room temperature in denoted solvents in a conventional 1.0 cm quartz cell. UV/Vis/NIR spectra were recorded on a PE Lambda 750 UV/Vis/NIR spectrophotometer.

Electrochemical measurement: All CV measurements were made with a CHI 620D potentiostat with one-compartment electrochemical cell under an atmosphere of nitrogen. All measurements were carried out in 0.1 M Bu_4NClO_4/acetonitrile at a scan rate of 100 mV.s^{-1}. The glassy carbon working electrode had a diameter of 0.3 mm. The electrode was polished prior to use with 0.05 mm alumina and rinsed thoroughly with water and acetone. A large-area platinum wire coil was used as counter electrode. All potentials are referenced to an Ag/AgCl electrode in saturated aqueous NaCl without regard for the liquid junction potential.

Oxidative spectroelectrochemistry: Oxidative spectroelectrochemistry was performed in a thin-layer cell (optical length=0.2 cm) in which an ITO glass electrode was set in indicated a solution of the compound under study (c≈1*10^{-4} M) and 0.1 M TBAP as supporting electrolyte. A platinum wire and Ag/AgCl in saturated aqueous solution were used as counter electrode and reference electrode, respectively. The cell was put into a PE Lambda 750 UV/Vis/NIR spectrophotometer to monitor spectral changes during electrolysis.

Computational methods: DFT calculations were carried out by using the B3LYP exchange correlation functional[80] as implemented in the Gaussian 09 program package.[81]

The electronic structures of complexes were determined by using a general basis set with the Los Alamos effective core potential LanL2DZ basis set for ruthenium and 6-31G* for other atoms.[34] Solvation effects were included by employing the conductor-like polarizable continuum

model (CPCM) with solvent=acetonitrile and united-atom Kohn–Sham (UAKS) radii.[82-84]For calculations of the localization/delocalization of the radical cations, the B3LYP functional was used with 35% HF exchange instead of the usual 20%, in accordance with previous methodology by Kaupp et al.[85]

Characterization: NMR spectra were recorded on a Bruker Avance 400 MHz spectrometer. Spectra are reported in ppm from residual protons of deuterated solvent for ^{1}H NMR (7.26 ppm for $CDCl_3$ and 1.92 ppm for CD_3CN) and ^{13}C NMR (77.00 ppm for $CDCl_3$). MS data were obtained with a Bruker Daltonics Inc. Apex II FT-ICR or Autoflex III MALDI-TOF mass spectrometer. The matrix for MALDI-TOF measurement was a-cyano-4-hydroxycinnamic acid. Microanalysis was carried out using Flash EA 1112 or Carlo Erba 1106 analyzer at the Institute of Chemistry, Chinese Academy of Sciences. Compounds 1 and 3 were prepared according to published procedures.[79]

Synthesis of ruthenium complex 2: 1 (36 mg, 0.06 mmol) and [Ru (bpy)$_2$Cl$_2$] 2H$_2$O (37 mg, 0.08 mmol, 1.2 equivalent) were added to 10 mL of ethanol and 5 mL of water. The mixture was stirred and heated to reflux for 4 h under N_2 atmosphere. After cooling to room temperature, ethanol was removed under reduced pressure, followed by the addition of an excess of KPF_6. The resulting precipitate was collected by filtering and washed with water and Et_2O. The obtained solid was subjected to flash column chromatography on silica gel (eluent: saturated aq. KNO_3/water/acetonitrile 1/20/500) followed by anion exchange with KPF_6 to give 35 mg of complex 2 in a yield of 45%. 1H NMR (400 MHz, CD3CN): d=3.81 (s, 12 H), 6.56 (d, J=2.3 Hz, 2H), 6.85 (d, J=8.8 Hz, 8H), 6.96 (d, J=8.8 Hz, 8H), 7.06 (t, J=6.7 Hz, 2 H), 7.18 (d, J=11.6 Hz, 2H), 7.47 (d, J=5.6 Hz, 2H), 7.52 (t, J=6.7 Hz, 2 H), 7.74 (t, J=7.8 Hz, 2H), 7.82 (d, J=9.1 Hz, 2H), 7.92 (d, J=5.4 Hz, 2 H), 8.10 (t, J=7.9 Hz, 2H), 8.22 (d, J=8.1 Hz, 2 H), 8.45 (d, J=8.1 Hz, 2H);

MALDI-MS: m/z 1169.3 [M-PF6]+, 1024.3 [M-2PF6]+, 868.3 [M-2PF6-bpy]+; elemental analysis (%) calculated for $C_{58}H_{50}F_{12}N_8O_4P_2Ru \cdot H_2O$: C 52.30, H 3.93, N 8.41; found: C 52.57, H 3.90, N 8.54.

Synthesis of iridium complex 4: Compound 1 (50 mg, 0.08 mmol) and 2 (44 mg, 0.04 mmol, 0.5 equivalent) were added to 10 mL of CH_2Cl_2 and 5 mL of MeOH. The mixture was stirred and heated to reflux for 6 h under an N_2 atmosphere. After cooling to room temperature, an excess of KPF_6 was added. The suspension was stirred for 30 min and then filtered to remove insoluble inorganic salts. The filtrate was concentrated under reduced pressure to afford a crude yellow solid. The obtained solid was dissolved in 20 mL CH_2Cl_2 and the solution washed with H_2O (20 mL*3). The organic phase was dried over anhydrous $MgSO_4$. The solvent was removed under reduced pressure, and the crude product was purified by silica gel chromatography (eluent: 100/1 CH_2Cl_2/ MeOH) to give 65 mg of complex 4 (62%). ^{1}H NMR (400 MHz, CDCl3): d=3.82 (s, 12H), 6.06 (d, J=7.5 Hz, 2H), 6.59 (t, J=7.2 Hz, 2H), 6.72 (t, J=7.4 Hz, 2H), 6.76 (d, J=8.7 Hz, 8 H), 6.89 (d, J=8.7 Hz, 8H), 7.12 (s, 2H), 7.15 (t, J=6.4 Hz, 2H), 7.31 (d, J=9.2 Hz, 2 H), 7.38 (d, J=7.7 Hz, 2H), 7.68 (d, J=5.7 Hz, 2H), 7.82 (m, 4H), 7.89 (d, J=9.2 Hz, 2H); MALDI-MS: m/z 1111.5 [M-PF6]$^+$; elemental analysis (%) calculated for $C_{60}H_{50}F_6N_6O_4PIr$: C 57.36, H 4.01, N 6.69; found: C 57.50, H 4.24, N 6.52.

Synthesis of 5-(di-p-anisylamino)-2,2'-bipyridine (5): A suspension of 5- bromo-2,2'-bipyridine (200 mg, 0.85 mmol), 4,4'-dimethoxydiphenylamine (293 mg, 1.28 mmol, 1.5 equivalent), [Pd2(dba)3] (39 mg, 0.04 mmol, 5 mol%), dppf (24 mg, 0.04 mmol, 5 mol%), and NaOtBu (98 mg, 1.02 mmol, 1.2 equivalent) in 15 mL of toluene was heated at 140 ℃ for 48 h under N_2 atmosphere in a sealed pressure tube. The system was then cooled to room temperature. The solvent was removed under vacuum and the crude product was purified by silica gel

chromatography (eluent: 5/1 petroleum ether/ethyl acetate) to yield 207 mg of 5 as a yellow solid (64%).^{1}H NMR (400 MHz, CDCl3): d 3.79 (s, 6H), 6.85 (d, J=8.7 Hz, 4 H), 7.09 (d, J=8.7 Hz, 4 H), 7.19 (t, J=6.1 Hz, 1H), 7.30 (d, J=8.7 Hz, 1H), 7.73 (t, J=7.6 Hz, 1 H), 8.17 (d, J=8.7 Hz, 1H), 8.25 (d, J=8.0 Hz, 1H), 8.28 (d, J=2.1 Hz, 1H), 8.60 (d, J=4.6 Hz, 1H); 13C NMR (100 MHz, CDCl3): d=55.5, 115.0, 120.1, 121.0, 122.5, 126.2, 126.8, 136.7, 139.5, 140.8, 145.2, 147.3, 149.0, 156.2, 156.5; EI-HRMS: m/z calculated for $C_{24}H_{21}N_3O_2$: 383.1634; found: 383.1638. Synthesis of ruthenium complex 6: 5 (50 mg, 0.13 mmol) and [Ru(bpy)$_2$Cl$_2$] 2H$_2$O (82 mg, 0.16 mmol, 1.2 equivalent) were added to 10 mL of ethanol and 5 mL of water. The mixture was stirred and heated to reflux for 4 h under N$_2$ atmosphere. After cooling to room temperature, ethanol was removed under reduced pressure, followed by the addition of an excess of KPF$_6$. The resulting precipitate was collected by filtering and washed with water and Et$_2$O. The obtained solid was subjected to flash column chromatography on silica gel (eluent: saturated aq. KNO$_3$/water/acetonitrile 1/20/400) to give 105 mg of complex 6 (74%). ^{1}H NMR (400 MHz, CD$_3$CN): d=3.82 (s, 6H), 6.66 (d, J=2.3 Hz, 1 H), 6.87 (d, J=8.8 Hz, 4 H), 7.00 (d, J=8.8 Hz, 4H), 7.09 (t, J=6.5 Hz, 1 H), 7.21 (m, 2H), 7.36 (t, J=6.4 Hz, 1H), 7.46 (m, 3H), 7.56 (d, J=5.6 Hz, 1 H), 7.74 (m, 1H), 7.78 (d, J=6.7 Hz, 2H), 7.87 (d, J=5.5 Hz, 1 H), 7.91 (t, J=7.8 Hz, 1H), 8.06 (m, 4 H), 8.17 (d, J=8.3 Hz, 1H), 8.25 (d, J=8.0 Hz, 1H), 8.47 (d, J=8.2 Hz, 3H); MALDI-MS: m/z 942.3 [M-PF$_6$]$^+$, 797.3 [M-2PF$_6$]$^+$, 641.2 [M-2PF$_6$bpy]$^+$; elemental analysis (%) calculated for $C_{44}H_{37}F_{12}N_7O_2P_2Ru$ 4H$_2$O: C 45.60, H 3.91, N 8.46; found: C 45.44, H3.42, N 8.83.

Synthesis of rhenium complex 7: 5 (50 mg, 0.13 mmol) and [Re(CO)$_5$Cl](57 mg, 0.16 mmol, 1.2 equivalent) were added to 10 mL of toluene. The mixture was stirred and heated to reflux for 8 h under N$_2$ atmosphere. After cooling to room temperature, toluene was removed under reduced pressure. The obtained solid was subjected to flash column chromatography on silica gel

(eluent: 40/1 CH_2Cl_2/ethyl acetate) to give 85 mg of complex 7 (94%). ^{1}H NMR (400 MHz, $CDCl_3$): d=3.83 (s, 6H), 6.96 (d, J=8.6 Hz, 4H), 7.19 (d, J=8.6 Hz, 4H), 7.26 (overlapping with solvent residue,1 H), 7.33 (m, 1H), 7.79 (d, J=8.7 Hz, 1H), 7.90 (overlapping, 2 H), 8.52 (s, 1H), 8.91 (d, J=5.1 Hz, 1H); MALDI-MS: m/z 1341.2 [2M-Cl]$^+$, 1287.3 [2M-Cl-2CO]$^+$, 654.3 [M-Cl]$^+$; elemental analysis (%) calculated for $C_{27}H_{24}ClN_3O_5Re$: C 46.85, H 3.49, N 6.07; found: C 46.88, H 3.30, N 6.01.

Synthesis of iridium complex 8: 5 (50 mg, 0.13 mmol) and [{Ir (ppy)$_2$Cl}$_2$] (70 mg, 0.065 mmol, 0.5 equivalent) were added to 10 mL of CH_2Cl_2 and 5 mL of MeOH. The mixture was stirred and heated to reflux for 6 h under an N_2 atmosphere. After cooling to room temperature, an excess of KPF$_6$ was added. The suspension was stirred for 30 min and then filtered to remove insoluble inorganic salts. The filtrate was evaporated to dryness under reduced pressure to give a crude yellow solid. The obtained solid was dissolved in 20 mL of CH_2Cl_2, followed by washing with H_2O (20 mL*3). The organic phase was dried over anhydrous MgSO$_4$. The solvent was removed under reduced pressure, and the crude product was purified by silica gel chromatography (eluent: 100/1 CH_2Cl_2/MeOH) to give 115 mg of complex 8 (88%). ^{1}H NMR (400 MHz, $CDCl_3$): d=3.83 (s, 6 H), 6.06 (d, J=7.5 Hz, 1 H), 6.28 (d, J=7.5 Hz, 1H), 6.62 (t, J=7.3 Hz, 1H), 6.75 (t, J=7.5 Hz, 1 H), 6.79 (d, J=8.8 Hz, 4H), 6.89 (t, J=7.4 Hz, 1H), 6.93 (d, J=8.8 Hz, 4 H), 6.99 (t, J=7.5 Hz, 1H), 7.04 (t, J=6.3 Hz, 1 H), 7.13–7.20 (m, 3H), 7.35 (dd, J=9.1, 2.6 Hz, 1H), 7.42 (d, J=7.7 Hz, 1H), 7.56 (d, J=5.7 Hz, 1 H), 7.64 (m, 2H), 7.78 (m, 3H), 7.86 (m, 2H), 7.96 (t, J=7.7 Hz, 1 H), 8.16 (d, J=9.2 Hz, 1 H), 8.29 (d, J=8.2 Hz, 1H); MALDI-MS: m/z 884.5 [M-PF6]$^+$; elemental analysis (%) calculated for $C_{46}H_{37}F_6N_5O_2PIr$: C 53.69, H 3.62, N 6.81; found: C 53.79, H 3.97, N 6.56.

3.3   RESULTS AND DISCUSSION

Design and synthesis and single crystal structure: Compounds studied in this paper (1–8) are shown in Scheme 3.1. Electron-donating methoxy substituents were used to ensure chemical reversibility of the $N/N^{\bullet+}$ process at an easily accessible potential. Amine atoms are directly connected to the bridging ligand to induce strong coupling between them. Ru, Re, and Ir metal components were chosen because of the stability of these complexes and their relatively high metal-associated oxidation potentials, which are well separated from those of triarylamines. These complexes could also offer an opportunity to study the effect of different oxidation states of the metal center (Ru^{II}, Re^{I}, Ir^{III}) on the electronic delocalization across the bridge. We note that a bis-triarylboron system bridged through the 5,5'-positions of a metal-chelating 2,2'-bipyridine was reported by Wang and co-workers.[86] However, that paper is devoted to the studies of the electron-accepting ability of triarylborons and spectroscopic response to fluoride anions, instead of MV interpretation.
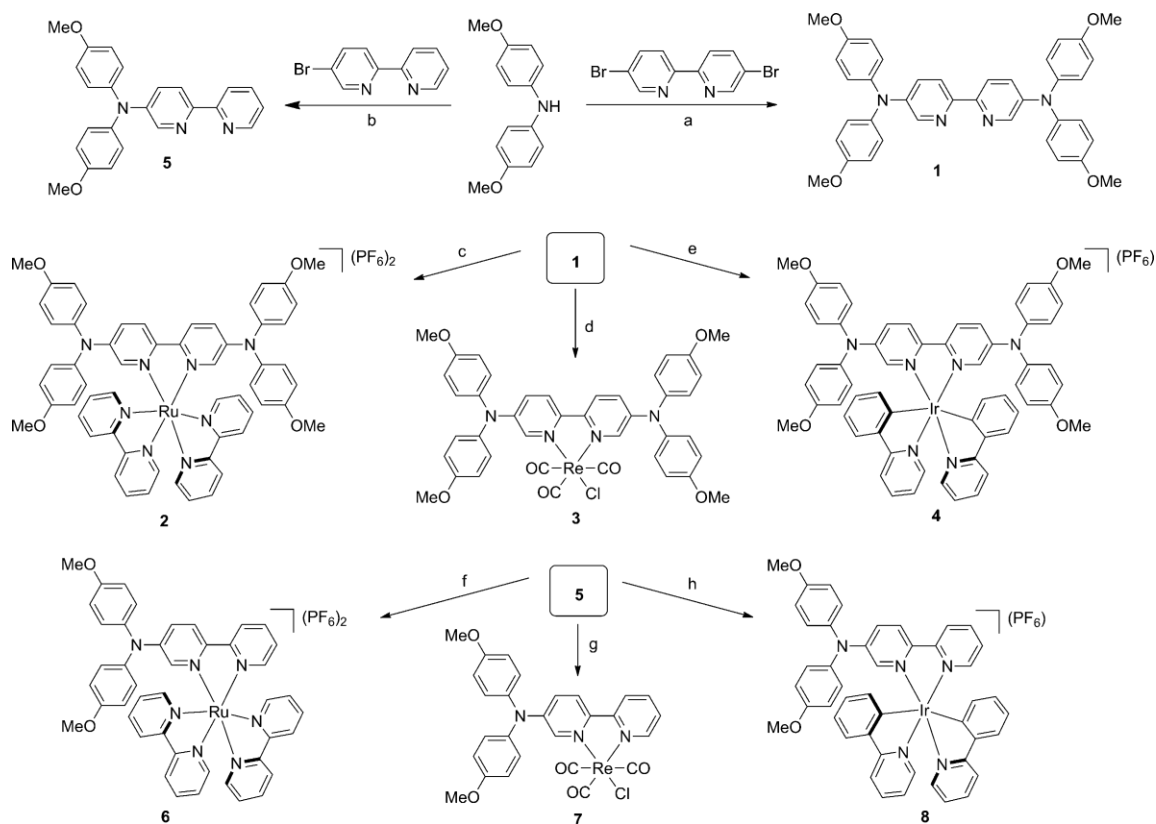
Scheme 3.1. Synthesis of studied compounds. a) [Pd$_2$(dba)$_3$] (dba = trans,trans-dibenzylideneacetone), 1,1'-bis(diphenylphosphino)ferrocene (dppf), NaOtBu, 70 %. b) [Pd$_2$(dba)$_3$], dppf, NaOtBu, 64 %. c) 1.cis-[Ru(bpy)$_2$Cl$_2$]; 2. KPF$_6$, 45 %. d) [Re(CO)$_3$Cl] , 74 %. e) 1. [{Ir(ppy)$_2$Cl}$_2$]; 2. KPF$_6$, 62 %. f) 1. cis-[Ru(bpy)$_2$Cl$_2$]; 2. KPF$_6$, 74 %. g) [Re(CO)$_3$Cl] , 94 %. h) 1. [{Ir(ppy)$_2$Cl}$_2$]; 2. KPF$_6$, 88 %.

Compounds 1–8 were synthesized as outlined in Scheme 3.1. The synthesis of 5,5'-bis(di-p-anisylamino)-2,2'-bi- pyridine (1) has been reported[79] previously by palladium-catalyzed C-N coupling between 5,5'-dibromo-2,2'-bipyridine[87] and 4,4'-dimethoxydiphenylamine.[88] A single crystal was obtained by slow evaporation of the solvent of a solution of 1 in CHCl$_3$, and its X-ray crystallographic structure is shown in Figure 3.3.[89] The N-N distance between the two amino nitrogen atoms is 9.80 Å. The two pyridine rings are essentially coplanar with a dihedral angle of 177.5°. Complexes 2–4 were obtained in moderate yields through complexion of 1 with cis-[Ru(bpy)$_2$Cl$_2$], [Re(CO)$_5$Cl] , and [Ir(ppy)$_2$Cl]$_2$, respectively. 5-(Di-p-

anisylamino)-2,2'-bipyridine 5 was prepared through a similar C-N coupling between 5-bromo-2,2'-bipyridine and 4,4'-dimethoxydiphenylamine in 64 % yield. Model complexes 6–8, with one amine redox site, were prepared as well for a comparison study. Some related triarylamine-containing polypyridine ligands or complexes such as 5,5'-bis(diphenylamino)-2,2'-bipyridine,[90] 5-(di-p-anisylamino)-2,2'-bipyridine,[91] an Ru^{II} complex with a 1,10-bis(diphenylamino)phenanthroline ligand,[92] and a Ru^{II} or Re^{I} complex with 5,5'-bis(carbazolyl)-2,2'-bipyridine[93] have previously been reported. However, none of these was intended to study the N-N electronic coupling.
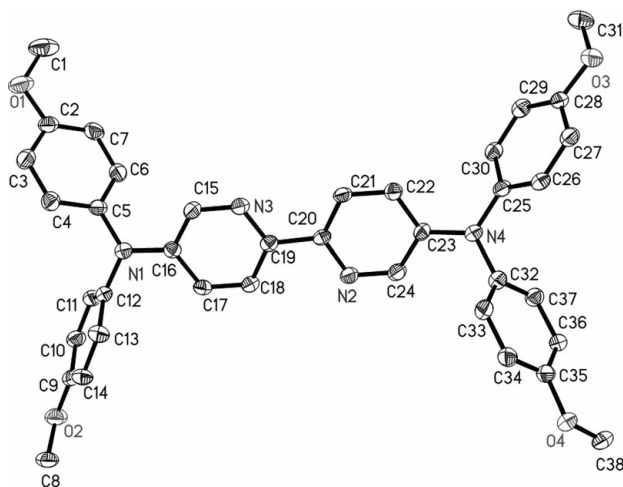
Figure 3.3. Thermal ellipsoid plot with 50 % probability of the X-ray crystal structure of 1. Hydrogen atoms and solvents are omitted for clarity.

Electrochemical studies: The electronic properties of these compounds were first studied by cyclic voltammetric (CV) analysis (Figure 3.4, Figures B.1 and B.2 in the Supporting Information, and Table 3.1). When the scan was reversed at +1.2 V, monoamine ligand 5 displayed a chemically reversible $N/N^{\bullet+}$ redox process at +0.86 V versus Ag/AgCl (see Figure B.1a in the Supporting Information, red line). However, a typical electrochemical–chemical–electrochemical (ECE) process was observed when the potential was scanned beyond +1.4 V. The irreversible

wave at +1.41 V is assigned to further oxidation of the in situ generated $N^{\bullet+}$ species ($N^{\bullet+} \rightarrow N^{2+}$), and a new product was formed during this process which gave rise to two new redox couples at +0.63 and +1.03 V. The identity of this new product has not been determined at this stage. However, similar ECE processes have been previously reported for some triarylamines, and formation of carbazole derivatives has been suggested and proved.[94, 95] This electrochemical characteristic was more or less evident in the CV profiles of all compounds studied when the potential was swept beyond +1.4 V.
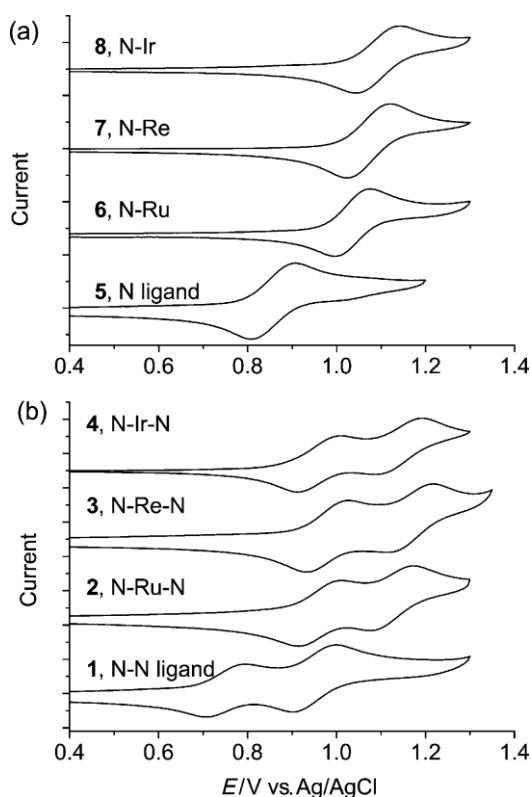
Figure 3.4. Comparison of the cyclic voltammograms of the $N/N^{\bullet+}$ processes of 1–8 in CH_2Cl_2.

Bisamine ligand 1 exhibited two well-separated redox couples at +0.75 and +0.95 V versus Ag/AgCl (See Figure B.1e in the Supporting Information). They are associated with the stepwise oxidation of two amine sites to the corresponding nitrogen radical cation species ($N^{\bullet+}$). The comproportionation constant Kc[96] is 2450, which indicates moderate thermodynamic stability of

the electrochemically generated organic MV species. When ligands 1 and 5 are coordinated with Ru^{II}, Re^{I}, or Ir^{III}, the $N/N^{\bullet+}$ processes take place at higher potential (around 200 mV more positive, Figure 3.4), reflecting the electron-withdrawing nature of the metal components. Similarly, two well-separated $N/N^{\bullet+}$ processes are observed in the CV profiles of complexes 2–4, and the potential separation ΔE is 160, 200, and 180 mV, respectively. We stress that the ΔE value should not be taken as a parameter for quantitative measurement of the electronic coupling between two amine sites. Compounds 1–4 are not a family with analogous, closely related structures and electronic properties. Moreover, electrochemical data are largely dependent on the measurement conditions, such as the solvent and supporting electrolyte.[97, 98] In addition to the $N/N^{\bullet+}$ and $N^{\bullet+}/N^{2+}$ processes, complexes 2 and 6 exhibit a $Ru^{II/III}$ process overlapping with the $N^{\bullet+}/N^{2+}$ wave, and complexes 3 and 7 display a Re-associated wave at higher potentials. In the case of complex 6, the anodic process is complicated by a desorption peak (Supporting Information Figure B.1b). Oxidation of iridium in complexes 4 and 8 is not evident in their CV profiles. For complexes 2–4 and 6–8, the higher cathodic current compared to the anodic current of the peaks around +1.0 V is a result of the contamination caused by the irreversible $N^{\bullet+}/N^{2+}$ processes. However, this was not an issue when the potential was scanned back before the $N^{\bullet+}/N^{2+}$ process, as shown in red lines in Figure B.1 in the Supporting Information.

Table 3.1. Electrochemical Data of Compounds Studied[a]

Compound	$E_{1/2}$ (anodic) amine-based	$E_{1/2}$ (anodic) metal-based	$E_{1/2}$ (cathodic)	ΔE^b(mV)	K_c
1, N-N ligand	+0.75, +0.95, +1.45[c]	--	--	200	2450
2, N-Ru-N	+0.96, +1.12, +1.50[c]	+1.46	-1.34, -1.55, -1.86	160	510
3, N-Re-N	+0.97, +1.17, +1.52[c]	+1.85	-1.53[d]	200	2450
4, N-Ir-N	+0.96, +1.14, +1.52[c]	[e]	-1.59, -1.98	180	1120
5, N ligand	+0.86, +1.41[c]	--	--	--	--
6, N-Ru	+1.04, +1.43[c]	+1.50[f]	-1.31, -1.53, -1.79	--	--
7, N-Re	+1.07, +1.50[c]	+1.82	-1.45,[d] -1.63[d]	--	--
8, N-Ir	+1.09, +1.49[c]	[e]	-1.48	--	--

[a]The potential is reported as the $E_{1/2}$ value vs Ag/AgCl unless otherwise noted. The anodic scan was run in dichloromethane. The cathodic scan was run in acetonitrile. [b]Potential difference of two consecutive $N/N^{\bullet+}$ processes. [c]Irreversible oxidation of $N^{\bullet+}$ species, E_{anodic}. [d]Irreversible reduction, $E_{cathodic}$. [e]Not observed. [f]Overlapping with adsorption/desorption peak.

The cathodic CV profiles of these compounds are shown in Figure B.6 in the Supporting Information and the reduction potentials are summarized in Table 3.1. No reduction event was evident for ligands 1 and 5 within the potential window of the solvent used (CH_3CN). However, Ru complexes 2 and 6 display three redox couples at -1.34, -1.55, -1.86 and -1.31, -1.53, -1.79 V versus Ag/AgCl, respectively. The first two waves are ascribed to reduction of the auxiliary bpy ligands, and the third couple is associated with reduction of the bridging bpy unit, which is connected to two electron-donating anisylamino groups and thought to be more sluggishly reduced. The cathodic waves of Re complexes 3 and 7 are chemically irreversible. In addition to the bpy-associated reduction, an irreversible Re process is believed to happen in these complexes,[99] which complicated the electrochemical behavior. The bpy-associated reduction events of Ir complexes 4 and 8 occurred at -1.59 and -1.48 V, respectively. At more cathodic potential, a ppy associated reduction wave could be observed.

Density functional calculations of the neutral states of 1–8: To aid in understanding their electronic structures, DFT calculations were first performed on the above compounds in their neutral states at the B3LYP/LanL2DZ/6-31G*/vacuum level (see details in the Experimental Section). The ruthenium and iridium complexes are cationic. However, the term "neutral state" will be used to refer to their as-prepared states for consistency. The two pyridine rings of the DFT-optimized structure of 1 are basically coplanar, consistent with its crystal structure. The LUMOs of 1, 3–5, 7, and 8 have major contributions from the bpy units connected to the anisylamino groups (Figures B.3–B.10 in the Supporting Information). However, the LUMOs of Ru complexes 2 and 6 are mainly associated with the auxiliary bpy ligands.The bpy units connected to the anisylamino groups of these two complexes begin to make major contributions at higher unoccupied orbitals such as LUMO+2 and LUMO+3. These DFT results are in agreement with the above electrochemical findings.

The upper occupied molecular orbitals of 1–4 are shown in Figure 3.5. According to the electron localization, these orbitals can be classified into four categories: those associated with both the amine and bridge components, and those lying mainly on the amine units, the metal components, or the bridge. Interestingly, the orderings of these orbitals are different for all four compounds, albeit with some similarities. The HOMOs of 1–4 are all associated with both the amine and bridge components. For 1, 2, and 4, the HOMO-1 levels have major density on the amine segments. However, HOMO-1 and HOMO-2 of 3 are dominated by Re(CO)$_3$Cl character, and its HOMO-3 has a similar composition to HOMO-1 of 1, 2, or 4. The HOMO-2 and HOMO-3 of 1 and 2 are predominantly associated with the amine components, and they are quasidegenerate. However, HOMO-2 and HOMO-3 of 4 have dominant contributions from the Ir(ppy)$_2$ segments, and their HOMO-4 and HOMO-5 have similar compositions to HOMO-2 and

HOMO-3 of 1 and 2. The metal component (Ru) of 2 predominantly contributes to its HOMO-5. The HOMO-4 levels of 1 and 2 have major characters of the bridge units. Orbitals with similar bridge-associated compositions of 3 and 4 lie in lower occupied levels (Figure B.9 and Figure B.10 in the Supporting Information).
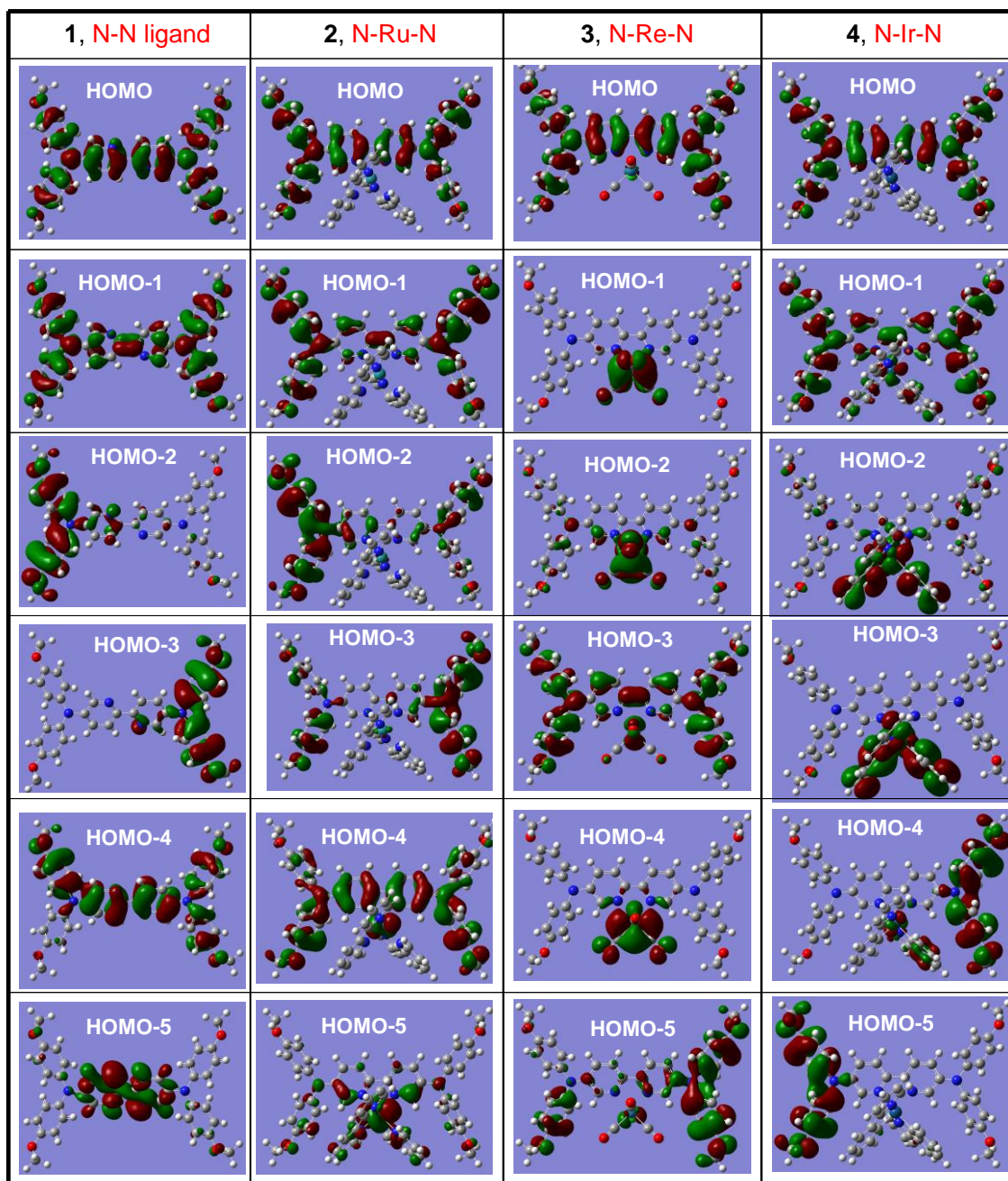
Figure 3.5. Selected frontier orbital diagrams for compounds 1-4.

The use of Koopman's theorem[100] to estimate the electronic coupling parameter H_{ab} of MV compounds has been demonstrated for many systems since 1990.[101, 102] In the case of triarylamine organic MV systems, Lambert, Coropceanu, Brdas, and co-workers[102, 103] used the energy separations ΔE between HOMO and HOMO1 to roughly estimate the amine–amine electronic coupling ($\Delta E = 2H_{ab}$). We note that HOMO and HOMO-1 of compounds in their studies have very similar orbital compositions to those of 1, 2, and 4, which have ΔE values of 0.43, 0.32, and 0.71 eV, respectively (Figure 3.6). This suggests that iridium complex 4 may have the strongest electronic coupling. For rhenium complex 3, the HOMO1 composition is totally different from those of 1, 2, and 4. Consequently, using the HOMO and HOMO-1 separation to estimate H_{ab} is meaningless for this compound. In a study of MV systems with cyclometalated ruthenium atoms as redox sites, Launay, Collin, and co-workers used a similar orbital splitting method to estimate the electronic coupling between termini.[104] However, they stressed that the orbitals involved should have high weights on the redox sites but different symmetries. In this regard, the energy separation between HOMO and HOMO-3 of 3 (0.44 eV) could be taken as an estimate for the N-N coupling, similar in magnitude to those of compounds 1 and 2.
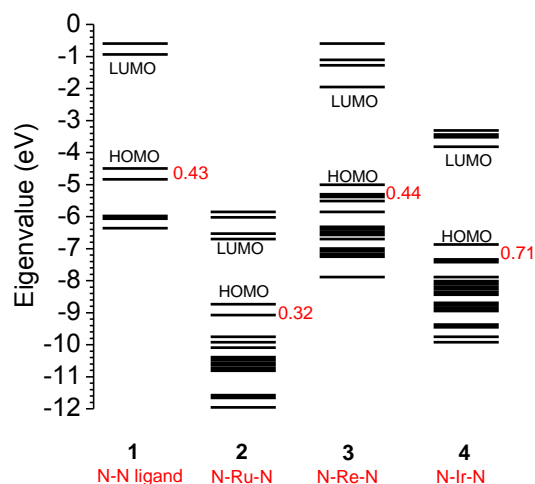
Figure 3.6. DFT-calculated frontier orbital alignment for complexes 1-4. The values shown in red color represent the energy separations (in eV) between the HOMO and HOMO-1 for 1, 2, and 4, and between the HOMO and HOMO-3 for compound 3.

Electronic spectra and TDDFT calculations of 1–8: The electronic absorption spectra of 1–8 were recorded to further study their electronic properties (Figure 3.7 and Table 3.2). To aid in the assignments of these spectra, time-dependent DFT (TDDFT) calculations of these compounds were performed at the B3LYP/LanL2DZ/6-31G*/vacuum level from the above DFT-optimized structures. Frontier orbitals that are involved in the calculated electronic transitions are provided in Figure B.3-B.10 (Supporting Information). The excitation energies E, oscillator strengths f, dominant contributing transitions, and associated percentage contributions and assignments of low-energy excitations are collected in Table B.1 in the Supporting Information. Monoamine ligand 5 displays a moderate transition in the deep-blue region (355 nm). This band is associated with the HOMO→LUMO transition and attributed to the intra-ligand charge transition (ILCT) from the triarylamine component to the electron-accepting bpy unit. Ruthenium complex 6 shows rather complex excitations in the region between 300 and 500 nm, in addition to the intense bpy-based intragand (IL) transitions at 288 nm. According to the TDDFT predications, we assign the

39

lowest-energy band of 6 at 460 nm to a similar ILCT transition, and the bands at 420 and 385 nm to the metal to ligand charge-transfer (MLCT) transitions. However, some ligand-to-ligand charge-transfer (LLCT) character could also be involved. Complexes 7 and 8 both show a broad and inseparable transition in the region between 300 and 500 nm, which are attributable to an mixture of MLCT and ILCT transitions. This assignment is supported by TDDFT calculations as well.
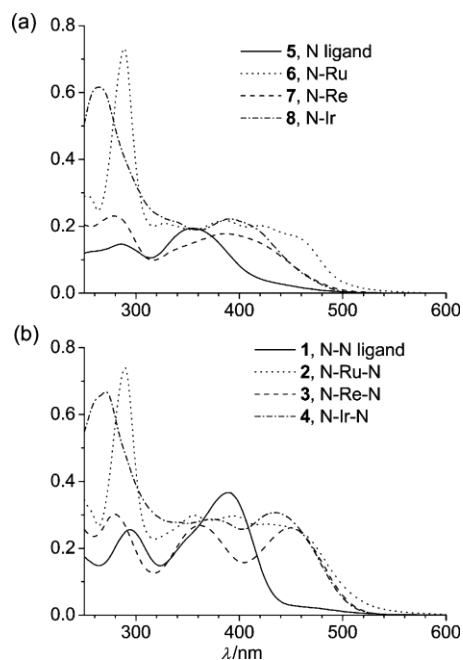
Figure 3.7. Electronic absorption spectra of 5–8 (a) and 1–4 (b) in dichloro- methane.

Table 3.2. Absorption Data of Compounds 1-8.[a]

Compound	λ_{max}/nm ($\varepsilon/10^5$ M^{-1}cm^{-1})
1, N-N ligand	294 (0.25), 388 (0.37)
2, N-Ru-N	290 (0.74), 356 (0.30), 396 (0.30), 458 (0.25)
3, N-Re-N	280 (0.30), 362 (0.27), 450 (0.26)
4, N-Ir-N	270 (0.67), 374 (0.29), 432 (0.31)
5, N ligand	285 (0.15), 355 (0.19)
6, N-Ru	288 (0.73), 328 (0.21), 385 (0.22) 420 (0.20), 460 (0.16)
7, N-Re	280 (0.23), 388 (0.18)
8, N-Ir	264 (0.62), 338 (0.21), 390 (0.22)

[a]All spectra were recorded in a conventional 1.0 cm quartz cell.

Compared to 5, the diamine ligand 1 displays redshifted and more intense ILCT transitions centered at 388 nm. The lowest energy band of ruthenium complex 2 at 450 nm is also assigned to the ILCT transitions (HOMO→LUMO+3 excitation), and its MLCT transitions are in a somewhat higher energy region. The absorption spectra of 3 and 4 are much different from those of 7 and 8 with the same metal component. The most important changes are the appearance of two isolated bands at 362 and 450 nm for 3 and 374 and 432 nm for 4. For rhenium complex 3, TDDFT calculations suggest that the band at 450 nm is involved in both ILCT and MLCT transitions (S2+S3 excitations), and the band at 362 is dominated by ILCT transitions (S6 excitation). Note that the target orbitals for these two ILCT transitions are different: LUMO for the former and LUMO+1 for the latter transition. The band at 432 nm of iridium complex 4 is predominantly associated with ILCT transitions having HOMO→LUMO character (S1 excitation), while the band at 374 nm is assigned to a mixture of ILCT and MLCT transitions (S7+S8 excitations). Again, the two ILCT transitions have different electron acceptor orbitals (LUMO and LUMO+3, respectively).

NIR transition analysis of MV species: To study the electronic couplings between two amine sites of 1–4, these compounds were gradually converted to the corresponding one or two-electron-oxidized species by electrochemical or chemical oxidation. When a potential from +0.6 to +0.9 V versus Ag/AgCl at an indium tin oxide (ITO) glass electrode was applied to a solution of 1 in dichloromethane to induce the first-electron oxidation, the ILCT transition at 388 nm decreased with concomitant emergence of three new peaks at 494, 734, 1570 nm (Figure 3.8).
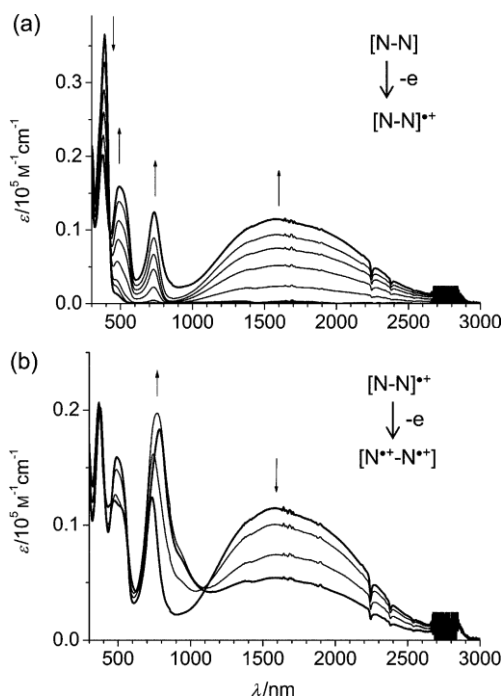
Figure 3.8. Absorption spectral changes of diamine ligand 1 in dichlorome- thane on one-electron (a) and two-electron oxidation (b) by oxidative electrolysis.

On further increasing the potential to +1.4 V to induce the second-electron oxidation, the peak at 494 nm decreased a little, the peak at 734 nm continued to increase, but the NIR peak at 1570 nm decreased significantly. On the basis of these facts, the peaks at 494 and 734 nm are attributed to the electronic transitions of in situ generated $N^{\bullet+}$, and the NIR peak to the IVCT transition. A similar absorption pattern has previously been documented for bis-triarylamine radical dication species.[105, 106] In principle, the IVCT band should disappear completely when both neutral amines are oxidized. However, because the potential required to induce the second-electron oxidation is relatively high, $[1]^{\bullet+}$ could not be completely converted to $[1]^{2+}$ before decomposition, and we could not observe complete disappearance of the IVCT band in Figure 3.8b. Previously, we reported the spectral changes of 1 on stepwise addition of $SbCl_5$ and failed to observe the IVCT transition.[79] The above spectroelectrochemical measurement proved that an intense IVCT transition did exist for $[1]^{\bullet+}$, and the use of $SbCl_5$ was clearly inappropriate for 1 due to the possible

complexation of SbCl$_5$ to the free coordinating sites of bpy. Figure 3.9 shows the spectral changes of 2–4 on oxidation with SbCl$_5$ in dichloromethane (the spectroelectrochemical results are presented below). Oxidation of rhenium complex 3 was described previously[79] and is also included for comparison. When these complexes were subjected to one-electron oxidation with SbCl$_5$, the ILCT and MLCT transitions decreased, and similar N$^{\bullet+}$-associated absorptions in the visible region to those of [1]$^{\bullet+}$ appeared (582 and 788 nm for [2]$^{\bullet+}$, 574 and 800 nm for [3]$^{\bullet+}$, 562 and 800 nm for [4]$^{\bullet+}$). At the same time, some broad NIR transitions were found to increase. When more oxidant was added to induce the second-electron oxidation of these species, the intense peaks around 800 nm continued to increase, while the broad NIR bands decreased gradually until they disappeared. It is noteworthy that a clear shoulder peak emerges around 1000 nm in Figure 3.9b, which can be assigned to the Ru$\rightarrow$N$^{\bullet+}$ electronic transition. The broad NIR transitions associated with the one-electron-oxidized species are somewhat unusual. In addition to a major band around 1300 nm, some shoulder bands on the low-energy side are distinctly evident. One possibility is that these NIR bands consist of a single IVCT transition and some low-energy vibronic structures that are observable in some class II/III or III MV systems.[107, 108] However, as was pointed out by a referee, the separation of the absorption maxima between the major band and the low energy shoulder band is quite large (>2000 cm^{-1}), which seems an unusually high-frequency mode to be significantly coupled to the electron-transfer process. In addition, triarylamine MV systems do not generally show resolvable vibronic structures. Solvatochromic studies also do not suggest that the singly oxidized forms of complexes 2 and 3 are class III systems. Another possibility is that more than one distinct NIR transition is indeed present in these systems. They may possibly be associated with the optically induced electron transfer between two amine units with and without the involvement of the metal centers. The above spectral changes of 2–4, including the appearance

and disappearance of the IVCT bands, could also be reproduced in spectroelectrochemical experiments, as was done for diamine ligand 1. Figure 10 compares the NIR absorption spectra as a function of wavenumber of $[1]^{\bullet+}$, $[2]^{\bullet+}$, $[3]^{\bullet+}$, and $[4]^{\bullet+}$ obtained in spectro-electrochemical experiments in both dichloromethane and acetonitrile. All compounds exhibit blueshift solvatochromism of the IVCT band in acetonitrile compared to dichloromethane. This phenomenon is commonly observed in most reported triarylamine MV systems.[62-64] However, the degree of the solvatochromism is different for each compound (1959, 1807, 1953, and 922 cm^{-1}, for $[1]^{\bullet+}$–$[4]^{\bullet+}$, respectively; Table 3.3). The free di-amine $[1]^{\bullet+}$ and complexes $[2]^{\bullet+}$ and $[3]^{\bullet+}$ have comparable solvatochromism, and iridium complex $[4]^{\bullet+}$ has the smallest solvatochromism. The small blueshifted solvatochromism of $[4]^{\bullet+}$ is very close to that of a class III triarylamine MV system bridged by 1,4-benzene (860 cm^{-1}),[109] and those of $[1]^{\bullet+}$–$[3]^{\bullet+}$ are slightly smaller than that of a class II tri-arylamine MV system bridged by para-$C_6H_4C{\equiv}CC_6H_4$ (2170 cm^{-1}).[110] Taking into account the shapes, energies (which are compared below), and solvatochromism of the IVCT bands of these systems, we tend to believe that the free diamine $[1]^{\bullet+}$ and complexes $[2]^{\bullet+}$ and $[3]^{\bullet+}$ belong to the class II systems. Iridium complex $[4]^{\bullet+}$ may be on the borderline between class II and III or close to a fully delocalized class III system, as reflected by the relatively small solvatochromic shift of its IVCT band. (Note: one should not speak of an IVCT band for a class III system, in which the valence is averaged. However, we use this term for simplicity, and it is acceptable to the MV community.) Oxidative experiments were also carried out on model complexes 5–8 with one amine group (Figure B.11 in the Supporting Information). When these compounds were subjected to one-electron oxidation, some new peaks around 800 nm appeared (776, 836, 850, 842 nm for 5–8, respectively). Similar absorption bands are present in $[1]^{\bullet+}$–$[4]^{\bullet+}$. These peaks are from the produced N$^{\bullet+}$ species themselves and they should not be ascribed to

44

electron transfers from the metal to the $N^{•+}$ species. Very similar absorption spectra were reported in the oxidative spectroelectrochemical experiments on Cu, Mn, and Ni complexes of ligand 5 by Lemaire and co-workers.[91]

We also previously observed a Ru→$N^{•+}$ transition of a MV system A (M=Ru, Figure 2) at a much lower energy (1360 nm).[50] In the NIR region (out to 2500 nm) of the absorption spectra for these model compounds (Figure B.11 in the Supporting Information), we could not observe any additional peaks. This fact rules out the possibility that the low-energy shoulder bands in Figure 3.9 for the diamine compounds are associated with the M→$N^{•+}$ electronic transitions. Numerous theoretical models have been developed to interpret the IVCT bands of MV compounds.
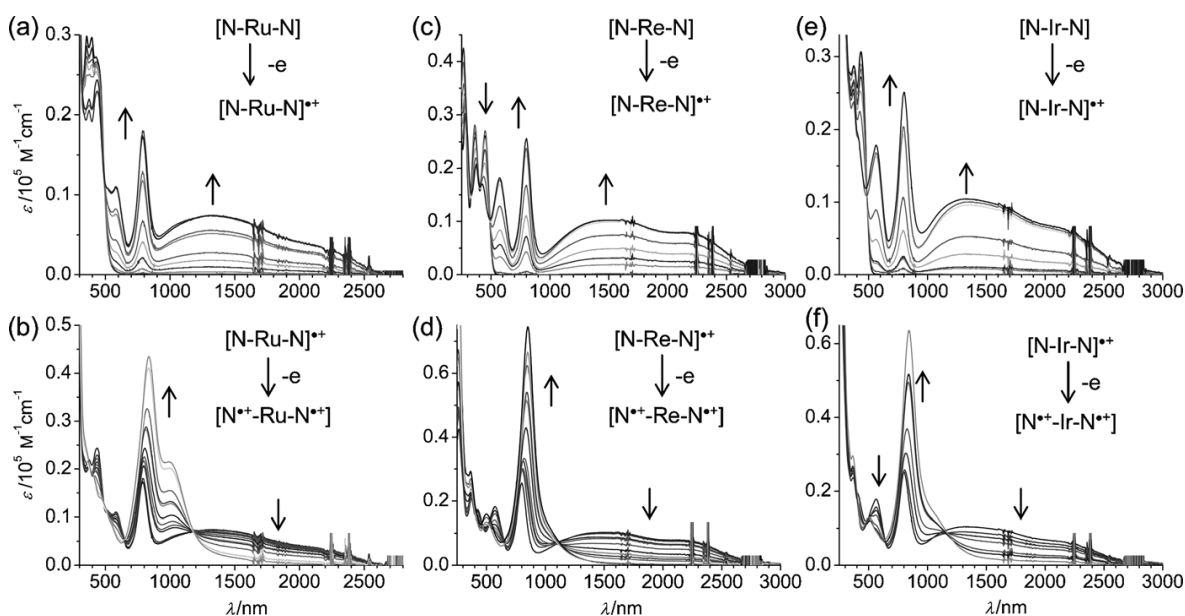
Figure 3.9. Absorption spectral changes of 2 (a and b), 3 (c and d), and 4 (e and f) in dichloromethane on one-electron (a, c, e) and two-electron oxidation (b, d, f) by adding different equivalents of $SbCl_5$ while keeping the concentration of 2–4 constant.

The most widely used are based on the Mulliken–Hush analysis,[111] in which two important parameters, namely, electronic coupling parameter H_{ab} and total reorganization energy λ, could be

quantitatively estimated for both organometallic and organic MV systems. For class II systems, $\lambda=E_{op}$, where E_{op} is the energy of the IVCT band maximum. The electronic coupling parameter H_{ab} can be estimated by [Eq. (3.1)], where μ_{ge} is the transition dipole moment of the IVCT band, R the diabatic electron-transfer distance, and e the elementary charge ($1.6*10^{-19}$ C). This equation is applicable to IVCT bands of any shape, and μ_{ge}/D can be calculated from the integrated absorbance ($\varepsilon/M^{-1}cm^{-1}$) of the IVCT band as a function of wavenumber $\tilde{v}$ via Equation (3.2).

$$H_{ab} = \frac{\mu_{ge}E_{op}}{eR} \tag{3.1}$$

$$\mu_{ge} = 0.09584 \times \sqrt{\frac{\int \varepsilon d\nu}{E_{op}}}$$

The NIR bands of $[1]^{\bullet+}$–$[4]^{\bullet+}$ were analyzed on the basis of Marcus–Hush theory, and corresponding parameters are summarized in Table 3.3. The IVCT band of $[1]^{\bullet+}$ is well separated from the transitions in the visible region. However, those of $[2]^{\bullet+}$–$[4]^{\bullet+}$ strongly overlap with the intense peaks around 800 nm. Thus, they were deconvoluted into a number of Gaussian-fitted functions (red lines in Figure B.16 of the Supporting Information) for the absorbance integration. The μ_{ge} values of $[1]^{\bullet+}$–$[4]^{\bullet+}$ were calculated to be 6.2, 7.3, 7.0, 7.1 D, respectively, according to Equation (3.2). Their H_{ab} values were calculated to 830, 1200, 1170, 1230 cm^{-1}, respectively, according to Equation (3.1), where R is taken to be the calculated N-N distance. These data suggest that complexes 2–4 have enhanced electronic couplings over 1, and iridium complex 4 has the largest coupling. However, as pointed out by many studies,[112] the true diabatic electron transfer distance is much shorter than the geometric distance between two organic redox sites due to the extensive delocalization of the diabatic states. Besides, the μ_{ge} and H_{ab} values were obtained by integrating over the whole NIR absorption. These values are rather tentative depending on what

part of the NIR transition is taken as the IVCT band. The $\tilde{v}_{max}/2$ value, which corresponds to the

H_{ab} value for a class III system, is also given for these compounds. It is clear that the H_{ab} value

obtained via Equation (3.1) for the nearly class III compound [4]$^{\bullet+}$ is much smaller than the

corresponding $\tilde{v}_{max}/2$ value (=4084 cm^{-1}), which suggests that the true diabatic electron-transfer

distance is indeed much shorter than the geometric distance. In addition, the H_{ab} value for [1]$^{\bullet+}$

(830 cm^{-1}) is somewhat smaller than that of a bis-triarylamine compound with a biphenyl bridge

(1550 cm^{-1}) reported by Lambert and co-workers and calculated using the same method.[62] Table

3.3 also gives the DFT computed H_{ab} values (see Figures 3.5 and 3.6), which gave a consistent

result, that is, complexes 2–4 have enhanced electronic coupling and iridium complex 4 has the

largest coupling. However, the calculated H_{ab} value for [1]$^{\bullet+}$ may be overestimated, likely due to

the difference in calculations with and without metal atoms. DFT calculations of the cationic states

of 1–4: To further study the electron delocalization of the one-electron oxidized complexes 2–4,

DFT calculations on [1]$^{\bullet+}$–[4]$^{\bullet+}$ were carried out. Since DFT methods tend to favor delocalized

states, hybrid functions such as B3LYP include a fraction of exact Hartree–Fock exchange to

balance delocalization and localization effects. Recently, Kaupp, Lambert, and coworkers

performed detailed theoretical calculations on a number of organic MV compounds[85] by hybrid

density functional methods with variable exact-exchange admixture combined with a continuum

solvent model. They found that, when an optimum of 35% of Hartree–Fock exchange was used,

calculations in the gas phase and with all solvents tested (acetonitrile, dichloromethane, and n-

hexane) resulted in spin delocalization for clear-cut class III systems. However, symmetry

breaking and charge localization were observed for class II systems with polar solvents such as

acetonitrile. These studies proved that the solvent effect is clear-cut in influencing the charge

character of organic MV systems. Thus, we performed similar calculations of [1]$^{\bullet+}$-[4]$^{\bullet+}$ in the gas

phase and solvents of different polarities (acetonitrile, dichloromethane, and n-hexane) with 35% Hartree–Fock exchange (see Experimental Section for details). The spin density (a–b) plots of these compounds are shown in Figure B.17 in the Supporting Information. The bisamine $[1]^{\bullet+}$ is delocalized in vacuum and n-hexane and acetonitrile. However, charge localization in one of the triarylamine units is evident in dichloromethane. For complexes $[2]^{\bullet+}$-$[4]^{\bullet+}$, distinct charge localization on one triarylamine is observed in both dichloromethane and acetonitrile. In case of rhenium complex $[3]^{\bullet+}$, asymmetric spin distributions in gas and n-hexane are evident as well. These results differ somewhat from the findings of Kaupp et al.,[85] because $[2]^{\bullet+}$-$[4]^{\bullet+}$ were experimentally determined to be more delocalized, albeit calculated to be less delocalized than $[1]^{\bullet+}$. One reason for this difference is that 1 is a neutral organic molecule, while 2–4 are transition-metal complexes, and they simply cannot be compared by the same calculation method. However, our results do agree that, when a polar solvent such as dichloromethane or acetonitrile was used for these calculations, spin localization and symmetry breaking did occur for non-class III systems. When the three complexes are compared, the rhenium complex $[3]^{\bullet+}$ appears to the least delocalized. This indeed agrees with the above experimental results, which showed that the IVCT of $[3]^{\bullet+}$ had the largest solvatochromic effect and the smallest H_{ab} value. TDDFT calculations of the cationic states of 1–4: To aid in the assignment of the visible and NIR transitions of $[1]^{\bullet+}$ – $[4]^{\bullet+}$ shown in Figures 8–10, TDDFT calculations were performed on the above DFT-optimized structures of these open-shell compounds. Similar level of theory (UB3LYP/ LanL2DZ/6-31G*) with the consideration of solvent effect (solvent=dichloromethane or acetonitrile) was employed for these calculations. Calculated low-energy excitations of these complexes are summarized in Table B.2 and corresponding frontier spin orbital involved in these excitations are shown in Figures B.14–B.17 in the Supporting Information. One common feature of these calculated results

is that two major absorption bands are predicted for all complexes in the NIR region in either solvent. The predicted lowest D_1 excitations are all dominated by a b-electron excitation from the highest occupied spin orbital (β-HOSO) to the lowest unoccupied spin orbital (β-LUSO) of individual compound (160B→161B for [1]$^{•+}$, 249B→250B for [2]$^{•+}$, 197B→198B for [3]$^{•+}$, and 249B→250B for [4]$^{•+}$.). These excitations are associated with the IVCT transitions for each compound. Although 160B and 161B of [1]$^{•+}$ have symmetrical configurations, the aforementioned frontier orbital for [2]$^{•+}$–[4]$^{•+}$ are clearly asymmetric and the spin locations switch from one triarylamine segment to another after excitation, which is in agreement with the nature of the IVCT transitions. In addition, electron redistribution on the bridge unit is also evident for all compounds on D_1 excitation. The predicted maxima of the IVCT transitions for all complexes are much more red-shifted than the experimental values. The predicted IVCT energies of [2]$^{•+}$–[4]$^{•+}$ are lower than that of [1]$^{•+}$, which is contradictory to previous experimental findings. Another contradiction between experiments and calculations is the IVCT energy difference of each compound in two solvents studied. As was discussed above, the $\Delta\tilde{v}_{max}$ values between acetonitrile and dichloromethane for [2]$^{•+}$ − [4]$^{•+}$ (particularly [4]$^{•+}$) are smaller than those of [1]$^{•+}$. However, [1]$^{•+}$ is predicted to have a slightly weaker solvatochromic effect (0.2 eV) than [2]$^{•+}$–[4]$^{•+}$ (0.3 eV). These contradictions again suggest that comparison of calculation results between a pure organic system and a transition metal complex should be made with great care. A second moderately intense band around 700–800 nm for all compounds is predicted. These predictions agree well with the experimentally observed bands (Figure 3.10). These bands are all associated with a b-electron excitation from a triarylamine-dominated orbital (159B for [1]$^{•+}$, 244B or 245B for [2]$^{•+}$, 193B for [3]$^{•+}$, and 242B or 243B for [4]$^{•+}$) to their β-LUSOs. They are associated with charge transfer from the triarylamine unit to the bridge segment and have nothing to do with the

metal components. These bands are also present in model compounds 6–8 after one-electron oxidation, as shown in Figure B.11 of the Supporting Information. For complexes $[2]^{\bullet+}$–$[4]^{\bullet+}$, some additional excitations with small oscillator strength are predicted in addition to the above-discussed two main bands. These weak excitations are predicted to be of MLCT character. These excitations are not observable in Figure 3.10. However, it is possible that they are embedded in the NIR envelopes and cannot be discerned due to low intensities.

3.4   CONCLUSION

We have prepared a series of 2,2'-bipyridine derivatives with two appended di-p-anisylamino groups as new prototype organic MV systems for studying metal chelation mediated electron coupling between organic redox sites. Model compounds with one di-p-anisylamino group and different metal components were also prepared and studied. Experimental and computational studies showed that the charge delocalization of organic MV systems could be enhanced by lateral metal chelation. The iridium complex exhibits the strongest coupling among all compounds studied. The singly oxidized forms of complexes 2–4 exhibit unusual absorption patterns, which evidence the presence of more than one distinct NIR transition. This implies that the underlying charge-transfer mechanism may differ from that of normal triarylamine MV systems due to possible involvement of the metal components. The nature of the IVCT transitions is supported by TDDFT calculations on these open-shell forms. Although the exact mechanism is not known at this stage, introduction of metal components into organic MV systems would give rise to new hybrid materials with impressive electronic properties, which will make them potentially appealing

materials for optoelectronic applications such as NIR electrochromic and/or photocurrent generation devices.[50]

4.0   CHARGE TRANSPORT IN IMPERFECT ORGANIC FIELD EFFECT TRANSISTORS: PHTHALOCYANINE MIXTURES AS CHARGE TRAPPING MODELS

This work is to be submitted for publication. Adam G Gagorik conducted the Monte Carlo simulation. Joel Gillespie and Xinfeng Quan collected the XPS and AFM experimental data, respectively. Xialing Chen was contributed for the rest of the calculation and experimental work. All authors discussed the result and were under the supervisor of Professor Geoffrey R Hutchison.

4.1   TRAP EFFECT IN ORGANIC SEMICONDUCTOR

As discussed in Chapter 1, charge transport in organic semiconductors is sensitive to impurities. There are two kinds of "impurities" as depicted in Figure 4.1: traps and barriers. For a hole transport, the introducing of a higher HOMO molecular site is to trap the host semiconductor molecule, while it work as a barrier (or "scatter" as in some other papers[113, 114]) if the "impurity" has a lower HOMO energy level than the semiconductor. Due to the weak Van der Waals interaction,[115] the charge transport in the organic semiconductors can be greatly hindered by impurities. Therefore, there are efforts trying to purify the materials, for example, it was reported by Palstra, et.al that the mobility of pentacene could be increased from 35 $cm^2 .V^{-1}.s^{-1}$ to 58 $cm^2 .V^{-1}.s^{-1}$ by removing significant amounts of impurities through vacuum sublimation. Besides the effort of reducing impurity sites through purification, there have also been work to decrease the

52

trap sites[116] with surface fictionalization and increase the charge transport. For example, an additional layer of silanes or some other polymer passivation layer is always deposited before growing n-type semiconductors, in order to reduce the electron trapping sites introduced by the silanol in the original SiO_2 substrate.
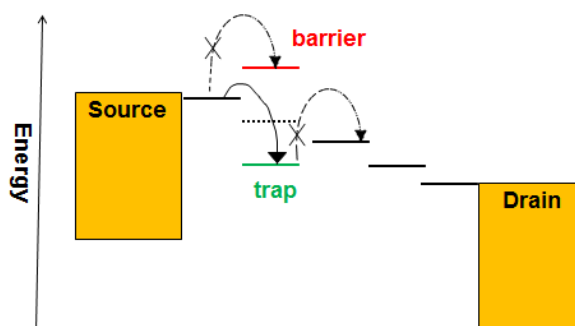
Figure 4.1. The schematic graph of introducing traps or barriers into semiconductor.

Negative differential resistance is a phenomenon that, unlike the regular electronic component that presents a positive resistance, the current decreases with increasing voltage. People are interested in negative differential resistance (NDR) due to the extensive applications in switching circuit and electronic oscillators.[117] The first observation of NDR was made in 1974 in a GaAs[118] sandwiched structure of double barriers. Since then, there have been quite a number of reports[119, 120] showing NDR effect, for example partially doped[119, 120] carbon nanotube. It is believed that the negative resistance occurred due to electronic barrier introduced at the p-n junction of diodes or chemical doping in semiconductors such as carbon nanotube.

In this work, the traps/barriers introduction was first time experimentally investigated with FET measurements of organic semiconductor films fabricated from solution. We used the molecule of Nickel (II) 1,4,8,11,15,18,22,25-octabutoxy-29H,31H-phthalocyanine (NiOBuPc) as the host site and (5,9,14,18,23,27,32,36-Octabutoxy-2,3-naphthalocyanine (OBuNc) as the dopant site. All of the pure and mixed films were fabricated from solution by spin-coating. To understand

how different amounts of "dopant" affect the charge transport to the host organic semiconducting system, we varied the concentration of the dopant molecule from 2.5% to 100%. The mobility was measured with FET measurements. And the effect of the dopant was studied by examining the concentration of dopants to mobility, and the result was compared with our computational work.[121] Moreover, we observed the NDR by introducing mixture sites of deep barriers experimentally and interpreted this phenomenon using the Monte Carlo simulation.

4.2 FABRICATION OF ORGANIC FIELD EFFECT TRANSISTOR DEVICES: PHOTOLITHOGRAPHY

4.2.1 Photolithography

The fast growth of semiconductor in the past several decades was brought about by reducing the cost per transistor, that is, scaling down the size, and therefore increasing the number of devices per chip. Ever since the 1960s, there have been extensive amounts of fabrication techniques emerging to create feature sizes from micron[122] to nanometer.[123, 124] Photolithography is a widely commercialized microfabrication method among these various techniques. It covers the critical size from nanometer to micrometer and costs much less than the finer resolution methods, such as e-beam lithography and scanning probe lithography. In addition to a good balance between critical size and cost, it is also easy to operate and scale-up in manufacturing.

The principle of photolithography is that a radiation sensitive photoresist is spin-coated on a substrate, and a mask with designed patterns shields the underlying photoresist when exposed to the UV light. Based on the type of mask and photoresist, the image on the mask will be written

directly to the photoresist or its negative image will be written. After exposure, the wafer is put in the solution of developer and the designed patterns appear on the wafer. There are two different kinds of photoresists: positive photoresist and negative photoresist. For the positive photoresist, once exposed to the UV light, it will become soluble in developer. Contrarily, the negative photoresist would become resistant to developer and stick to the substrate once exposed.

4.2.2 Etch vs. lift-off

There are two different schemes to fabricate a micro-device: etch and lift-off. The former is a subtractive process while the latter is additive. The principle of these two methods is depicted as in Figure 4.2.
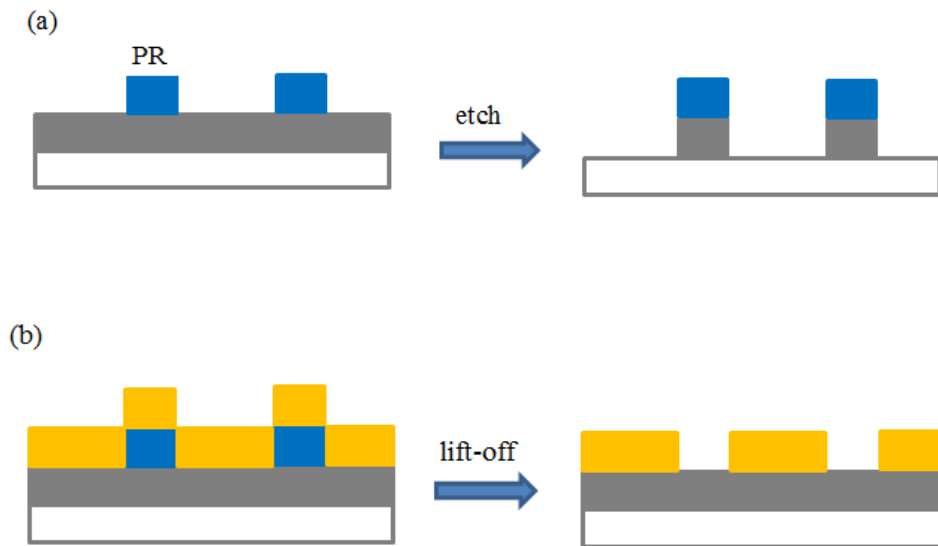
Figure 4.2. The scheme to depict how to fabricate devices with etch (a) or lift-off (b).

In etching, the pattern is protected by photoresist while the other area is exposed to the etchant. Based on what kinds of etchants are used, there are wet etching and dry etching. Etchant

solutions such as HF, KOH are used in wet etch while fluorine or chlorine vapors of CH_3F, SF_6 are normally used in dry etches. The pros and cons of these two processes are listed in Table 4.1.

Table 4.1. The advantages and disadvantages of the wet and dry etching process.

Etch Method	Pros	Cons
Wet etch	High selectivity, simple equipment, high throughput (batch process)	Isotropic, high chemical and waste disposal cost
Dry etch	Anisotropic, easy and cheap disposal of waste	Poor selectivity, complex instrument

For the process of lift-off, photoresist is sequentially spin-coated, exposed and developed to get the mirrored pattern. Then metal is deposited and washed with acetone. In the end, metal on the photoresist would be removed, and devices are left on the substrate.

Different combinations of mask and photoresist will be used depending on the design of process. For example, if devices are going to be fabricated by lift-off, positive photoresist and a dark mask (Figure 4.3) would be used so that the UV radiation passes through the pattern and the exposed photoresist would be dissolved in the developer and form the mirrored image. Similarly, to get a design after etching, a positive photoresist along with a clear mask is needed to get the exposed area etched.
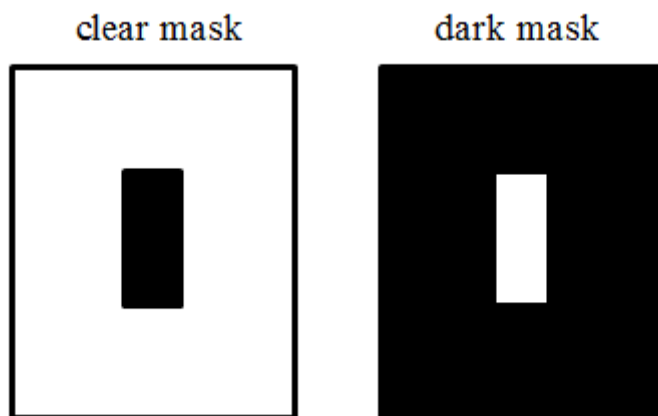
Figure 4.3. The two types of masks: clear vs. dark mask. For the clear mask, the pattern area is covered with metal and shielded against the UV radiation. While for the dark mask, the pattern area is clear and the rest is protected by metal.

4.3   EXPERIMENTS

MATERIALS. All essential chemicals and reagents were purchased from Sigma-Aldrich and used without further purification. Their chemical structures are shown in Figure 4.4. The substrates were made of silicon wafers with 300 nm dry thermal oxidized SiO_2 (<0.005 Ω.cm, <100>) on top of the boron-doped 500-550 μm Si purchased from University Wafer.

INSTRUMENTS. The fabrication of microelectrodes was conducted in the Nanoscale Fabrication and Characterization Facility Center (NFCF) of University of Pittsburgh using conventional photolithography technique. FET measurements were performed using a Keithley 2612 Source Meter. The organic semiconductor films were spin-coated using the KW-4A spin-coater from CHEMAT Technology Inc. The electrochemistry analyzer was purchased from CH Instruments, Inc. Film thickness was measured with a KLA-Tencor Alpha-Step IQ surface profiler.

Atomic Force Microscopy (AFM) measurement was performed using an Asylum Research MFD-3D SPM. Probes with Ti/Pt coated on a silicon tip (AC240TM, Asylum) with a first mode resonance frequency of 70 kHz, and a normal stiffness of 2 N/m were used. Topography and phase images were recorded. Roughness and section data was obtained from the default analyzing software. X-ray photoelectron spectra (XPS) were collected on an in-house custom-built instrument utilizing a Leibold EA10 hemispherical energy analyzer operating with a constant 50 eV pass energy. The experiments were performed at a base vacuum of 10^{-9} Torr or better and used the Ka line of Al for X-ray excitation (1487 eV). Samples were cleaned with a 5kV Ar ion gun prior to analysis. XPS background was subtracted using the Shirley method, and theoretical sensitivity factors were used for quantitative analysis.
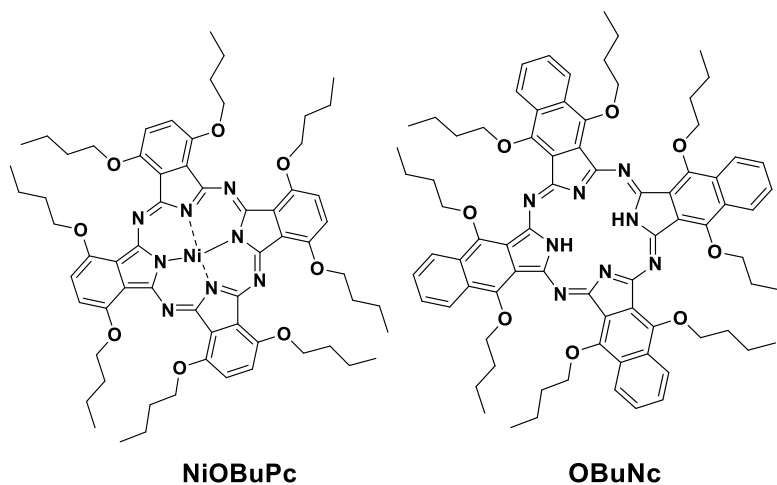
Figure 4.4. The chemical structure of nickel(II) 1,4,8,11,15,18,22,25-octabutoxy-29H,31H-phthalocyanine (NiOBuPc) and (5,9,14,18,23,27,32,36-octabutoxy-2,3-naphthalocyanine (OBuNc). The two structures differ in both metal center and peripheral ligand substitution.

EXPERIMENTS. Microelectrodes for FET measurements were fabricated for bottom-contact devices with 70 nm of Au with 3 nm of Ti as the adhesion layer was deposited onto silicon

wafer. To improve signal, interdigital microelectrodes were used with 50 µm long and 450 µm wide channels (Figure C.1). The backside of the wafer was scratched to be conductive and attached to aluminum foil to connect to the gate probe. Details of the fabrication of FET devices are included in Appendix C.

Before depositing the semiconducting films, the bottom-contact devices were pretreated as follows: sonication in acetone for 30 s, followed by immersion in piranha solution (2:1 by volume of concentrated H_2SO_4 and H_2O_2) for 2 h, rinsing with ultrapure water, blowing with nitrogen and then immersing in the octadecyltrichlorosilane (1% in toluene) for 3 h. Finally, the devices were rinsed with toluene and dried with nitrogen before spin-coated. Pure and mixed solutions of NiOBuPC / OBuNc (17.4mM combined total concentration in toluene) were spin-coated on the substrates. Samples were stored in vacuum overnight before characterization.

Electronic Structure Calculations. The molecular orbital and frontier energies were obtained after optimization of the geometries, using density function theory[80] (DFT) with B3LYP function[33] in Gaussian 09. The basis set was 6-31G for C, N, O, H and LANL2Z pseudo potential[34] was used for the metal.

Monte Carlo Transport Simulations. Our group has developed a coarse-grained Monte Carlo hopping model to study charge transport in thin film OFETs and OPVs.[121, 125, 126] In this work, we have used the model to predict the effect of traps, barriers, and defects on OFET current-voltage characteristics (IV curves), to gain deeper understanding of the experimental results.

4.4   RESULTS AND DISCUSSIONS

After the films had been made, physical and electrical characterizations were performed to collect information of morphology, electrochemistry and mobility.

Surface Profiler. Four kinds of films were spin-coated, and the thicknesses were measured with surface profiler. It was found that the pure NiOBuPc and OBuNc films were 200 nm thick on average while the thickness of the mixed 40% and 60% NiOBuPc films were 100 nm. However, as charge transport occurs mainly in the first several layers[127] near the interface of semiconductor and insulator, all films are thick enough to rule out the possibility that the mobility is going to be affected by the thickness.

Elemental Analysis. To make sure that the composition of the films is the same as the solutions prepared, XPS was used to confirm the weight percentage of the elements in the films. The results (Table D.1 in the supporting information) showed that the film had the same composition as prepared from the solution, indicating that the percentage of traps we introduced in the solution matched the ratio of mixture component in the films, themselves.

Energy Level. Gaussian computations were performed to predict the energy level theoretically, and hence determine the energy difference between the host site and doping semiconductors. The computational energy difference for the two materials is -0.028 eV for HOMO and -0.385 eV for LUMO, a much larger difference in LUMO than HOMO, which can be understood with the observation of orbital diagram in Table 4.2. It shows that the HOMO orbitals of NiOBuPc and OBuNc both have a major contribution from phthalocyanine and phenyl rings while the LUMO orbitals of these two molecules look quite different. The aromatic phthalocyanine rings still have a bigger contribution to OBuNc LUMO energy but in NiOBuPc, the LUMO orbital mainly locate on one of the octabutoxyl alkyl arm.
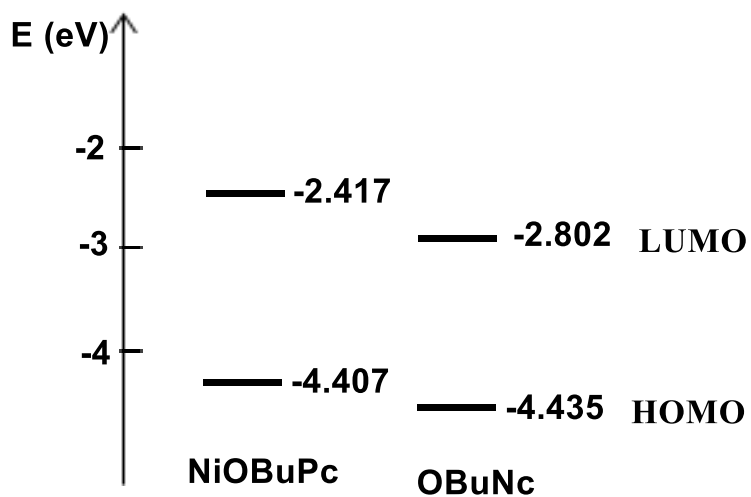
Figure 4.5. Energy level scheme for the NiOBuPc and OBuNc

Table 4.2. The diagram of frontier orbitals in NiOBuPc and OBuNc.

Molecule	NiOBuPc	OBuNc
HOMO		
LUMO		

We also used Differential Pulse Voltammetry (DPV) to experimentally measure the energy difference in HOMO. The difference of the first oxidation peak of NiOBuPc and OBuNc was 0.01 eV, close to the simulation prediction.
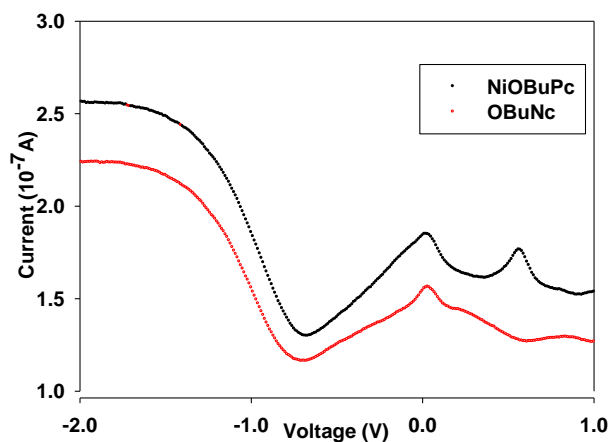
Figure 4.6 Differential Pulse Voltammetry of NiOBuPc (blue) and OBuNc (red). The concentration is 0.01 mM in the solvent of CH₂Cl₂. Reference electrode: Ag/AgCl; working electrode: glassy carbon; counter electrode: Pt

FET measurements. We scanned V_{ds} from 0 to -30 V and varied V_g (0, -5 V, -10 V, -15 V). The result showed that the material is a p-type semiconductor. With a specific gate voltage applied, I_{ds} increased linearly in the beginning and became saturated at large V_{ds}, typical of FETs.

The representative FET output graph.
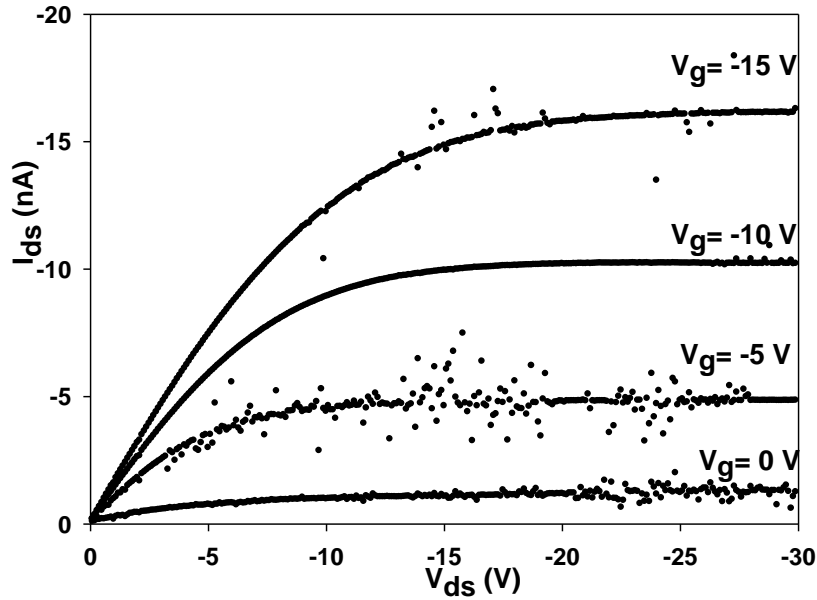
Figure 4.7 A representative output of FET measurement of NiOBuPc films

$$I_{ds} = \frac{WC_i}{2L}\mu(V_g - V_o)^2 \tag{4.1}$$

Field effect mobility can be deduced from equation 4.1, which describes the source-drain current in the saturation region. In equation 4.1, V_o is the extrapolated threshold voltage, μ is the field-effect mobility, W is the channel width, L is the channel length, and C_i is the capacitance per unit area of the insulating layer. The slope of a plot of $\sqrt{I_{ds}}$ vs. V_g is equal to the square root of $\frac{WC_i}{2L\mu}$, from which field-effect mobility can be calculated.

After calculating mobility of the pure and mixed films (Table D.3 in supporting information), we can examine mobility as a function of the percentage of the traps introduced. The plot is as follows:
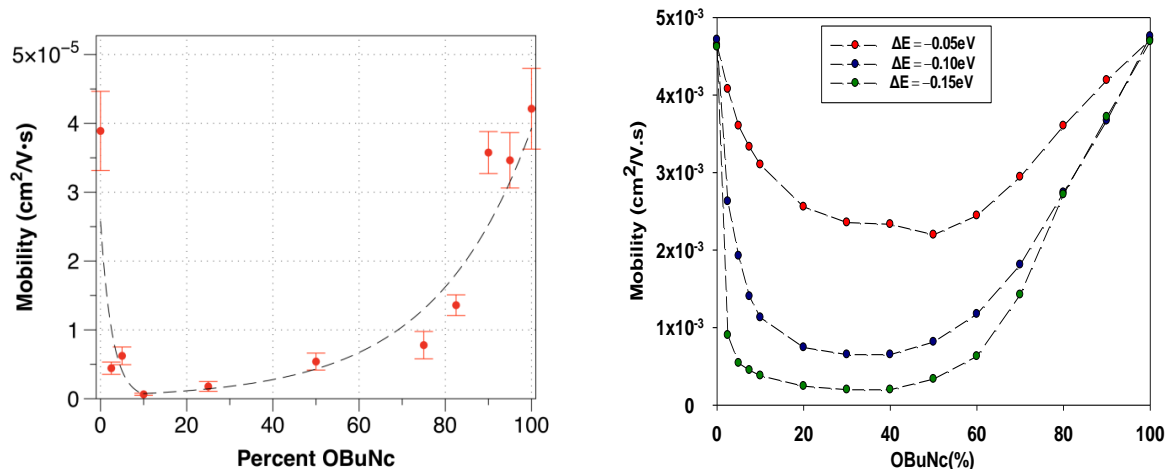
Figure 4.8 Mobility with the different amount of barriers in experiment (left) and simulation (right). Note that while the experimental electrochemistry suggest the OBuNc should be shallow barrier (i.e. -0.01 V) , comparison with the Monte Carlo transport simulations suggest the effect is much more significant, more like with deep barriers.

The asymmetrical trend of mobility agrees with the prediction of our simulation. However, it is unexpected that the experimental shallow traps behave like the deep barriers simulated.

Moreover, we found that in the mixed films, the I_{ds} decayed after it reached the saturation, which agrees with the prediction of the computation work[125] in our group by Hanwell, et.al. This negative resistance behavior is simulated to be achieved through the introduction deep barriers to hinder the conducting path in the semiconductor. It is discussed in detail in Appendix D.4.
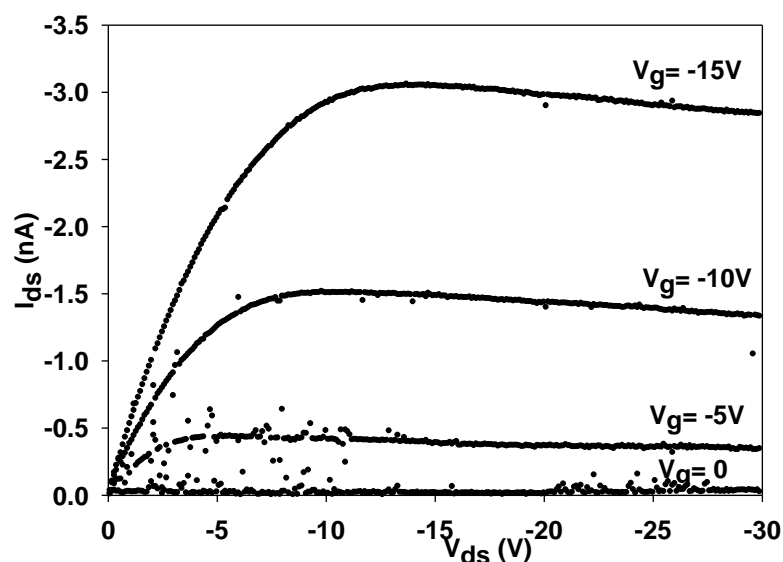
Figure 4.9 The output data of one 75% OBuNC film that showed the negative differential resistance.

AFM Measurements. Surface topology of the films with different composition was characterized by Atomic Force Microscopy (AFM) with tapping mode. Samples with OBuNc percentage of 0%, 25%, 50%, 75%, and 100% were chosen as models to see surface topology variety. As shown in Figure 4.11, surfaces of all five films are smooth with a small height roughness (1.5 nm for the OBuNc and around 0.3 nm for the other four samples) across 5 μm $\times$ 5 μm area. No observable crystalline domains were seen from both height and phase images (Figure D.5-D.6), indicating a homogeneous distribution of "traps" in the film at the scale of 5 μm $\times$ 5 μm.
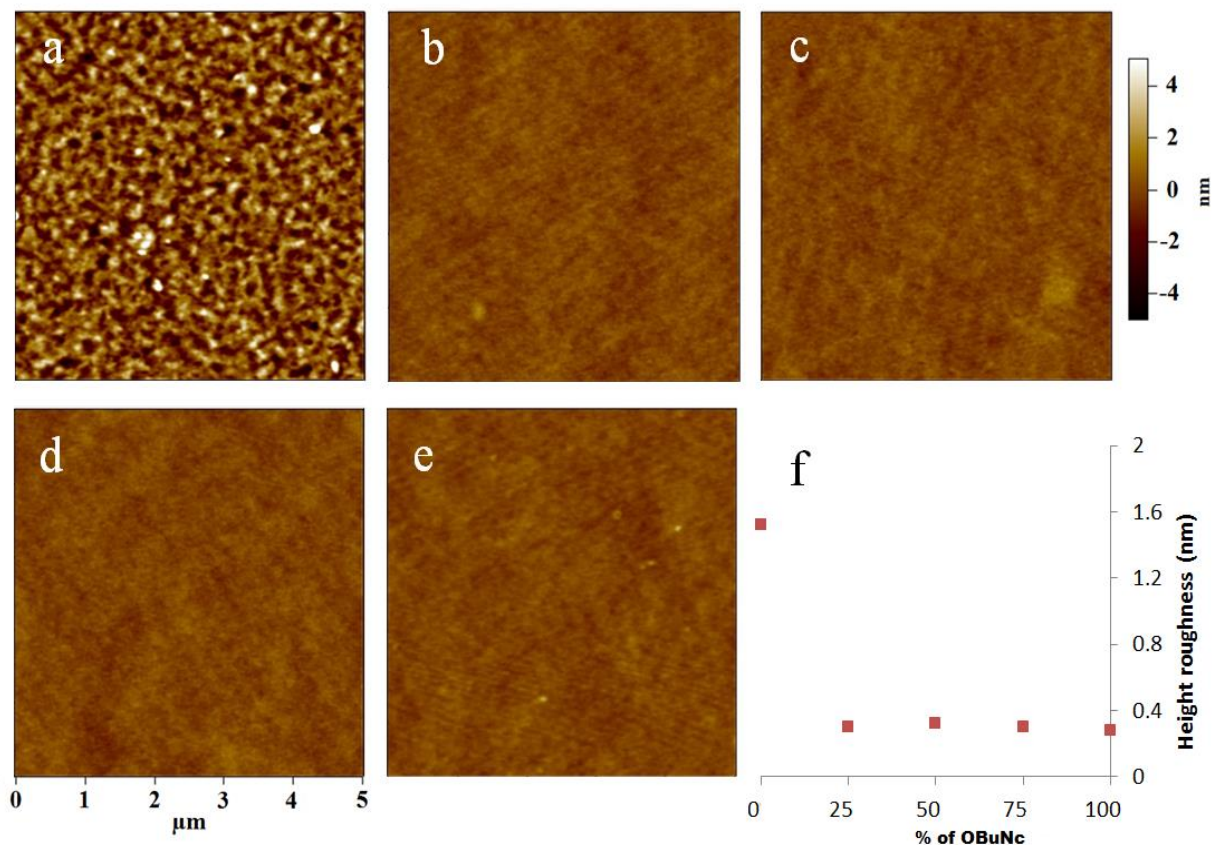
Figure 4.10 AFM height images (5 μm × 5 μm) of samples containing OBuNc a) 0%, b) 25%, c) 50%, d) 75%, and e) 100%. Height roughness is 1.52 nm for 0%, 0.30 nm for 25%, 0.32 nm for 50%, 0.30 nm for 75%, and 0.28 nm for 100%.

Discussion. It was reported by Ma[113] that both traps and barriers would decrease the mobility but in a different extent. What they found is that traps reduced the mobility more than the barriers and it is due to the different mechanism of how traps and barriers work: By introducing traps, the semiconductor charge carriers would be trapped and couldn't move freely until there is a large enough thermal activation, therefore traps decrease the mobility a lot. However, in the introduction of barriers, the charge carriers are hindered by the barriers to some extent but most of them can still move freely in the film. There was another work[114] by Qiu`s group that the effect of traps and barriers were examined by doping host semiconductor material of 4,4'-N,N'-

dicarbazolebiphenyl (CBP) with three different semiconductors of various energy level differences as low barriers, deep traps and deep barriers. What they observed is that shallow traps and barriers decreased the mobility more than the deep dopants. And they proposed a mechanism that in the case of shallow traps/barriers, the energy barrier is not very big and the charge transport would still proceed in the regular hopping path between hopping site and trap site. However, if the energy barrier of the introduced dopants is big enough, the hole/electrons would avoid jumping to the trap sites and instead take a neighboring host-host site with an elongated path. Therefore, the mobility would not be significantly reduced. However, the simulation conducted in our group[121] predicted the behavior of traps and barriers differently. First of all, both the traps and barriers decrease the mobility and do not increase until a minimum is obtained. And the position of the minimum is related to the energy difference between the normal site and trap/barrier site. Second, it was shown that deep traps/barriers decreased the mobility more strongly than the shallow traps, which is contrary to the report of Qiu[114].

Our FET conductivity measurements show that the introduction of OBuNc decreased the charge transport in NiOBuPc strongly even though the morphology of the films did not look quite different, which agrees with the simulation. However, the shallow barriers in the experiment produced the asymmetrical mobility curve and NDR, both of which indicate the behavior of deep barriers predicted by the simulations.

4.5   CONCLUSION

We explored the effect of barriers to the charge transport in organic semiconductors processed from solution. The AFM topography and FET conductivity measurements show that by introducing controlled amount of barriers, there is not an obvious difference in morphology or domain size, but the conductivity changes significantly. It is found that 2.5% of OBuNc to NiOBuPc decreases the mobility by 90%, which is accordant with the simulation of deep traps, barriers, and defects. But what is different between the experiment and our simulation is that the shallow barriers in our experiment behave more like the deep barriers predicted in simulation. Both the graph of mobility with percentage of barrier and the observance of NDR in the experiment agrees with the simulation prediction of deep barriers, however, based on the energy levels of the two molecules, OBuNc should work as shallow barriers in the charge transport of NiOBuPc molecules. We could not explain this discrepancy at this moment. It may be because the introduction of shallow barriers affects the crystal alignment and decreases the electronic coupling in the semiconducting system.

Based on this work, we draw two practical conclusions for the organic semiconductors fabricated from solution. First, the introduction of a small amount of "impurities" reduces the mobility a lot, so it is important to purify the semiconductors and make the fabrication defect-free. Second, if people want to make devices with negative resistance, it is very easy to do: make a mixture of phthalocyanines like this. No need for photo-irradiation as reported previously[128].

5.0   IMPROVING COATING OF PHTHALOCYANINE FILMS FROM SOLUTION

This work is to be submitted for publication. Paula B Hoffmann collected the Kelvin Probe AFM data. Xialing Chen was contributed for the rest of the calculation and experimental work. All authors discussed the result and were under the supervisor of Professor Geoffrey R Hutchison.

5.1   INTRODUCTION

Phthalocyanines (Pcs) is a group of materials attracting more and more interest because of their wide-ranging applications in photodynamic therapy,[20] nonlinear optical application,[22, 23] field effect transistors,[129, 130] solar cells.[21, 39, 131] Phthalocyanine films are usually fabricated by thermal evaporation techniques[129, 132] because they cannot dissolve in most solvents. However, with chemical modification of the peripheral ligand, substituted Pcs can be synthesized to become soluble.[23, 39, 133] The octabutoxy[38] and tetrasulfonic[134, 135] acid, tetrasodium substituted phthalocyanines are two of those soluble in solution. To date, there are lots of techniques to fabricate films from solutions: drop-cast,[136] spin-coating,[137] Langmuir Blodgett,[23] inkjet printing.[138, 139] Among the many methods, layer-by-layer[133, 135, 140] (LBL) deposition is a method that makes use of the interaction between neighboring layers and can control the thickness of the films. The mechanism of the process is described in Figure 5.1. The first layer of molecule (molecule A) is adsorbed onto the substrate and then the second layer of molecule (molecule B) deposited on top of A because of the interaction between molecule A and B. Electrostatic attraction between positively and negatively charged polymers is the most widely used method to form LBL

films. It has been frequently used in biology and chemistry research to fabricate films from solution.

Molecule A   Molecule B
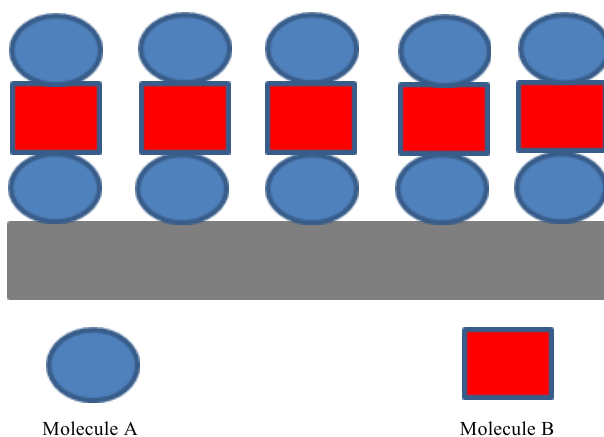
Figure 5.1. Schematic mechanism of how layer-by-layer films form

The mechanism of layer-by-layer is still under-explored compared to other methods like spin-coating and drop-cast. Due to the weaker electrostatic interaction, it[135, 140] is found that the layer-by-layer process is quite sensitive to experimental conditions of concentration of solution, choice of solvents, pH, ionic strength, etc. Therefore, it is important to study the factors that are critical to producing reproducible and uniform layer-by-layer films.

This chapter was designed to fabricate phthalocyanine films using layer-by-layer method and explore how to form good coating on glass and ITO substrates. The multilayer films were grown by alternatively dipping the substrates in sulfonated sodium substituted phthalocyanine solutions of pH 11 and pH 3. Based on the spectra, electrochemistry, morphology and surface potential information detected, it is found that

the critical factor to form LBL films is the trace amounts of PDDA in the water bath, which is different from a previous report[141] that the pair of different pH is the key for the LBL films from the sulfonated sodium substituted phthalocyanines.

5.2   EXPERIMENTS

Materials. All essential chemicals and reagents were purchased from Sigma-Aldrich. Copper phthalocyanine-3, 4′, 4″, 4‴-tetrasulfonic acid tetrasodium salt (CuPs) and Poly (diallyldimethylammonium chloride) (PDDA) (Mw<100,000 g.mol^{-1} , 35%wt.% in water) were used without further purification. Their chemical structures are shown in Figure 5.2. ITO slides (30-60 Ω/sq surface resistance) were also bought from Aldrich. Glass substrates (microscope slides) were obtained from VWR International.
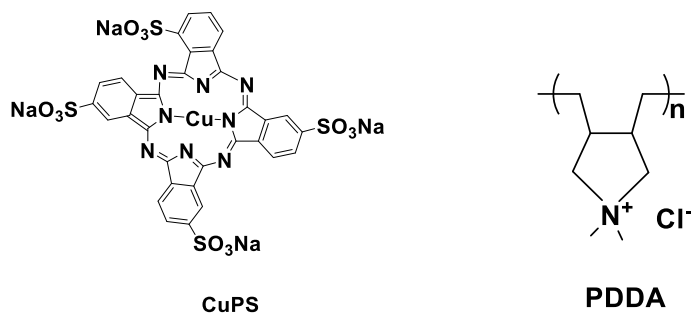
Figure 5.2. Chemical structure of the CuPs and polymer PDDA.

Instrument. The pH meter was purchased from Mettler Toledo. The UV spectra were collected with the HR 2000+CG-UV-NIR spectroscope from Oceanoptics with the light source of DH-2000-BAL.

Multilayer Preparation. Ultrapure water was used for all the experiments, which was obtained by an ion-exchange and filtration unit (Milli-Q Academic, Millipore Corp.). The resistivity is 18.2 MΩ•cm. After being rinsed in acetone and boiling water for 30 minutes, the glass substrates were dried with nitrogen gas, and immersed sequentially in 1:3 (30% H_2O_2: H_2SO_4) hot piranha and H_2O_2: NH_4OH: H_2O 1:1:6 (by volume) solutions for 30 minutes, rinsed in water, and blown dry with nitrogen gas. Before the immersion in phthalocyanine solutions, the substrates were treated with pH 3 PDDA solution for another 30 minutes, and then

washed in a water bath of 2 L for 30 s three times. For the ITO slides, the procedure is similar except that the substrates were treated with oxygen plasma in Plasma Cleaner or Reactive Ion Etcher or UV Ozone[142] Cleaner for 10 minutes instead of piranha solution.

The phthalocyanine solutions were prepared by dissolving 0.0163 g solute (CuPS, NiPS or the mixture of these two) in 10 ml water. A manual procedure[3] was used to grow each cycle of the LBL films: the substrate was immersed in the solution for 20 minutes, rinsed in the water bath for 30 s, dried with nitrogen gas, and immersed in the solution for another 20 minutes. For every two cycles, an absorbance UV spectrum was collected.

5.3 RESULTS AND DISCUSSION
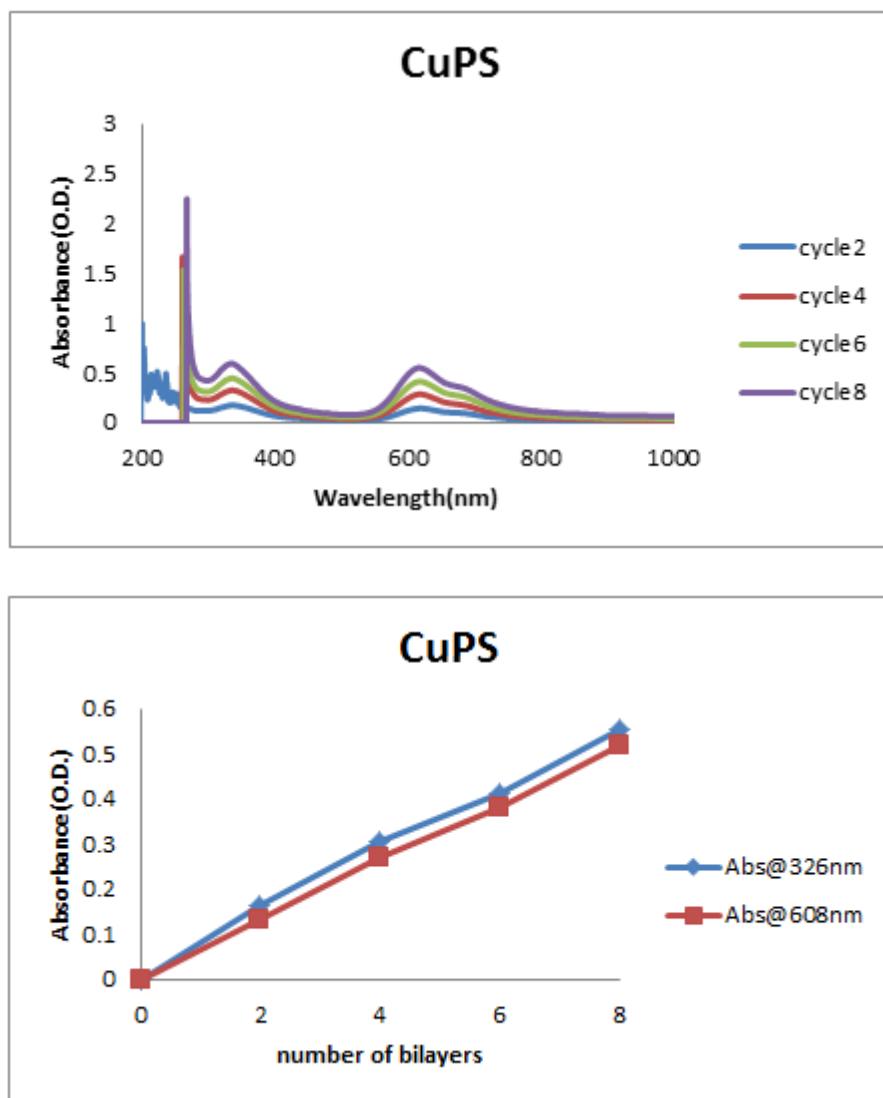
Figure 5.3 (top) UV-VIS spectrum for the slides cycled with the CuPS solution; (bottom) the height of the absorbance peak around 330 nm and 610 nm with number of bilayers.
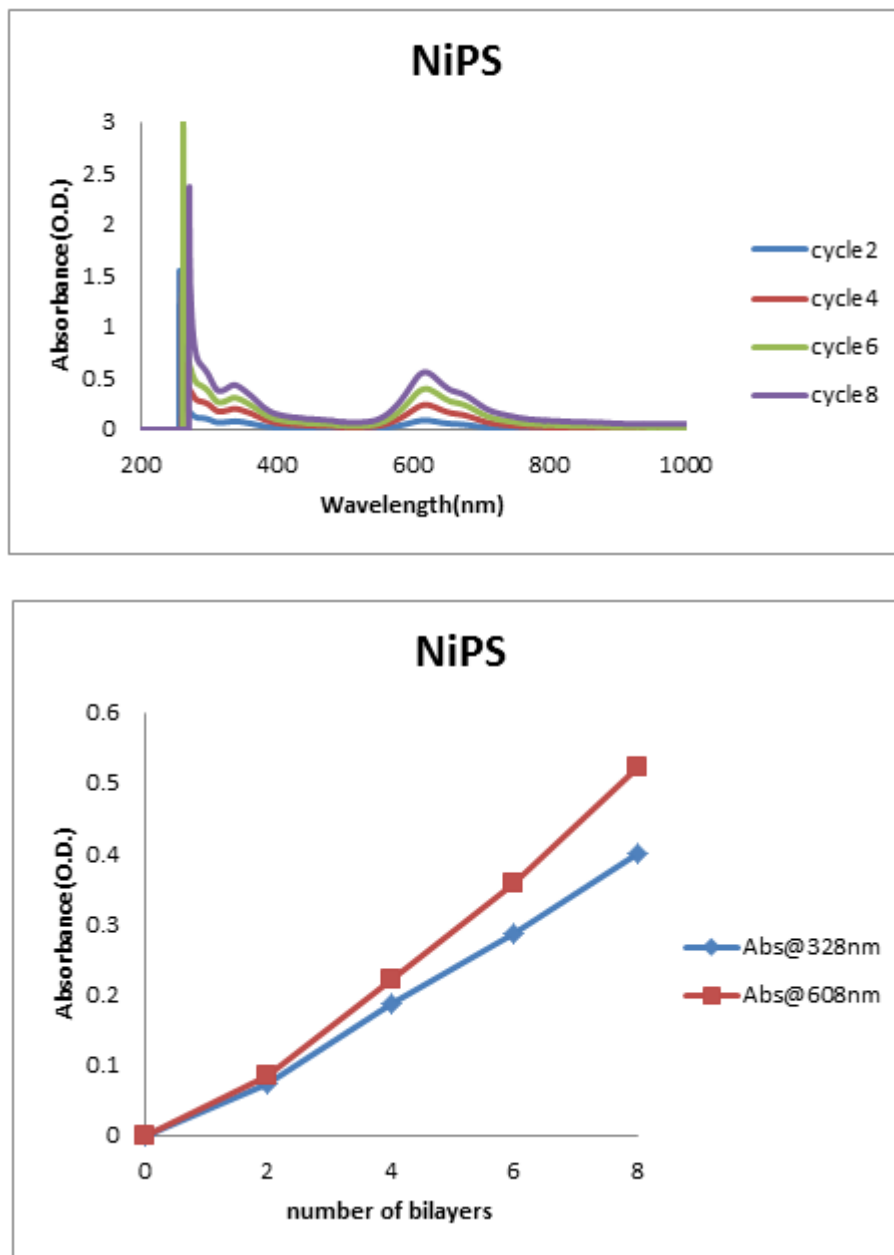
Figure 5.4 (top) UV-VIS spectrum data for the slides cycled with the NiPS solution; (bottom) the height of the absorbance peak around 330 nm and 610 nm with number of bilayers**.**

There are consistently two absorption peaks[143] for the CuPs and NiPs films. The one in the range of 600-700 nm, termed Q-band, is due to the electronic transition from HOMO to LUMO and responsible for the color of the compound. It is sensitive to the peripheral substitution and

environment. The absorption near 600 nm is for monomers while the absorption near 700 nm corresponds to dimers. The ratio of these two peaks indicates the information of aggregation in the films. The ultra-violet absorption is denoted as a Soret band, and mainly attributed to the transition between the deeper occupied energy levels (HOMO-1, HOMO-2, etc) to LUMO as illustrated in Chapter 2. The other mixed CuPs and NiPs (20%, 40%, 60%, 80% CuPs in Appendix E) films also show absorption of Q-band and Soret band. Moreover, solutions of different pH were also utilized and it was found that both pH 3 and pH 11 could produce LBL films, which means that pH is not the most important to grow LBL films as discussed by Bertoncello, et.al.[144] And we checked the water bath with and without PDDA to see how it affects the film process. The result is as in Figure 5.5.
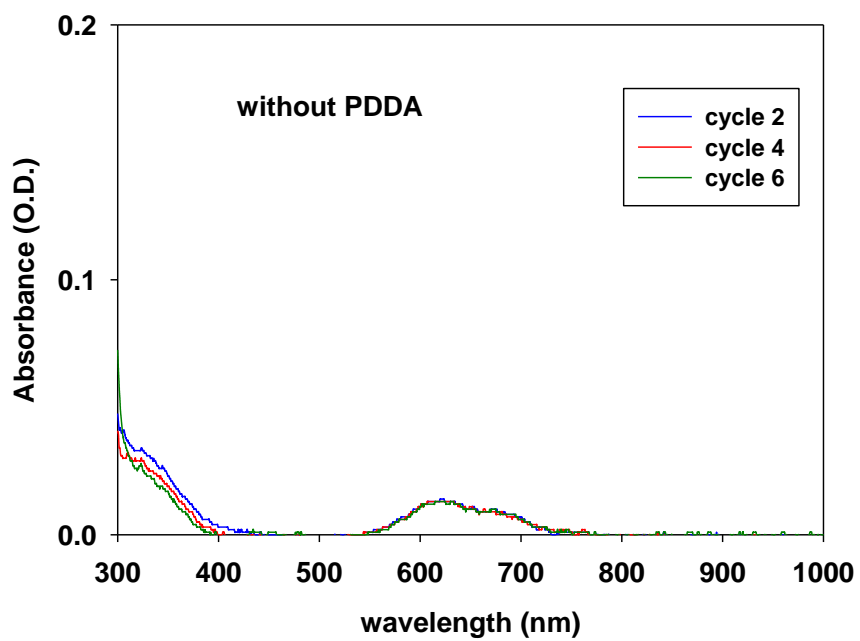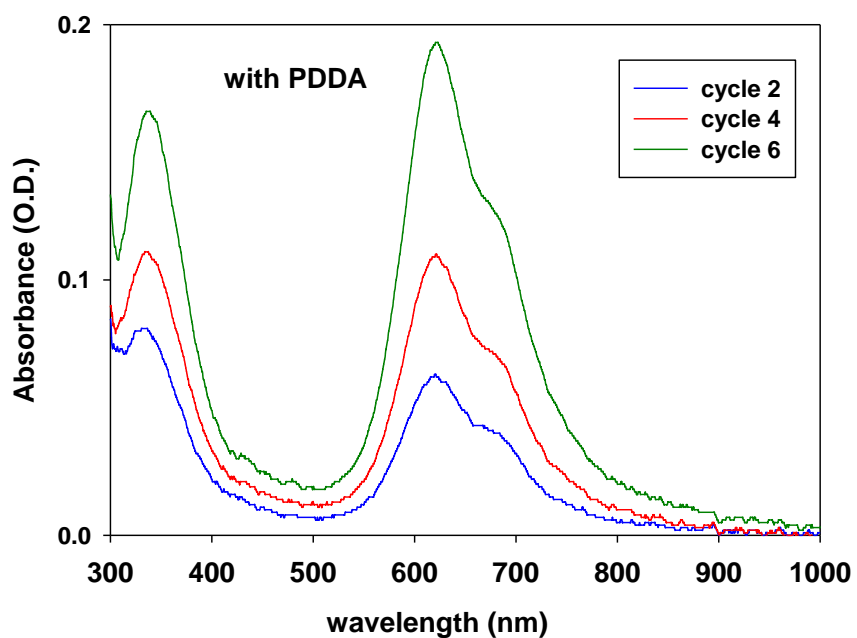
Figure 5.5. The UV-VIS spectrum of the glass slides immersed in the CuPs solution and rinsed with the PDDA water bath (top) and ultrapure water bath (bottom).

It is shown that a small amount of PDDA in the water bath is critical to get the layer by layer films. PDDA is a positively charged polymer while CuPs and NiPs aromatic complex are negatively charged. So it is reasonable that the trace amount of PDDA in the water bath helps attract the Ps and assist film to grow. The amount of PDDA in the water bath was quantitatively varied (Figure 5.6), and different pH was examined to see if they bring any difference to the UV-Vis absorbance.
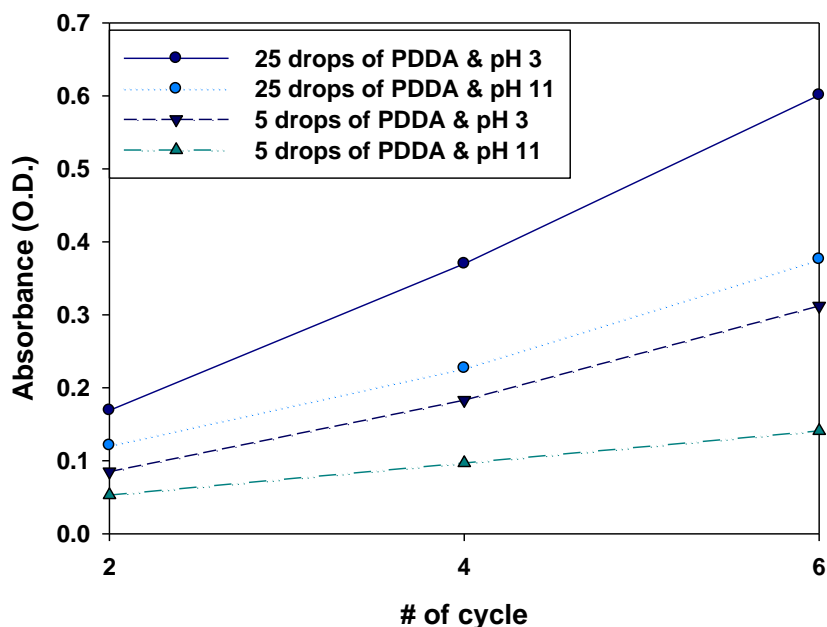
Figure 5.6. The spectra data of CuPs solutions of different pH (pH 3, pH 11) and varying amounts of PDDA in the water bath for absorption at 612 nm. The absorption of 328 nm is in supporting information.

It shows that more PDDA in the water bath helps grow the films. Moreover, pH 3 CuPs solution produces a thicker film than the pH 11 solution. To figure out the difference between the pH 3 and pH 11 CuPs solutions, the pH 11 CuPs solution was titrated to pH 3 to see if there is a

protonation by changing the pH. The titration curve shows that there is a sharp change in the pH of 10-4. It[145] was reported that in H_2SO_3 there are two protonation processes at pKa_1=1.85 and pKa_2=7.20, so the turning point in Figure 5.7 is believed to be the second protonation of H₂SO₃ ($HSO_3^- \rightleftharpoons H^+ + SO_3^{2-}$).
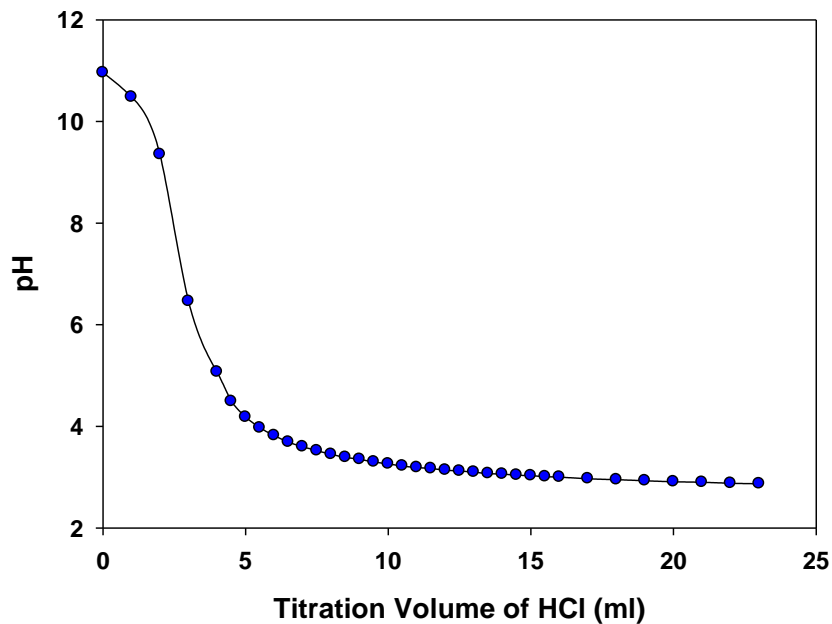
Figure 5.7. Titration curve of the CuPs solution (10 ml of 1.66 mM) with HCl of 2.4126 mM.

To further characterize the electrical and surface information of the films made of different solutions (pH, PDDA), Kelvin Probe AFM was used to collect the surface potential and morphology as in Figure 5.8 and 5.9.
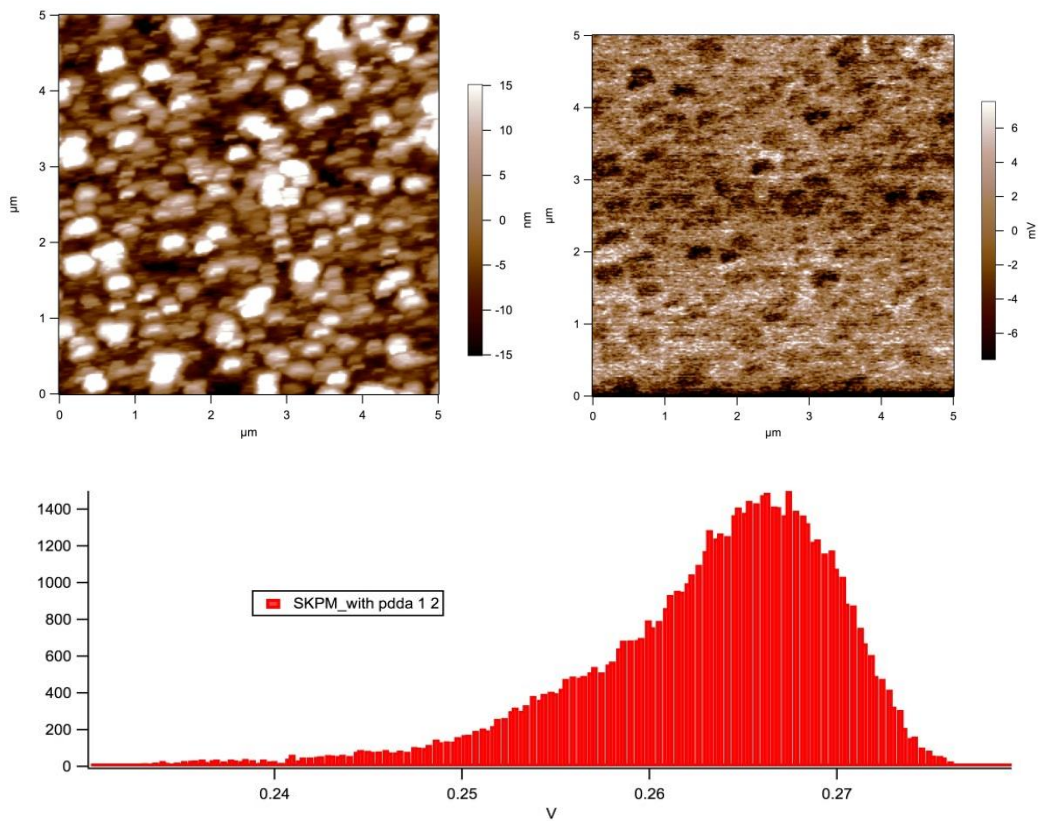
Figure 5.8 Morphology (top left) and surface potential (top right) plots of the film made from pH 3 CuPs solution and cycled in the water bath with PDDA. (Bottom) Histogram of surface potential image shown above before any image modification.
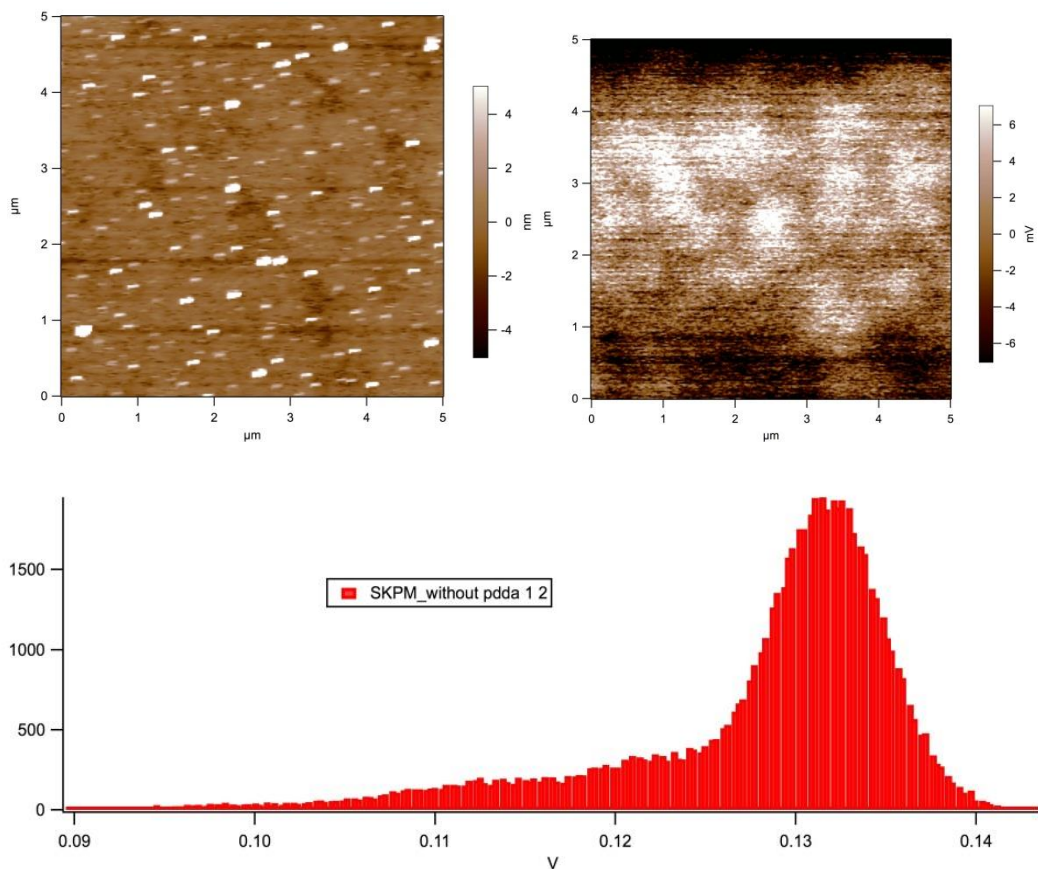
Figure 5.9 Morphology (top left) and surface potential (top right) plots of the film made from pH 3 CuPs solution and cycled in the water bath without PDDA. Histogram (bottom) of surface potential image shown above before any image modification.

By comparing Figure 5.8 and Figure 5.9, it seems that the films made from water bath with PDDA are thicker and more positive in surface potential than those grown from water bath without PDDA. It is because PDDA is a positively charged polymer and makes the surface more positively charged.

5.4 CONCLUSIONS

In summary, we have examined the mechanism of the layer-by-layer growth of CuPs films. The addition of PDDA and variation of the pH were studied, and it was found that a small amount of PDDA is the most critical factor to growing the layer-by-layer films. It was also found that a pH 3 CuPs solution tends to produce a thicker film than the pH 11 solution. Based on the titration of the CuPs solution, it was found that the sulfonic substitution on the phthalocyanine can be protonated or deprotonated by varying pH, therefore affects absorption of the films in different pH.

6.0   SUMMARY

In this dissertation, we explored the optical and electrical behavior of organic semiconductors by experiment and simulation. In order to electrically characterize the semiconductor films, we also fabricated transistor devices and studied how to improve the coating process from solution. To summarize, this work involves device fabrication, thin film growth, materials characterization, and computational interpretation. It enhances the understanding of the optical and charge transport behavior of organic semiconductors, and also provides guidance on potential semiconductor candidates for applications in LED, photovoltaic, transistor, etc.

Chapter 1 provided a brief introduction to the classical theories of charge transport in organic semiconductors and literature reports of experimental and simulation in terms of the temperature dependence, trap introduction, and optoelectronic performance.

Chapter 2 performed calculations to study how different metal and peripheral ligand substitutions affect the electrical and optical properties of phthalocyanine molecules. With the electrical and optical simulations of energy level, reorganization energy and optical absorption spectra, it was concluded that the optical and electrical properties of the phthalocyanines were tuned more with the peripheral substitution than the metal center.

Chapter 3 conducted the electrical and optical simulations of the triarylamine mixed valence systems bridged with different components. Four different MV complexes chelated with H_2, Ru, Re and Ir bridges were simulated. Molecular orbital and energy levels were obtained through DFT calculations. Electronic absorption was simulated with TDDFT simulations. Electronic coupling was computed based on the energy level, shape and solvatochromism of the

spectra. Experiments show that the metal chelation increase electronic coupling while simulations indicate that the ligand species delocalize the MV system more than the metal chelated species. The discrepancy may come from the different basis sets we used in the simulation for bridge with and without metals. But it is still quite accurate to help interpret and assign the electrochemistry and UV spectra data obtained in experiments.

Chapter 4 explored how the introduction of traps affects charge transport in organic semiconductors. Different amount of trap sites were intentionally introduced into the transport site, and the conductivity were measured. By plotting the mobility with the percentage of trap concentration, it shows that 2.5% of traps decreased the mobility by 90% and produced an asymmetrical graph as simulated. Moreover, we also observed negative differential resistance in the mixed films which was attributed to the block of the charge transport path. However, what was contradictory between the experiment and simulation was that our traps behave like deep barriers in the simulation though it was a shallow barrier considering the energy level difference detected in experiment and simulation. We suspected the discrepancy happens because the solution processed films are different in structure from the perfectly aligned crystal structure assumed in our simulation.

Chapter 5 discusses the layer-by-layer process of phthalocyanine films. Different parameters (pH, PDDA, composition) were examined to find out the critical factor to growing layer by layer films from sulfonated sodium phthalocyanines. It was found that the layer-by-layer films could be fabricated using one solution with either pH 3 or pH 11. The key to growing layer-by-layer films was that there must be PDDA in the water-bath.

To quantitatively study the influence of PDDA, we conducted experiments with different

amount of PDDA in the water bath and found that the films did not grow without PDDA and the amount of phthalocyanines adsorbed increase with the amount of PDDA in the water bath. To further understand the electrical and surface information of the PDDA assisted layer by layer films, Kelvin probe AFM was used to characterize the surface potential of the different films. A more positive surface potential was observed for the films with PDDA, which further demonstrates the existence of the positively charged polymer PDDA on the films.

Appendix A   SUPPORTING INFORMATION FOR CHAPTER 2

Appendix A.1   SAMPLE DFT INPUT FILE

The following is an example input file of nickel phthalocyanine DFT calculation to optimize the geometry with basis set of 6-31G and LANL2DZ.

```
%NProcShared=4

%Chk=nickel-phthalocyanine-opt.chk

#opt B3LYP/genecp


 nickel-phthalocyanine-opt


0 1
C       1.37841      2.91314     0.20998
C       0.25765      2.05549     0.16337
C       0.42937      0.65422     0.20685
C       2.67720      2.37602     0.29602
C       1.73386      0.14680     0.29830
C       2.24079     -1.15004     0.33868
C       3.93832      0.17580     0.39799
N       3.59815     -1.12666     0.38554
C       2.81515      0.98205     0.33881
N       5.25608      0.65467     0.40941
C       6.32152     -0.06331     0.40205
C       7.56506      0.48462     0.37190
C       8.46847     -0.54093     0.34831
C       7.93364      1.82451     0.33818
C       9.83936     -0.27077     0.29201
C       9.29610      2.12662     0.27332
C      10.25051      1.08410     0.25127
C       7.72564     -1.72214     0.36519
N       6.39248     -1.42227     0.38851
N       1.52838     -2.21831     0.29945
C       2.04932     -3.54251     0.30710
```

```
N       3.36048     -3.88441     0.33533
C       3.41188     -5.24002     0.30668
C       2.11948     -5.74789     0.24895
C      -0.10989     -4.80161     0.16657
C       1.62203     -7.05006     0.17867
C      -0.64032     -6.09822     0.09251
C       0.22144     -7.22097     0.10081
N       4.61221     -6.01736     0.28260
C       5.81584     -5.53683     0.29851
N       6.13151     -4.20985     0.34934
C       7.48695     -4.13705     0.32038
N       8.23212     -2.91689     0.33101
C       8.03519     -5.42289     0.21259
C       6.97730     -6.30357     0.20425
C       7.17778     -7.68953     0.07530
C       9.36128     -5.88225     0.08929
C       9.58409     -7.27155    -0.05032
C       8.49709     -8.17015    -0.05636
C       1.27254     -4.66840     0.24563
Ni      4.86364     -2.67337     0.37431
H      -1.71243     -6.23344     0.02596
H      -0.19942     -8.21518     0.04223
H       1.23530      3.98817     0.17942
H      -0.73727      2.48135     0.09484
H       9.60957      3.16247     0.23387
H      11.30047      1.33378     0.19549
H      10.59398     -7.65895    -0.15712
H       8.68237     -9.23579    -0.16739
H       2.28578     -7.90433     0.17657
H      -0.75560     -3.93092     0.15271
H      -0.42979     -0.00089     0.16382
H       3.53897      3.03199     0.32464
H       7.18626      2.60972     0.34641
H      10.56850     -1.06702     0.26526
H       6.34856     -8.38423     0.06002
H      10.20324     -5.20226     0.08371

Ni    0
S  3  1.00
      7.6200000          -0.4082550
      2.2940000           0.7455308
      0.8760000           0.5325721
S  4  1.00
      7.6200000           0.1872591
      2.2940000          -0.3966964
      0.8760000          -0.4954003
```

```
       0.1153000              1.0844343
S   1   1.00
       0.0396000              1.0000000
P   3   1.00
      23.6600000             -0.0481558
       2.8930000              0.6258473
       0.9435000              0.4715158
P   1   1.00
       0.0840000              1.0000000
P   1   1.00
       0.0240000              1.0000000
D   4   1.00
      42.7200000              0.0372699
      11.7600000              0.1956103
       3.8170000              0.4561273
       1.1690000              0.5621587
D   1   1.00
       0.2836000              1.0000000
****
C 0
6-31G
****
N 0
6-31G
****
H 0
6-31G
****
NI    0
NI-ECP    2    10
d potential
  3
1    469.9324331         -10.0000000
2     85.4236411         -69.4084805
2     21.2674984         -12.0951020
s-d potential
  4
0    162.1686097          3.0000000
1    176.5333232         22.0253618
2     68.9562010        443.0181088
2     13.5792838        145.5696411
p-d potential
  4
0     69.0181506          5.0000000
1    275.5955596          4.9882824
2     47.1315453        256.6945853
```

2   12.9874075   78.4754450

Appendix A.2   **TDDFT CALCULATION OF UV-VIS SPECTRUM**
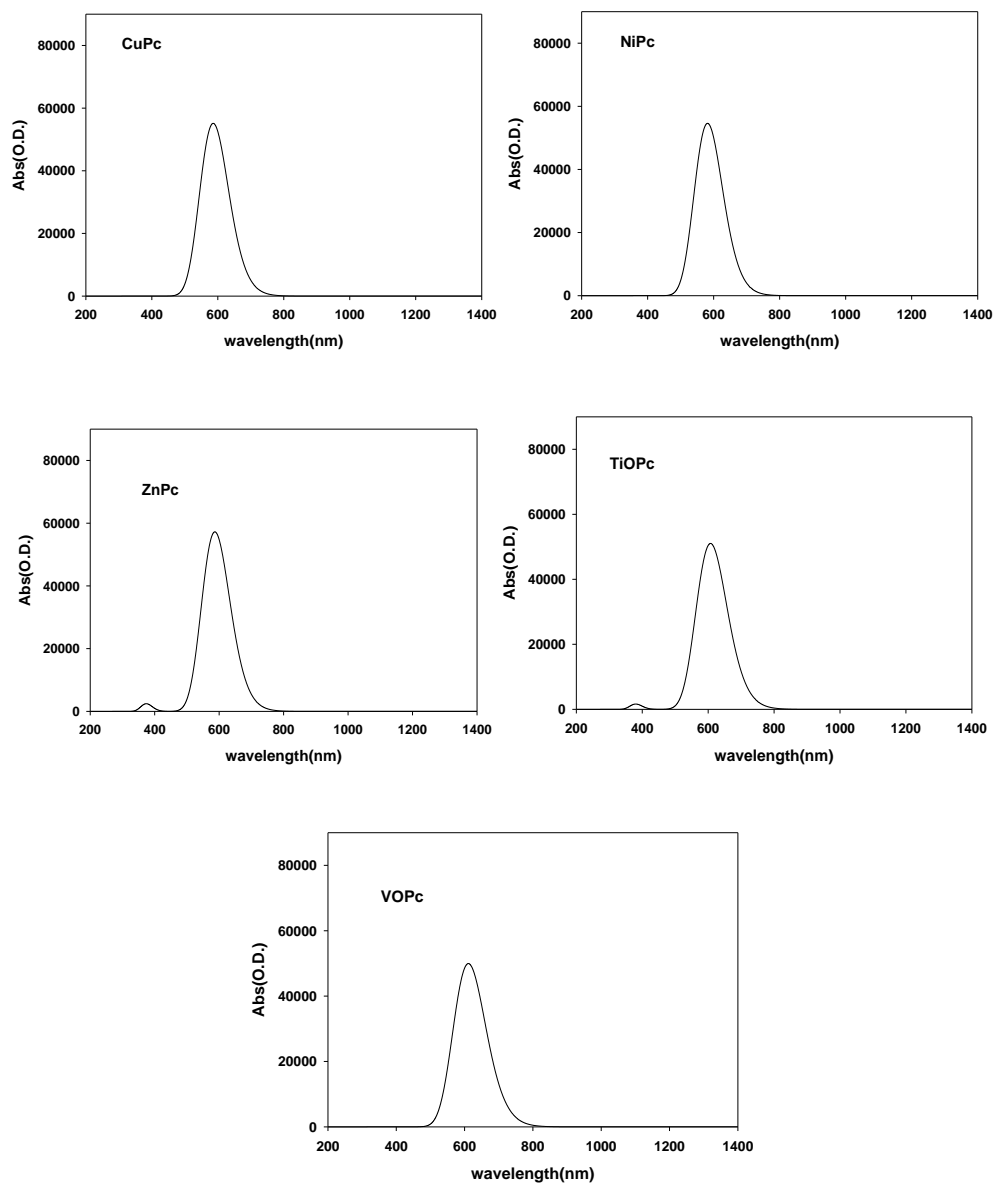
Figure A.1. Simulated electronic absorption spectra of phthalocyanine molecules with different metal centers.
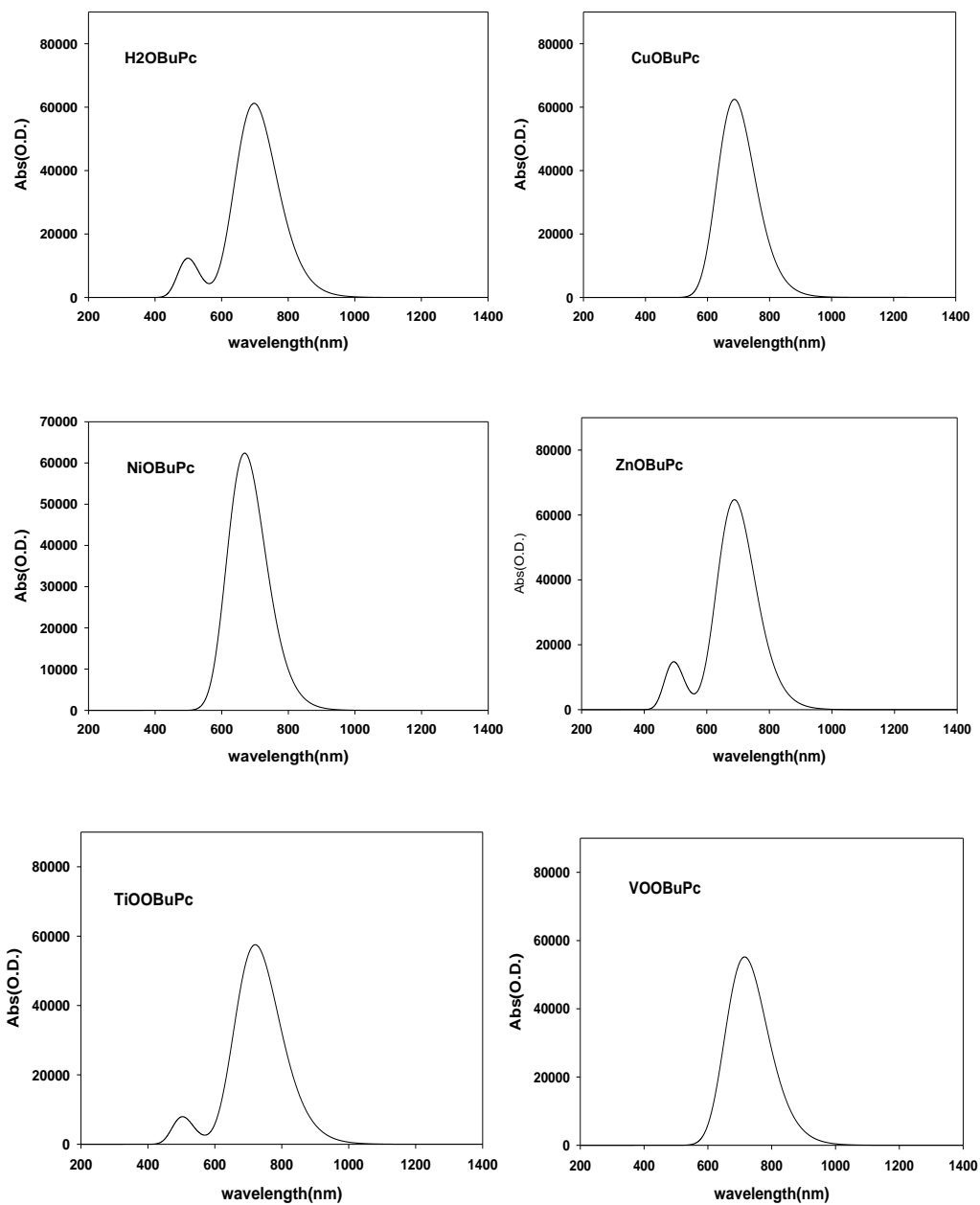
Figure A.2. Simulated electronic absorption spectra of octabutoxy phthalocyanine molecules with different metal centers.
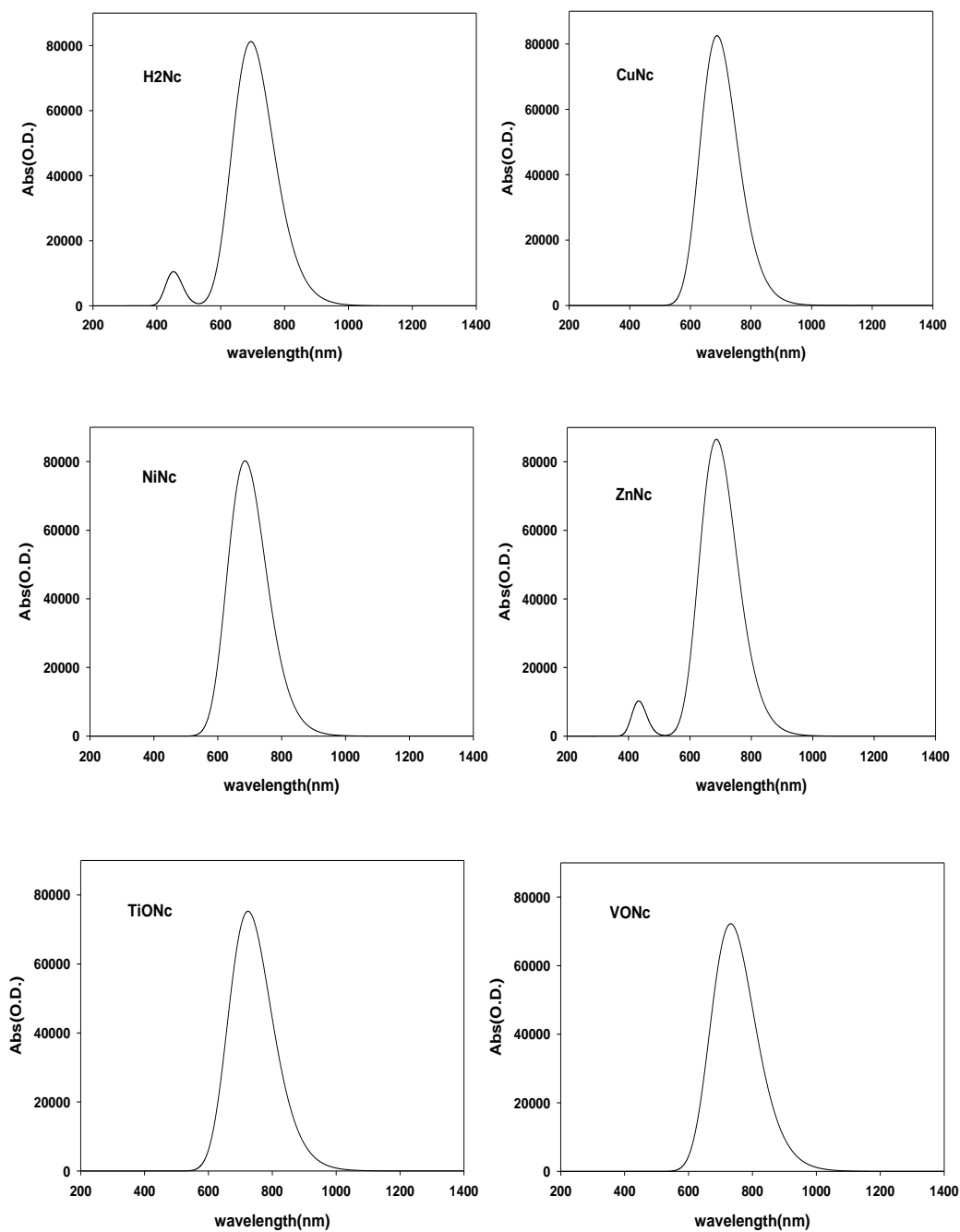
Figure A.3. Simulated electronic absorption spectra of octabutoxy phthalocyanine molecules with different metal centers.
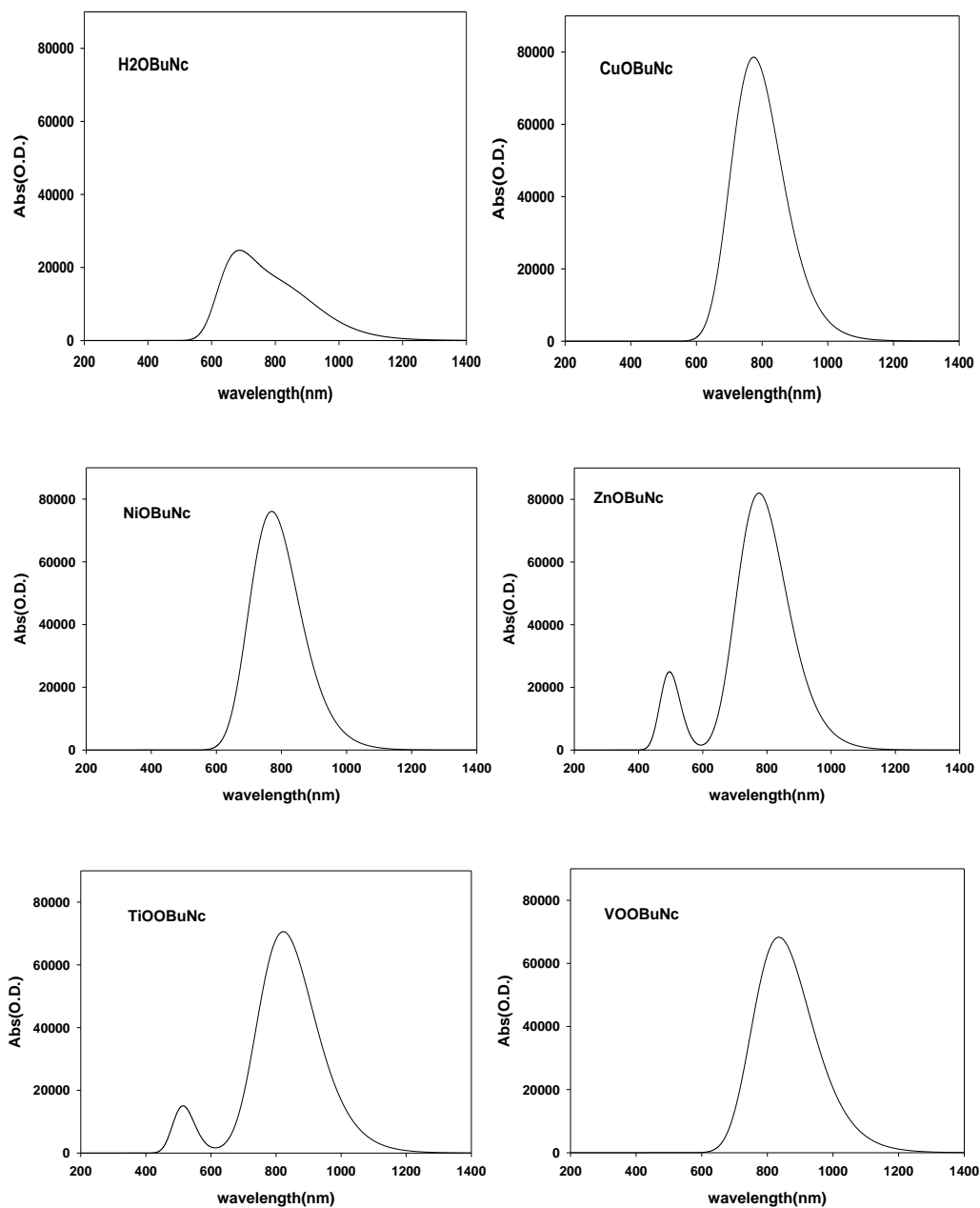
Figure A.4. Simulated electronic absorption spectra of octabutoxy phthalocyanine molecules with different metal centers.
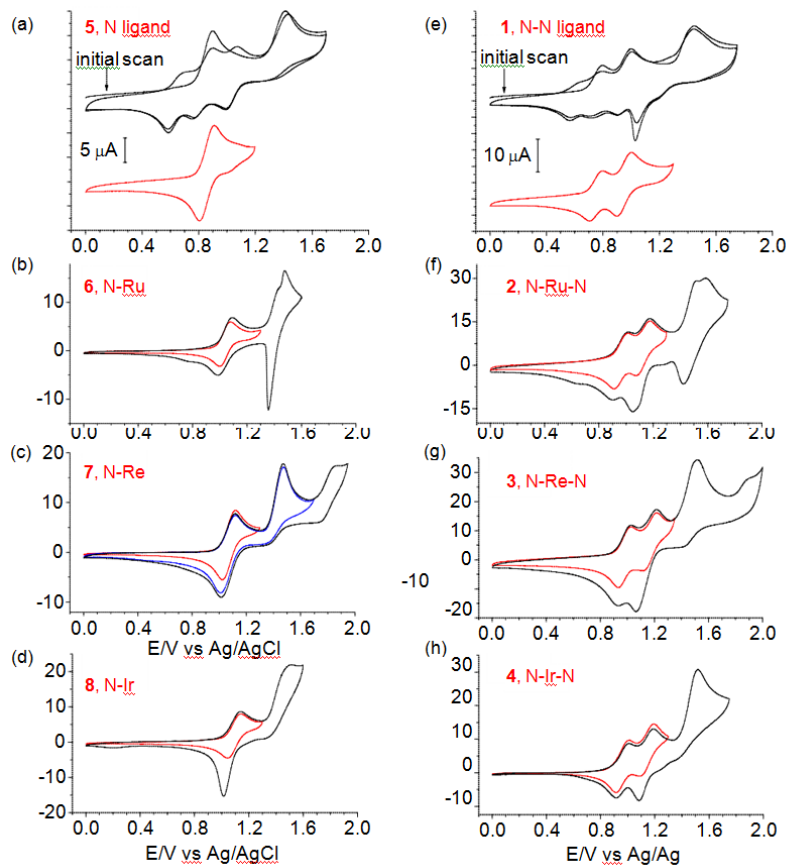
Figure B.1. Anodic cyclic voltammetric profiles of 1-8 in CH_2Cl_2 containing 0.1 M Bu_4NClO_4 as the supporting electrolyte at a scan rate of 100 mV/s.
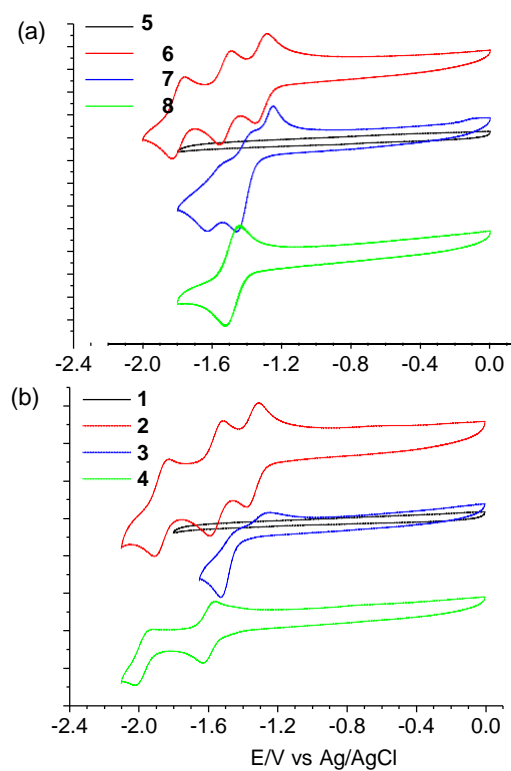
Figure B.2. Cathodic cyclic voltammetric profiles of 1-8 in CH_3CN containing 0.1 M Bu_4NClO_4 as the supporting electrolyte at a scan rate of 100 mV/s.

LUMO   HOMO
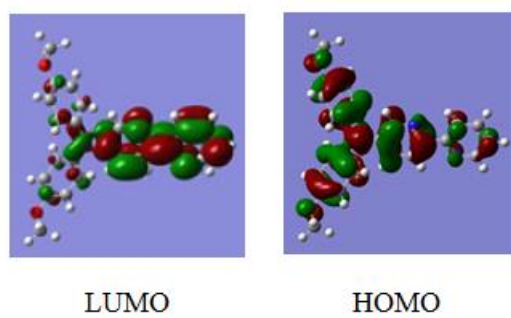
Figure B.3. HOMO and LUMO diagrams of 5.

LUMO+2 **LUMO+1** **LUMO**

HOMO **HOMO-1** **HOMO-2**
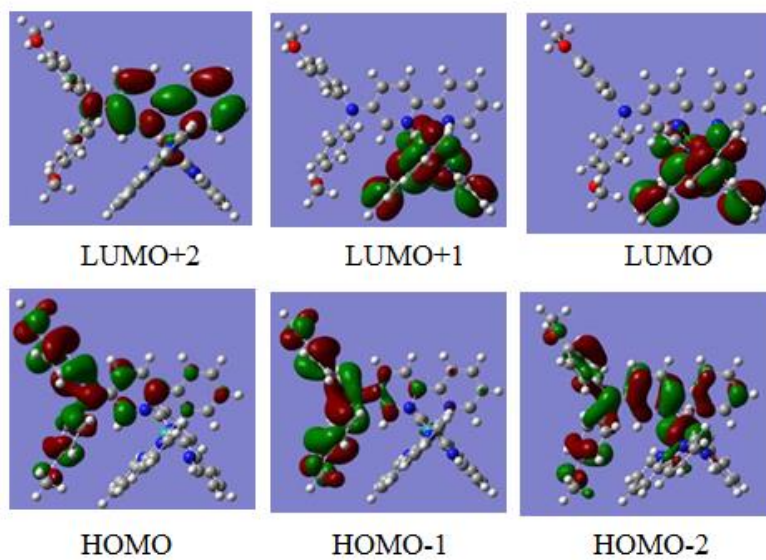
Figure B.4. Selected frontier orbital diagrams of 6.

LUMO **HOMO** **HOMO-1** **HOMO-2**
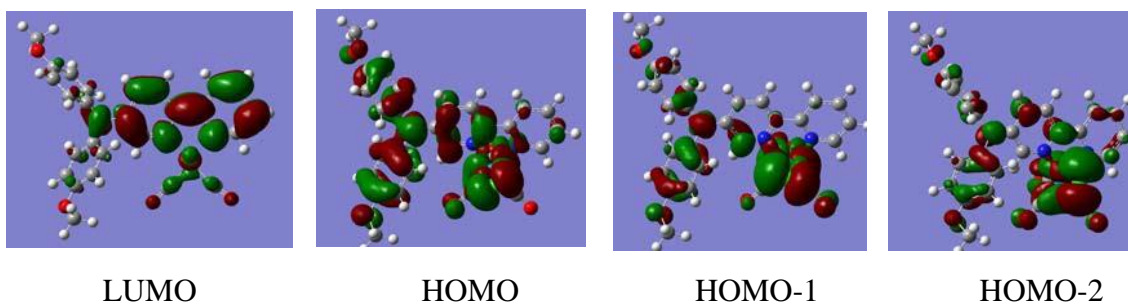
Figure B.5. Selected frontier orbital diagrams of 7.
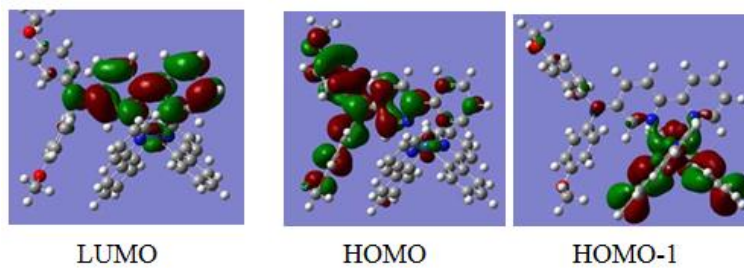
Figure B.6. Selected frontier orbital diagrams of 8.
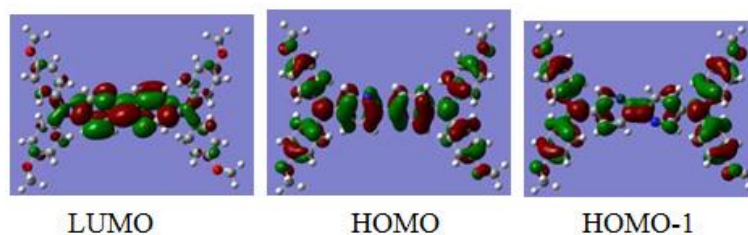
Figure B.7. HOMO and LUMO diagrams of 1.
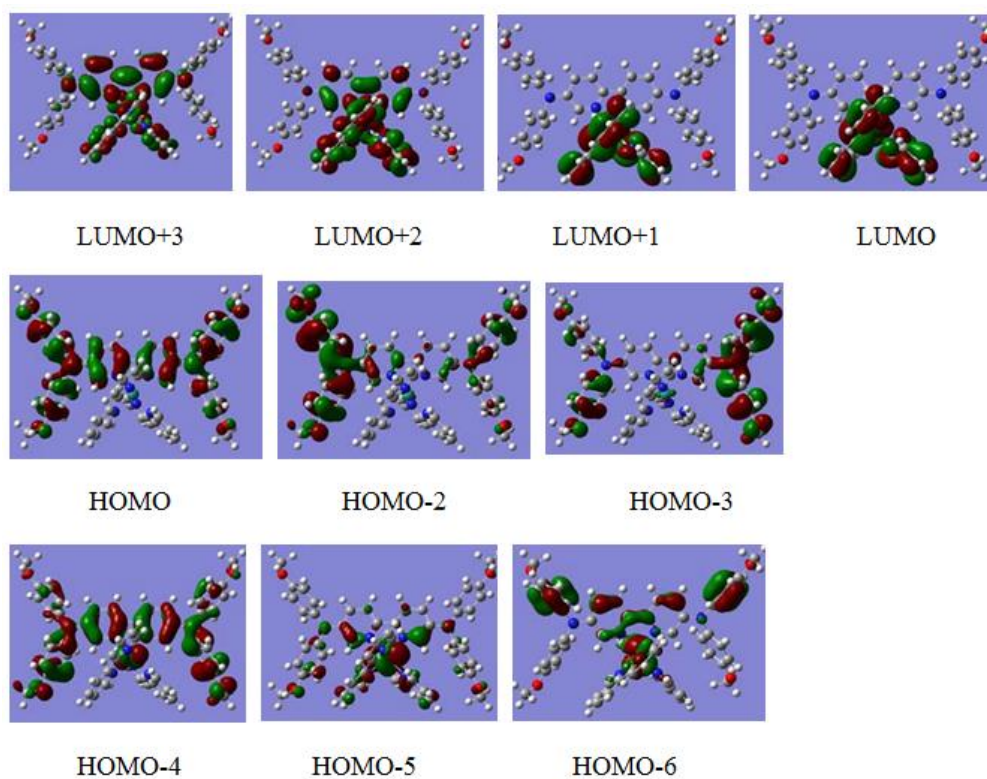
Figure B.8. Selected frontier orbital diagrams of 2.

LUMO+1   LUMO

HOMO   HOMO-1   HOMO-2
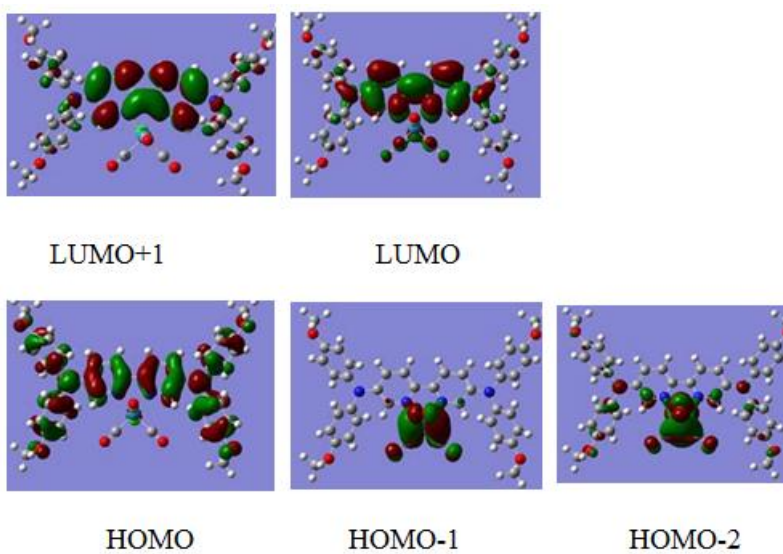
Figure B.9. Selected frontier orbital diagrams of 3.

LUMO+3   LUMO+2   LUMO

HOMO   HOMO-1   HOMO-2
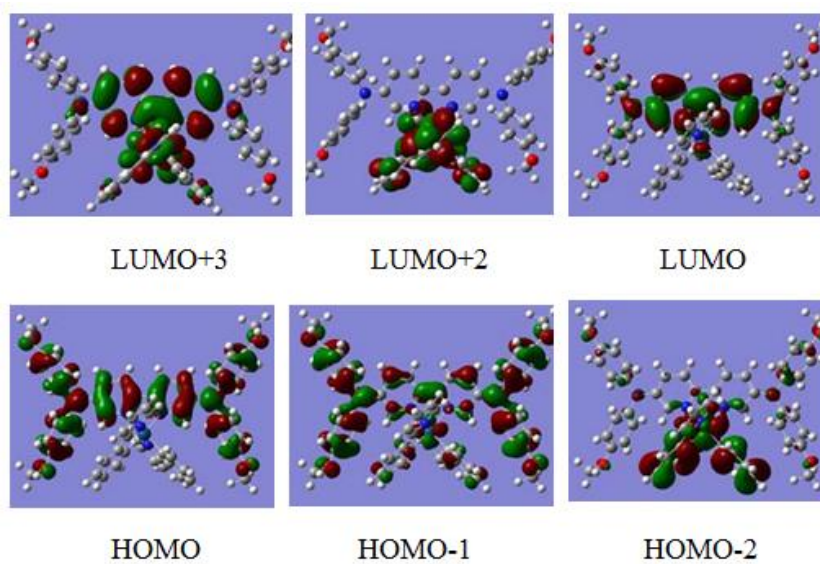
Figure B.10. Selected frontier orbital diagrams of 4.

Table B.1. Selected excitation energy (E), oscillator strength (f), dominant contributing transitions and the associated percent contribution and assignment of compounds studied. [a]

Compound	S_n	E/eV	E/nm	f	Dominant Transitions (contribution)[b]	Assignment
5, N ligand	1	3.28	377	0.55	HOMO → LUMO (88%)	ILCT
6, N-Ru	3	2.37	523	0.2056	HOMO → LUMO+2 (90%)	ILCT
	6	2.64	470	0.0029	HOMO-2 → LUMO (41%)	MLCT
					HOMO-2 → LUMO+1 (13%)	MLCT
					HOMO-3 → LUMO (17%)	MLCT
	7	2.65	467	0.026	HOMO → LUMO+3 (87%)	LLCT
7, N-Re	2	2.53	490	0.0506	HOMO-2 → LUMO (56%)	MLCT
					HOMO-1 → LUMO (18%)	MLCT
					HOMO → LUMO (21%)	ILCT
	3	2.81	441	0.325	HOMO-2 → LUMO (37%)	MLCT
					HOMO-1 → LUMO (20%)	MLCT
					HOMO → LUMO (31%)	ILCT
8, N-Ir	2	2.71	458	0.282	HOMO → LUMO (76%)	ILCT
					HOMO-1 → LUMO (12%)	MLCT
	3	3.03	410	0.035	HOMO-1 → LUMO (81%)	MLCT
					HOMO → LUMO (13%)	ILCT
1, N-N ligand	1	3.05	406	1.12	HOMO → LUMO (89%)	ILCT
2, N-Ru-N	5	2.36	526	0.056	HOMO → LUMO+2 (95%)	LLCT
	6	2.48	500	0.434	HOMO → LUMO+3 (89%)	ILCT
	9	2.57	483	0.0021	HOMO-5 → LUMO (15%)	MLCT
					HOMO-4 → LUMO (7%)	MLCT
					HOMO-3 → LUMO (12%)	LLCT
					HOMO-2 → LUMO (43%)	LLCT
	20	2.85	434	0.0605	HOMO-6 → LUMO+1 (25%)	MLCT
					HOMO-5 → LUMO (19%)	MLCT
					HOMO-6 → LUMO (30%)	MLCT
3, N-Re-N	1	2.56	484	0.0503	HOMO-1 → LUMO (80%)	MLCT
	2	2.69	461	0.60	HOMO → LUMO (62%)	ILCT
					HOMO-1 → LUMO (16%)	MLCT
	3	2.70	459	0.117	HOMO-2 → LUMO (81%)	MLCT
	6	3.27	379	0.316	HOMO → LUMO+1 (86%)	ILCT
4, N-Ir-N	1	2.61	474	0.598	HOMO → LUMO (87%)	ILCT
	7	3.12	397.4	0.154	HOMO-2 → LUMO+2 (36%)	MLCT
					HOMO → LUMO+3 (45%)	ILCT
	8	3.12	396.8	0.166	HOMO-2 → LUMO+2 (38%)	MLCT
					HOMO → LUMO+3 (46%)	ILCT

[a] Computed at the TDDFT/B3LYP/LanL2DZ/6-31G*/vacuum level of theory. [b] The actual percent contribution = (configuration coefficient)^2 ×2 ×100%.
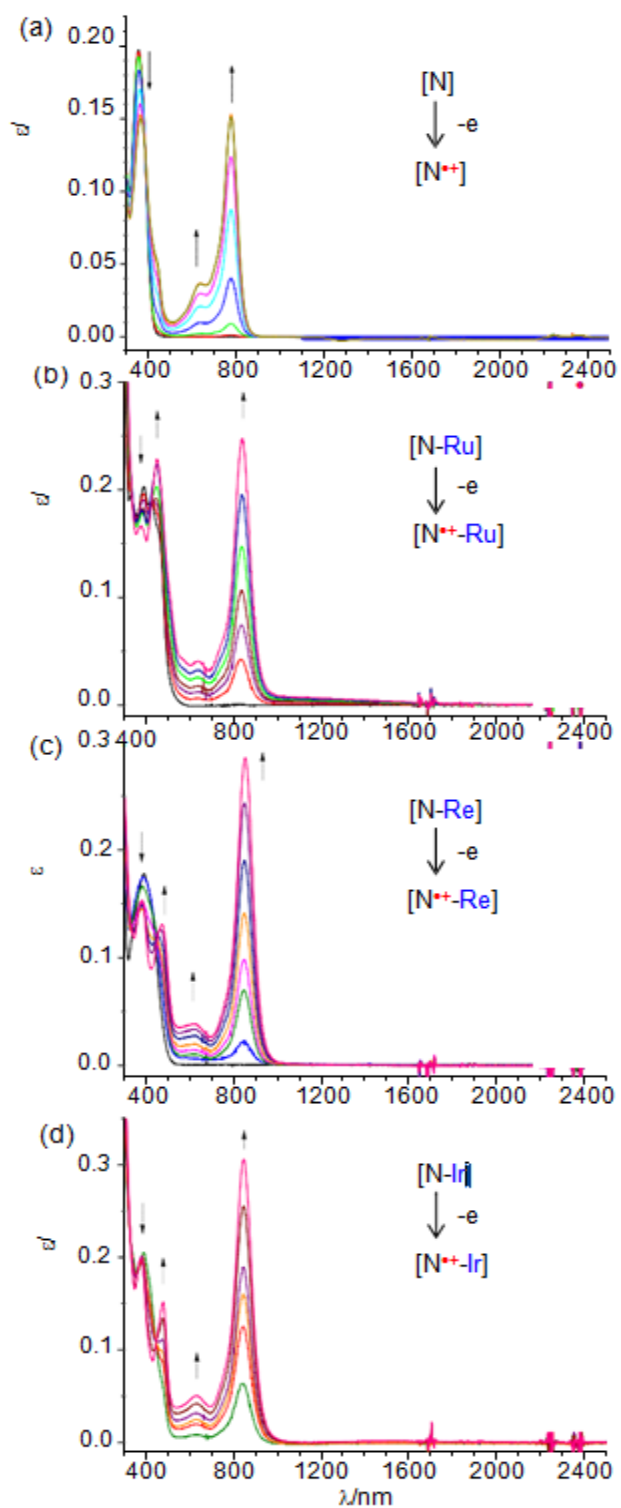
Figure B.11. Absorption spectral changes of 5 (a), 6 (b), 7 (c), and 8 (d) in dichloromethane upon one-electron oxidation by oxidative electrolysis (for 5) or chemical oxidation with SbCl$_5$ (for 6-8).
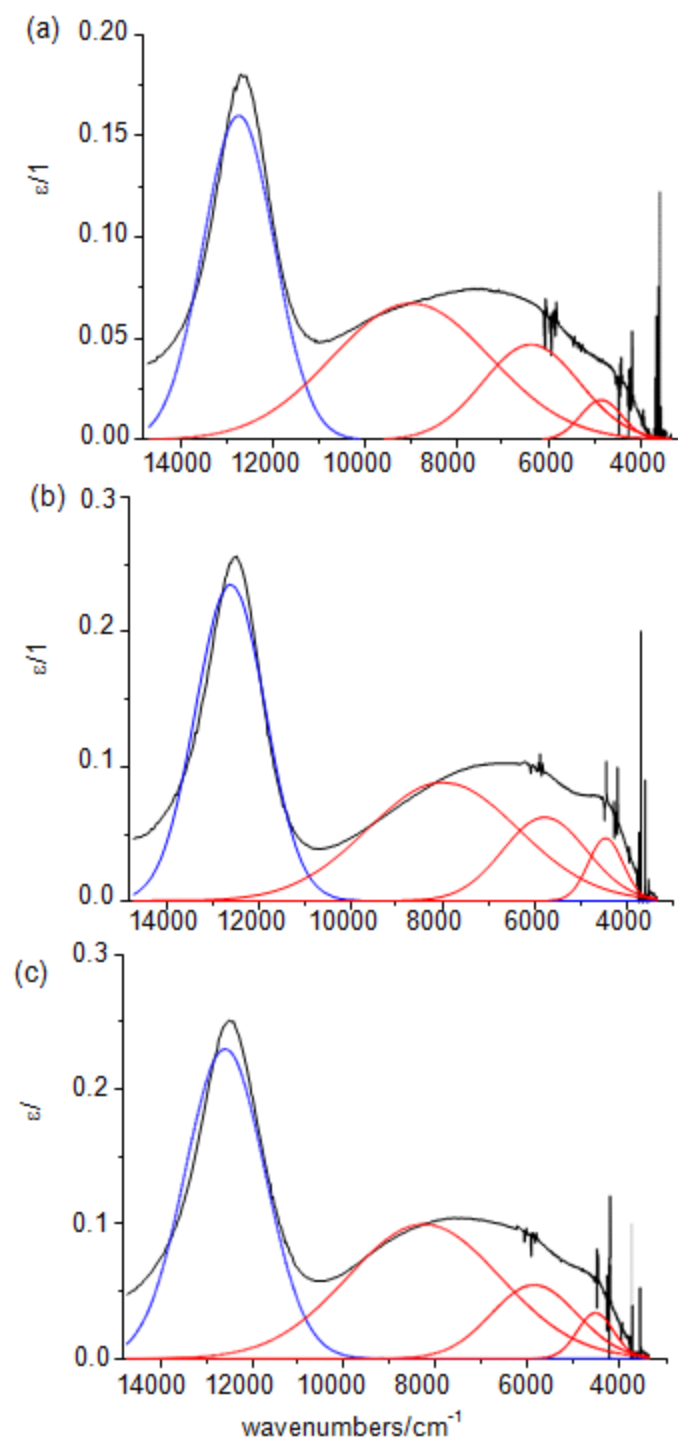
Figure B.12. Decovoluion of the NIR spectra of of [2]•+ (a), [3]•+ (b), and [4]•+ (c). The irregular noises at the low energy side were deleted intentionally before deconvolution.

| gas | *n*-hexane | CH$_2$Cl$_2$ | CH$_3$CN |

[**1**]$^+$ [N-N]$^{•+}$

[**2**]$^+$ [N-Ru-N]$^{•+}$

[**3**]$^+$ [N-Re-N]$^{•+}$

[**4**]$^+$ [N-Tc-N]$^{•}$
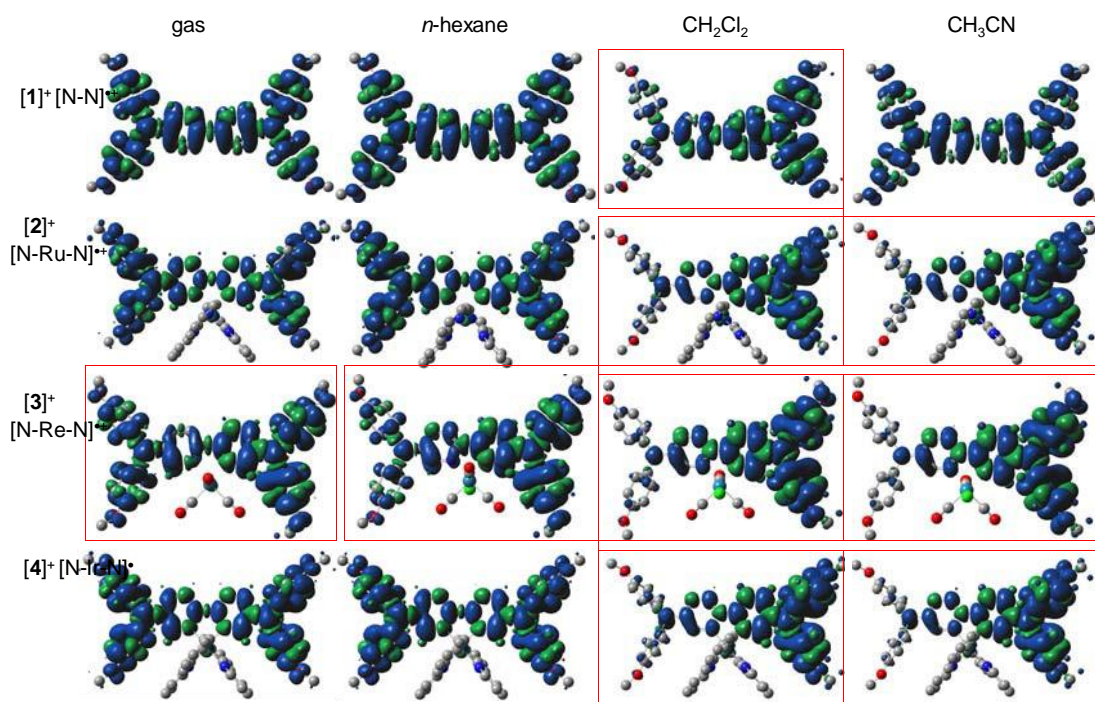
Figure B.13. Spin density plots of [1]$^{•+}$-[4]$^{•+}$ in gas phase and different solvents. Distinct charge localization was observed for [2]$^{•+}$- [4]$^{•+}$ in acetonitrile, as highlighted in red rectangles. H atoms have been omitted for clarity.

Table B.2. Calculated low-energy excitations of one-electron oxidized species of 2-4 at the Level of B3LYP/LanL2DZ/6-31G.

		D_n	E/eV	E/nm	f	Dominant Transitions
[1]•+	CH_2Cl_2	1	0.70	1779.9	0.7529	160B → 161B (1.007)
[N-N]•+		2	1.73	716.0	0.1805	159B → 161B (0.961)
	CH_3CN	1	0.72	1730.2	0.7392	160B → 161B (1.009)
		2	1.74	711.4	0.1701	159B → 161B (0.944)
[2]•+	CH_2Cl_2	1	0.61	2033.6	0.612	249B → 250B (1.010)
[N-Ru-N]•+		2	0.87	1422.2	0.0034	248B → 250B (0.997)
		3	1.06	1171.3	0.0045	246B → 250B (0.998)
		5	1.53	810.1	0.2097	245B → 250B (0.996)
	CH_3CN	1	0.64	1922.6	0.519	249B → 250B (1.005)
		2	0.82	1505.6	0.0032	248B → 250B (0.997)
		3	1.00	1238.9	0.0051	246B → 250B (0.996)
		5	1.59	778.43	0.0569	245B → 250B (0.997)
		6	1.61	771.1	0.1932	244B → 250B (0.995)
[3]•+	CH_2Cl_2	1	0.61	2035.6	0.612	197B → 198B (1.011)
[N-Re-N]•+		2	1.08	1150.5	0.0002	196B → 198B (0.999)
		3	1.16	1069.6	0.004	195B → 198B (0.999)
		4	1.52	814.5	0.0898	194B → 198B (0.931)
		5	1.53	808.5	0.1866	193B → 198B (0.931)
	CH_3CN	1	0.64	1950.6	0.5372	197B → 198B (1.007)
		2	1.20	1031.2	0.0004	196B → 198B (0.999)
		3	1.28	965.8	0.002	195B → 198B (0.993)
		4	1.55	800.1	0.0656	194B → 198B (0.989)
		5	1.58	785.1	0.2045	193B → 198B (0.993)
[4]•+	CH_2Cl_2	1	0.60	2082.1	0.5608	249B → 250B (1.003)
[N-Ir-N]•+		2	0.78	1584.0	0.0012	248B → 250B (0.998)
		3	0.81	1529.7	0.0455	247B → 250B (0.985)
		5	1.37	903.5	0.0003	245B → 250B (0.993)
		6	1.44	858.1	0.0004	244B → 250B (0.997)
		7	1.55	800.0	0.1932	243B → 250B (0.995)
	CH_3CN	1	0.63	1972.2	0.4886	249B → 250B (0.997)
		2	0.80	1545.3	0.002	248B → 250B (0.960)
		3	0.82	1504.3	0.0408	247B → 250B (0.947)
		5	1.39	890.5	0.0003	245B → 250B (0.980)
		6	1.47	841.2	0.0003	244B → 250B (0.936)
		7	1.59	781.4	0.0829	243B → 250B (0.937)
		8	1.60	772.7	0.1635	242B → 250B (0.987)
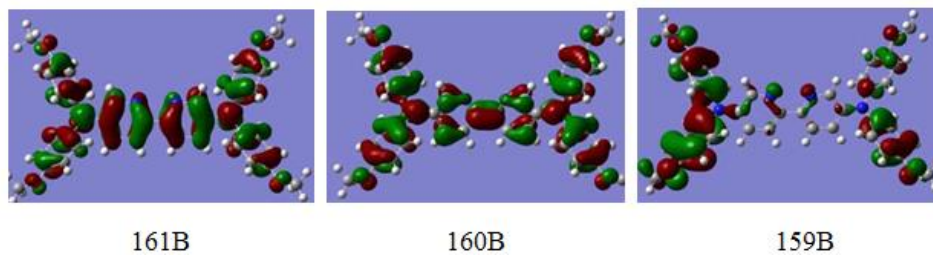
Figure B.14. Frontier orbital diagrams of 1^+ involved in the predicted excitations listed in Table B.2.
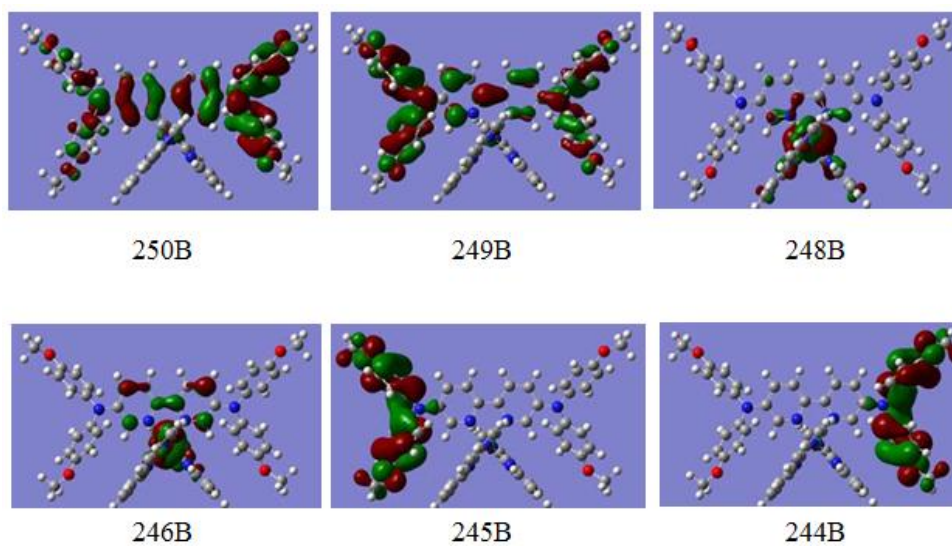
Figure B.15. Frontier orbital diagrams of 2^+ involved in the predicted excitations listed in Table B.2.
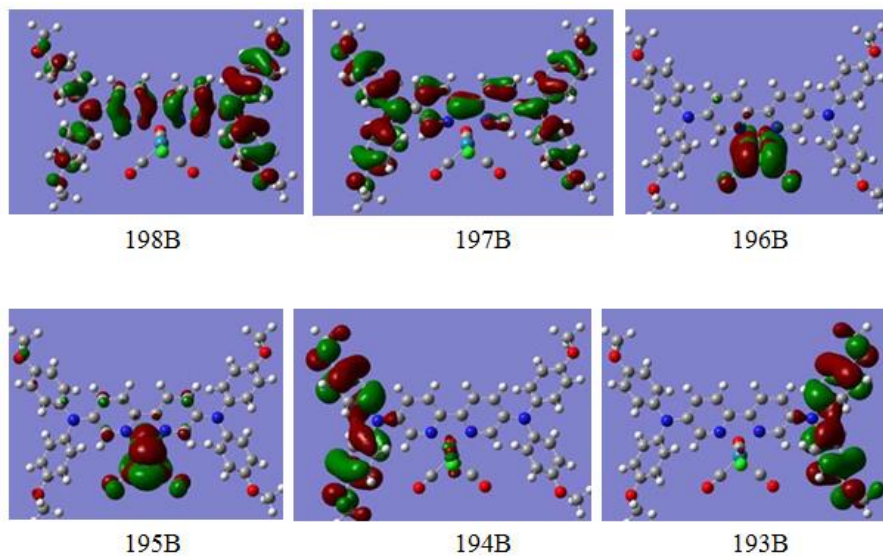
Figure B.16. Frontier orbital diagrams of 3^+ involved in the predicted excitations listed in Table B.2.
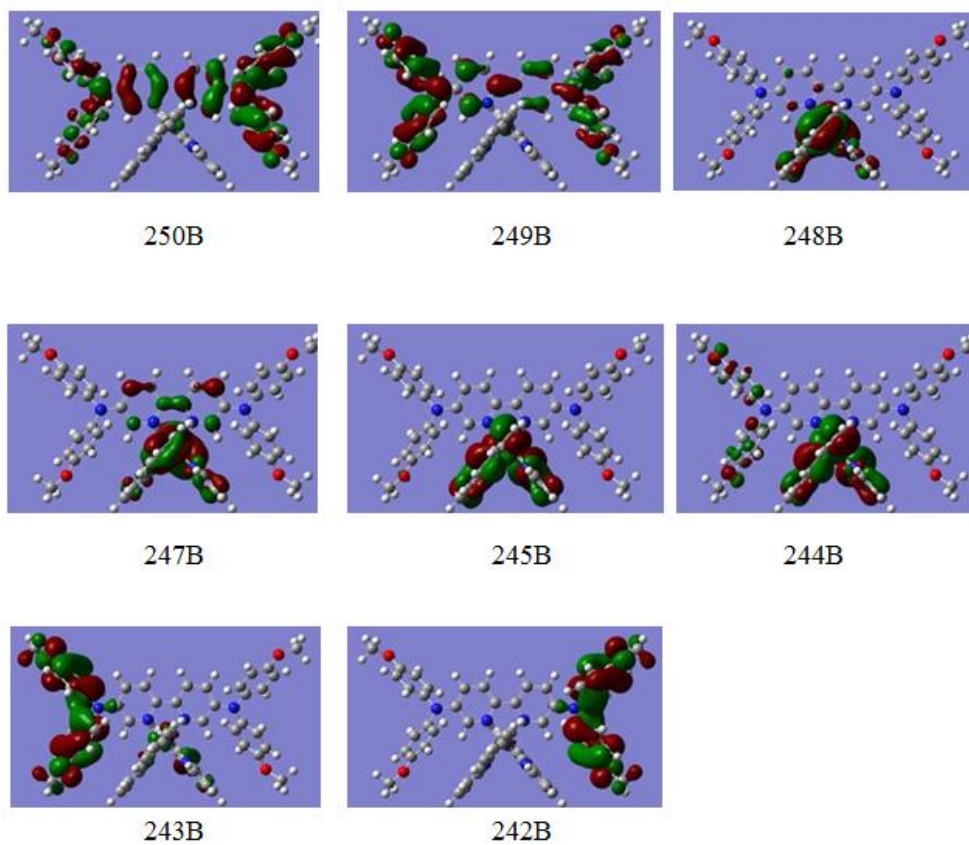
Figure B.17. Frontier orbital diagrams of 3^+ involved in the predicted excitations listed in Table B.2.

Design and Fabrication of Organic Field Effect Transistor Devices. Before fabrication, the photolithography mask (Figure C.1) was designed with computer-aided design (CAD). The critical dimension in our design is 1 μm. Interdigital electrodes with multiple channels were designed to enhance the current signal. Channels of different geometries and dimensions were created to determine the optimal device for a specific project.
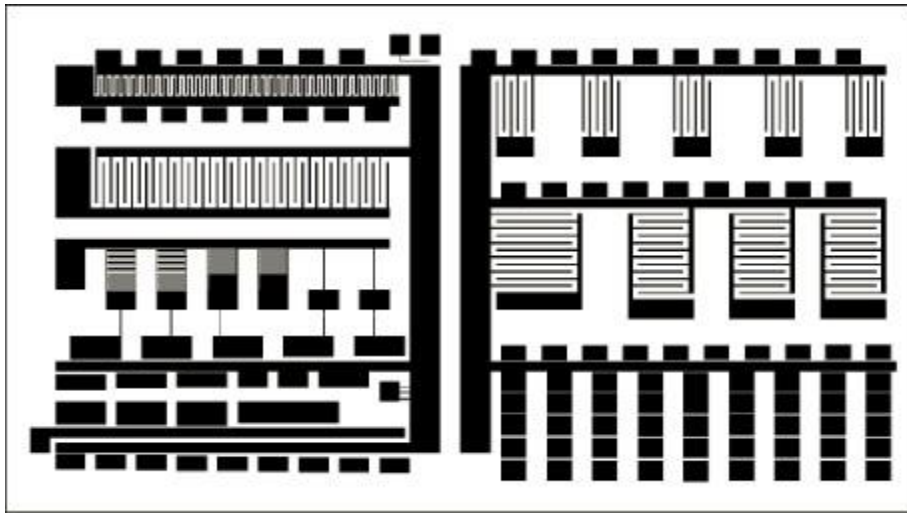
Figure C.1. Primary die for our first generation source-drain electrodes

The procedure to fabricate the device in Figure C.2 is:

(1)   Deposit 4 nm of Ti, 80 nm of Au onto the 4" silicon wafer using an e-beam evaporator.

(2)   Wash with acetone, isopropanol, DI water, and blow dry with nitrogen gas.

(3)   Hard bake on a hotplate of 120 ℃ for 30 minutes

(4)   Spin coat the primer of hexamethyldisiloxane (HMDS) and positive photoresist of AZ 4210 onto the substrate. The spin recipe is 10 s, 500 rpm for the pre-spin and 30s, 3000 rpm for the second spin, which produces a 2.5 μm thick photoresist layer.

(5)   Soft bake at 95 ℃ for 5 minutes.

(6)   Expose with the Karl Suss MA6 Mask Aligner for 3.5 s.

(7)   Develop with the developer (1 AZ400K:3 DI water) for 1 minute.

(8)   Rinse with DI water to remove the extra developer, dry with nitrogen gas and soft bake at 70 ℃ for 1 minute to get rid of moisture residue.

(9)   Etch Au with aqua regia (3 HCl:1 HNO_3:4 H_2O) for 1 minute.

(10) Etch Ti with HF solution for 10 s.

(11) Wash with acetone, isopropanol and water, and blow dry with nitrogen.
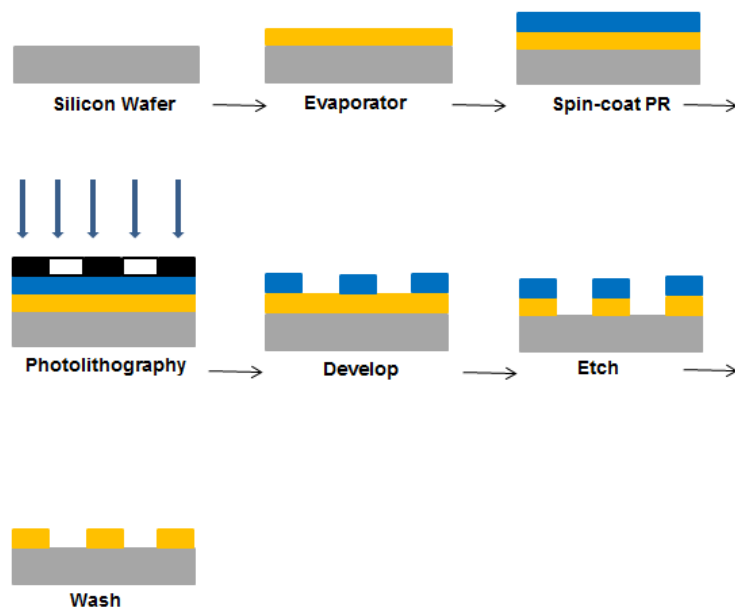
Figure C.2. Fabrication process of our first generation of devices

Before testing the fabricated devices, we tested the probe stage and Keithley source meter with the purchased N-type IRF513 metal-oxide-semiconductor FET (MOSFET) to make sure that the instrument and connection were working correctly.
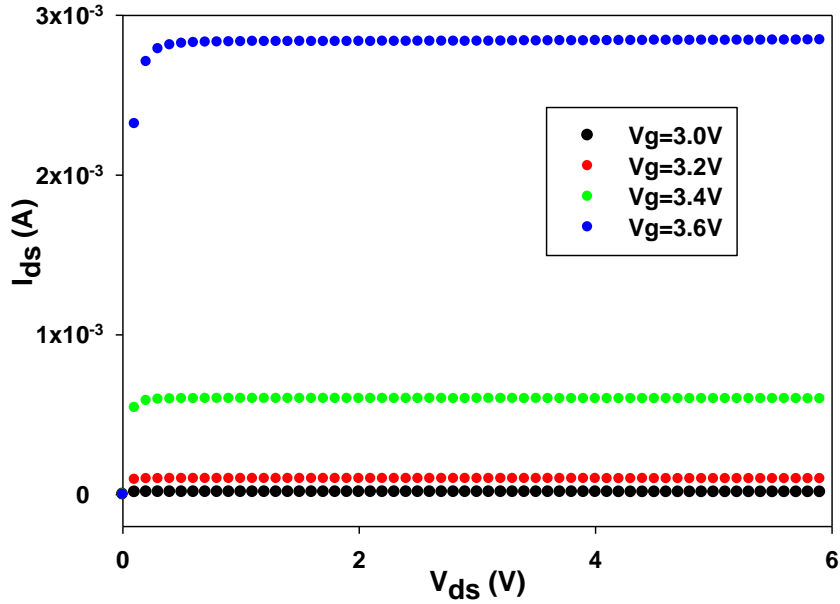
Figure C.3. Output of the standard N-type IRF 513 Power MOSFET.

As shown in Figure C.3, the output was of a typical N-type FET: the drain-source current increases with the gate voltage and saturates when the drain-source voltage gets large enough. The standard tests with IRF 513 MOSFET device indicate that our semiconductor parameter analyzer works correctly. So the next we did was to deposit the semiconductor onto the devices to check the quality of the devices fabricated. Poly (3-hexylthiophene) (P3HT)[146] (1 mg/mL in chloroform) was drop-casted and tested.
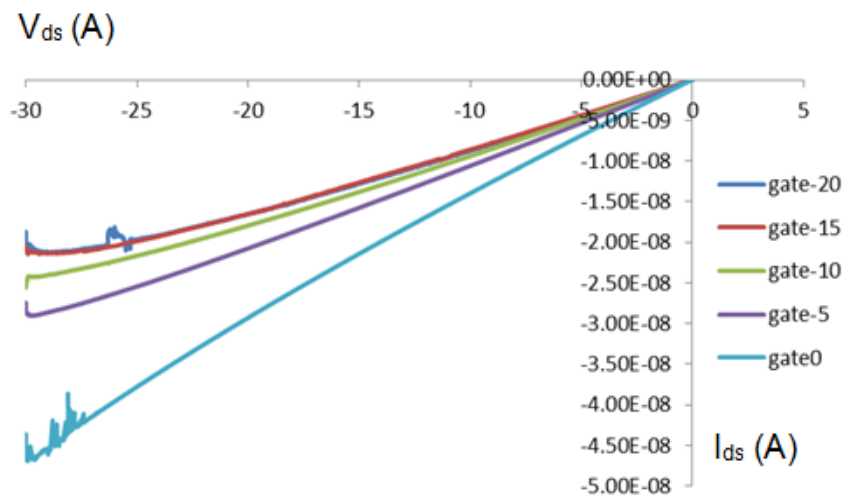
Figure C.4. FET measurement for poly (3-hexylthiophene) test device

The FET measurements on the devices, however, did not show expected gate dependence. The source-drain current decreased with gate, which is not normal. We suspected the gate leakage was severe as we used wet etching in the fabrication, which may produce some pinholes or defects to the SiO_2 insulating layer and makes the gate not correctly working.

Therefore, we switched to lift-off to see if it can improve the fabrication. As we did not have negative photoresists in the cleanroom at that time, a new dark mask was needed to conduct lift-off process with the positive photoresist. Moreover, it was observed that the 1 μm channel was too small to develop and the interdigital devices turned out to work better than the rectangular ones. So we increased the critical dimension of the new mask to 3 μm and implemented more interdigital channels than the first mask. Moreover, experiments showed that the gate was not well connected to the stage, so an additional gate mask was designed to fabricate gate electrodes on the front side of the chips for semiconductors with very low mobility that require maximized current signal.

The pair of masks is as in Figure C.5. The gate mask is to expose the area where the gate electrodes would be made and the source-drain mask is to fabricate the source-drain electrodes. There is a fiducial mark in the center for alignment.
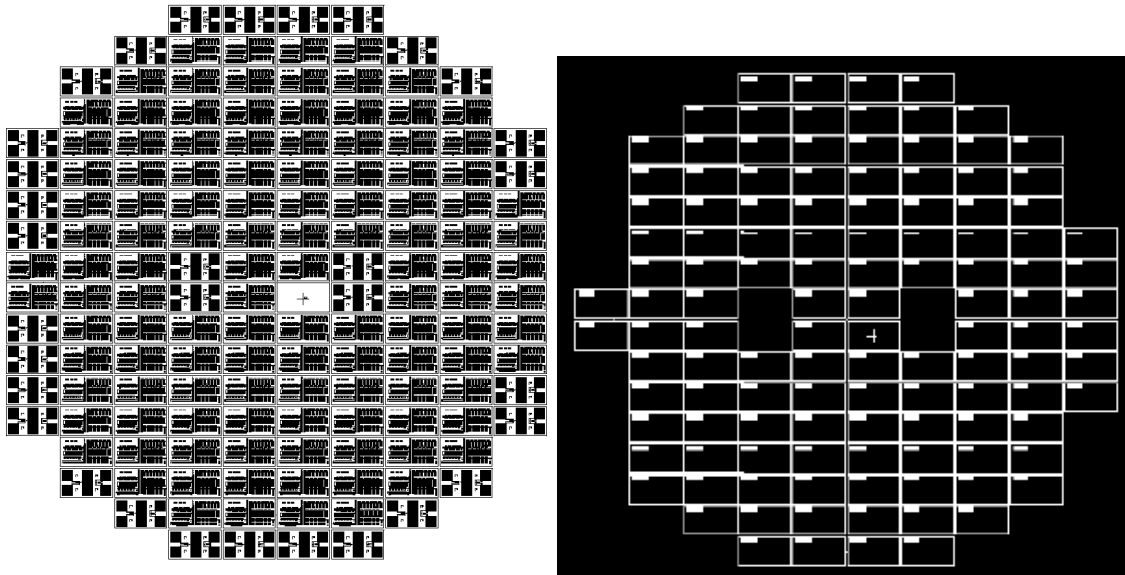
Figure C.5. The source-drain mask (left) and gate mask (right)

As shown in the source-drain mask in Figure C.6, the three big rectangles on the top left are the gate electrodes while the others are source and drain electrodes. The channels are 3-30 μm long and 250-700 μm wide for the rectangular patterns. For the interdigital electrodes, there are 5 bigger electrodes with 12 channels of 50 μm long, 450 μm wide and 7 smaller ones with 5 channels of 50 μm long0, 500 μm wide. For each geometry, more than one electrode was designed to make sure that the measurement can be repeated to get an average data.
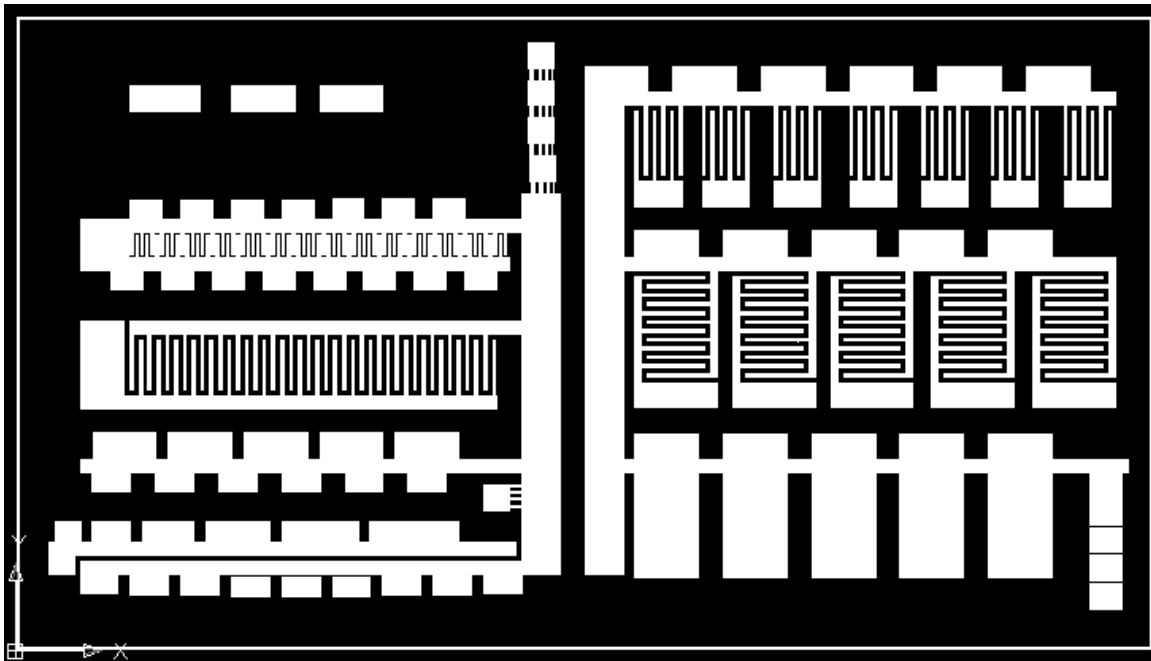
Figure C.6. Primary die for the new source-drain mask.

The new recipe of the fabrication is as follows:

(1)   Wash with acetone, isopropanol, DI water and dry with nitrogen gas.

(2)   Hard bake with the hot plate at 120 ℃ for 30 minutes.

(3)   Spin coat the primer of hexamethyldisiloxane (HMDS) and positive photoresist of Shipley 1827 on the wafer. The spin recipe is 10 s, 500 rpm for the pre-spin and 40s, 6000 rpm for the second spin, which produces a PR layer of 2 μm thick.

(4)   Soft bake at 95 ℃ for 5 minutes.

(5)   Expose with the NFCF Q4000 mask aligner for 30 s.

(6)   Develop with the solution of 351 developer (1developer:3 DI water) for 1 minute.

(7)   Rinse with DI water to remove extra developer and dry with nitrogen.

(8)   Deposit 5 nm of Cr and 80 nm of Au with e-beam evaporator.

(9)   Lift-off with acetone.
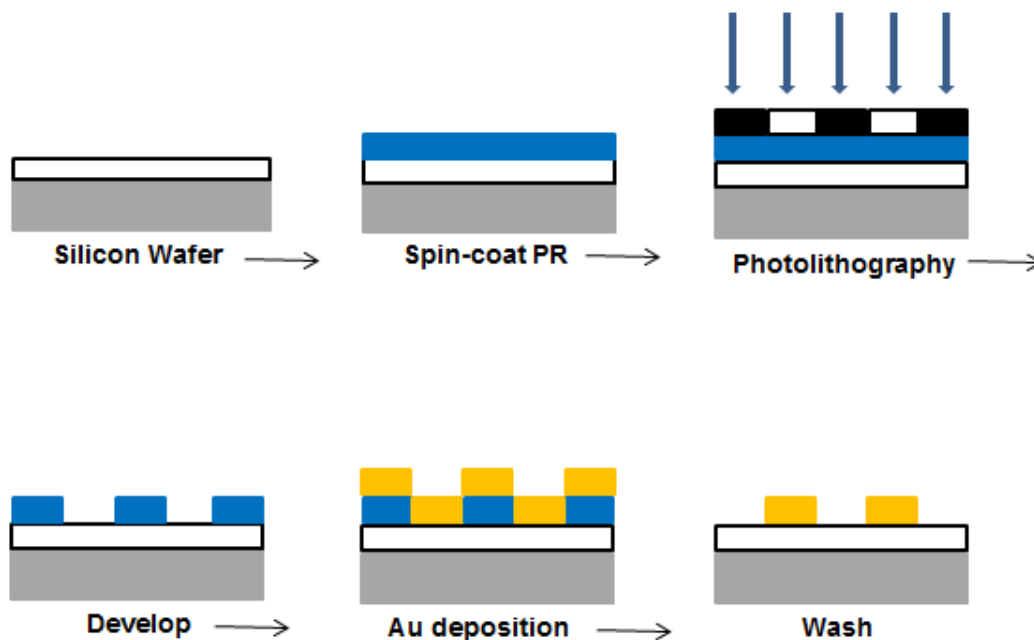
Figure C.7. Fabrication flow of the new devices

The standard tests of the new device were conducted with drop-casted P3HT as before, and the result is shown in Figure C.8.
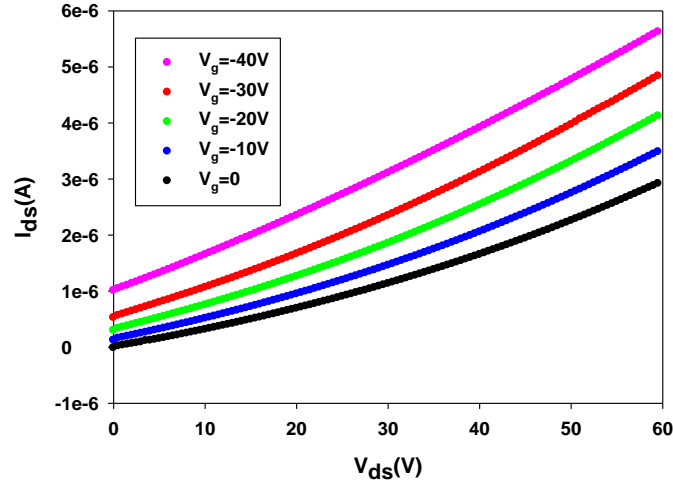
Figure C.8. The FET graph of the device tested with P3HT.

Compared to the previous devices, the new devices produced a larger current signal and improved gate dependence. However, we checked the gate current signal and found that there was still gate leakage in order of magnitude of μA. As the F^- was used to etch the gate contact, and it is quite possible the HF penetrated to the insulating SiO_2 layer even if the device was protected with photoresist before etching. So we decided to avoid using HF in the process, scratch the SiO_2 in the backside, and attach the exposed doped Si to conductive aluminum tape with silver paint to make a good contact with the gate probe (Fig C.9).
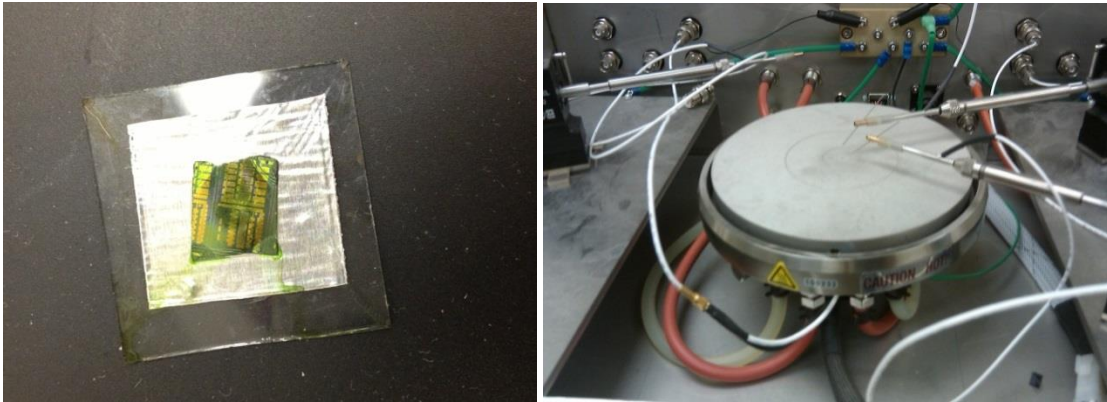
Figure C.9. The device and FET stage
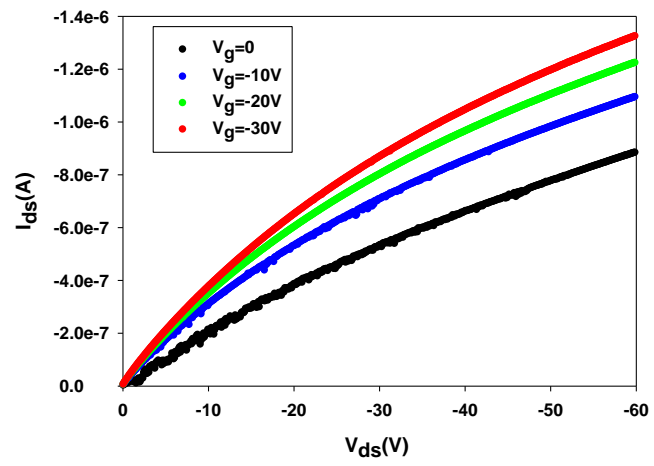
Figure C.10. The output of testing the new generation of device with P3HT: source-drain current with source-drain voltage.

Figure C.10 showed that the devices produced better output: gate dependence was improved, and the trend of saturation showed up. Moreover, the gate leakage was smaller than the device etched with HF. After the test P3HT, we deposited the semiconductor we are interested in onto the devices and tested it. The FET result of the spin-coated Nickel(II) 1,4,8,11,15,18,22,25-octabutoxy-29H,31H-phthalocyanine is shown in Figure C.11. The linear and saturated gate dependence of the source-drain signal was perfect along with the gate leakage noise of nA, quite good device performance.
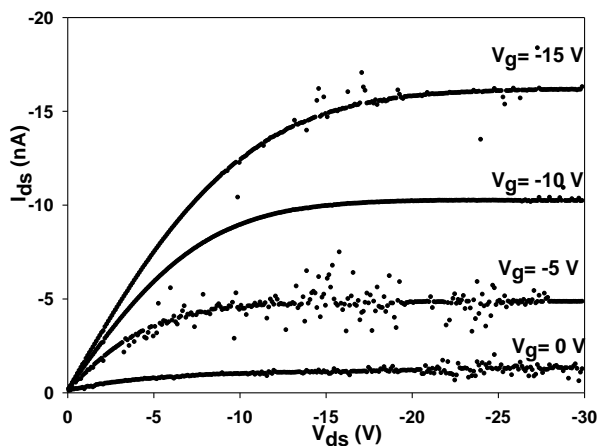
Figure C.11. The output of source-drain (left) and gate (right) signal with the film of Nickel(II) 1,4,8,11,15,18,22,25-octabutoxy-29H,31H-phthalocyanine.

Appendix D   SUPPORTING INFORMATION FOR CHAPTER 4:

CHARACTERIZATION OF THE OCTABUTOXY PHTHALOCYANINE AND

NAPHTHALOCYANINE FILMS

Appendix D.1   XPS MEASUREMENT

Pure NiOBuPc and mixed NiOBuPc/OBuNc film were detected. The elemental analysis was reported to see if the composition of the film is the same as prepared from solution.

Sample 1: Pure NiOBuPc
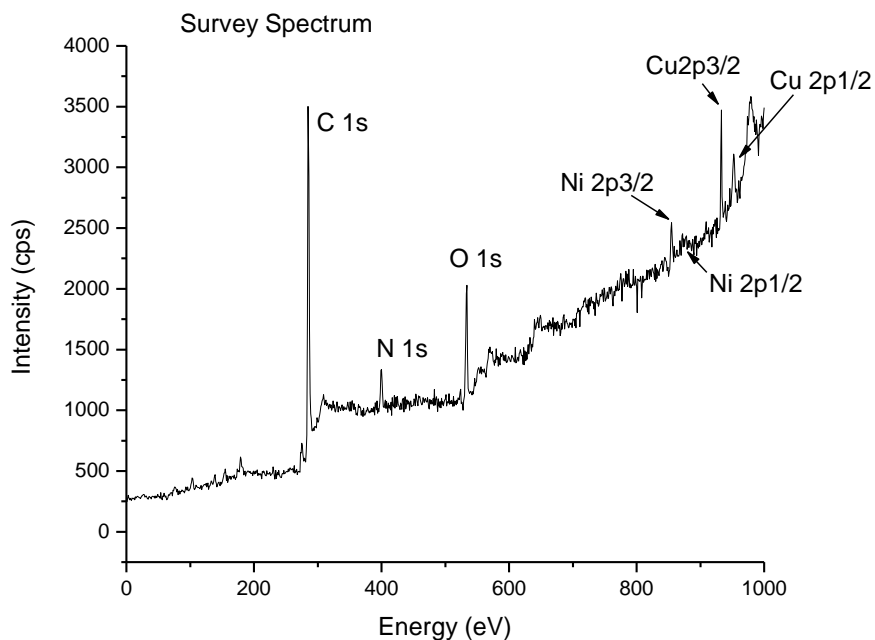
Figure D.1. XPS measurement of the film made with pure NiOBuPc solution. Note: Copper peaks are due to the sample holder

Table D.1. The XPS analysis result of the pure NiOBuPc film.

Element	Int. area	S(sensitivity factor)	I/S	Cx(atom%)	No. of atoms	Theor.Ratio
C	7531	1.00	7531	82.7	64	79
N	1079	1.80	599	6.6	8	9.8
O	2520	2.90	869	9.5	8	9.8
Ni	1535	14.61	105	1.1	1	1.2
Sum:	12665	na	9104	99.9	81	99.8

Sample 2: Mixed NiOBuPc + OBuNc
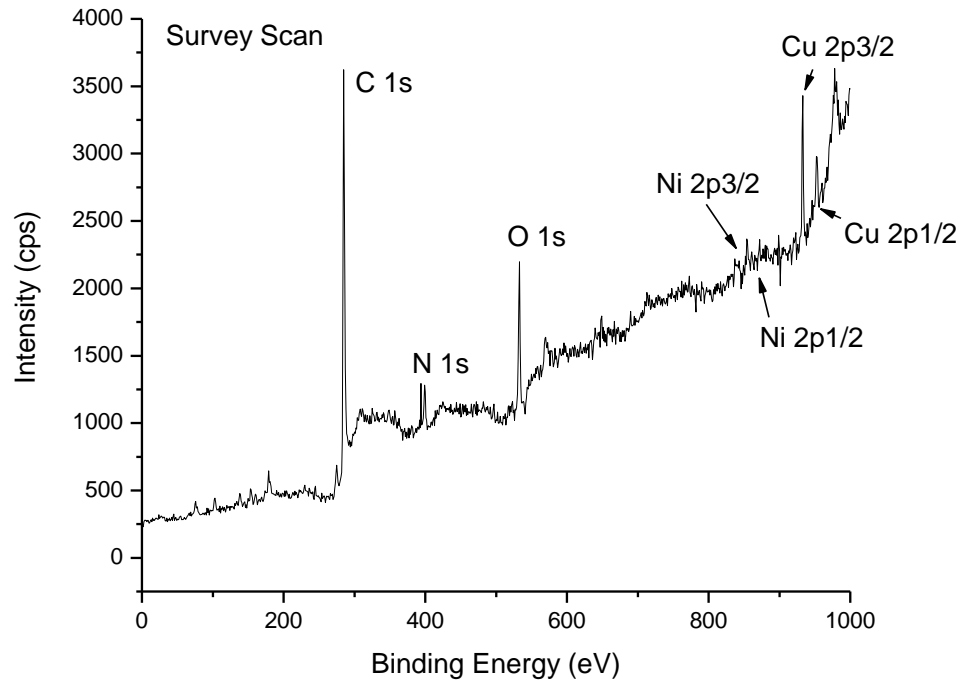
Figure D.2. XPS measurement of the film made with NiOBuPc/OBuNc (50/50) solution.

Table D.2. The XPS analysis result of the 50/50 mixed phthalocyanine films.

Element	Int. area	S(sensitivity factor)	I/S	Cx(atom%)	Number of atoms	Theor.Ratio
C	6947.5	1.00	6947.5	81.8	144	81.4
N	933	1.80	518	6.1	16	9.03
O	2843	2.90	980	11.5	16	9.03
Ni	635	14.61	43.5	0.5	1	0.56
Sum:	11358.5	na	8489	99.9	177	100.02

Appendix D.2   **FET MEASUREMENT**

NiOBuPc are mixed with OBuNc, conductivity of the pure and the mixed films were collected and

mobility was calculated.

Table D.3. The experimental mobility data of the pure and mixed films of NiOBuPc/OBuNc

Film(% of OBuNc)	Std. error	Average	Mobility (10^{-5} cm²/V.s)						
			Device 1	Device 2	Device 3	Device 4	Device 5	Device 6	Device 7
0	0.575	3.89	2.8 6.31 1.95	4.07 7.67 6.38	4.66 2.5 4.74	1.5 2.55 1.55			
2.5	0.089	0.443	0.619 0.079 0.037 0.138	0.367 0.476	0.444 0.974 0.692 0.606				
5	0.128	0.623	0.184 0.206 0.682 0.391	1.52 1.1 0.97 0.634	0.779 0.131 0.252				
10	0.015	0.063	0.107	0.042 0.077	0.027				
25	0.072	0.178	0.449 0.045	0.013	0.034 0.484	0.030	0.191		
50	0.123	0.539	0.030	0.030	0.822 0.543	0.99 0.928 0.436 0.535			
75	0.198	0.778	0.195 0.164 0.1	0.181 0.166	0.056	1.91 1.34 1.11	1.93 1.24 0.741 0.879		
82.5	0.150	1.359	1.91 1.72 1.34 1.11	1.93 1.24 0.741 0.879					
90	0.305	3.576	4.03 2.47 2.46	3.54 5.36 4.87 4.81	4.85 3.29 3.05 3.13	6.07 5.2 6.19	2.5 2.42 2.05		
95	0.403	3.463	4.77 3.85 3.86 3.39	5.61 5.32	0.377 0.086	6.91 6.05 5.79	3.2 2.36 1.47	4.04 3.53 1.99	3.66 3.53 2.09 0.846
100	0.586	4.212	0.71	0.874 0.912	7.87 6.64 6.46	7.29 6.23 5.21 5.32	1.79 2.54 1.78	3.09 2.88 2.42 2.52	8.46 7.04

Note: the different figures within the same device represent the mobility with the same film but different area of a same device.

Before using the mixed of NiOBuPc/OBuNc, we also tried mixing NiOBuPc with terthiophene or ZnOBuPc. But neither of them worked. It turned out that the pure terthiophene and ZnOBuPc do not show FET behavior, and introducing them into the NiOBuPc could not produce a mobility graph of a range of 0%-100%. The source-drain current decreased to a noise level when more than 50% of terthiophene or 3% of ZnOBuPc was introduced. Moreover, in the simulation model, we assume both the transport site and trap site are able to transport charges. So the terthiophene and ZnOBuPc are not ideal candidates for this project.

Table D.4. The experiment mobility data of the pure and mixed films of NiOBuPc/terthiophene

Film(%of terthiophene)	Std. error	Average	Mobility (10^{-5} cm²/V.s)		
			Device 1	Device 2	Device 3
0	0.39	1.60	0.959 0.606	1.94 3.65 1.53 2.37	1.12 0.638
25	0.20	0.76	0.951 1.34 0.493 0.701	0.355	
50	0.21	0.50	0.808	0.145 0.228 0.836	
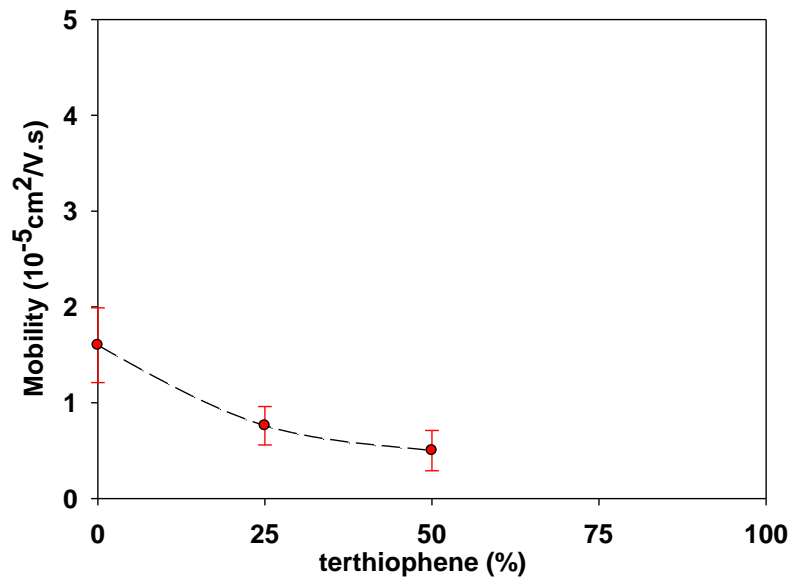
Figure D.3. Mobility with percentage of terthiophene in the NiOBuPc/terthiophene mixed films.
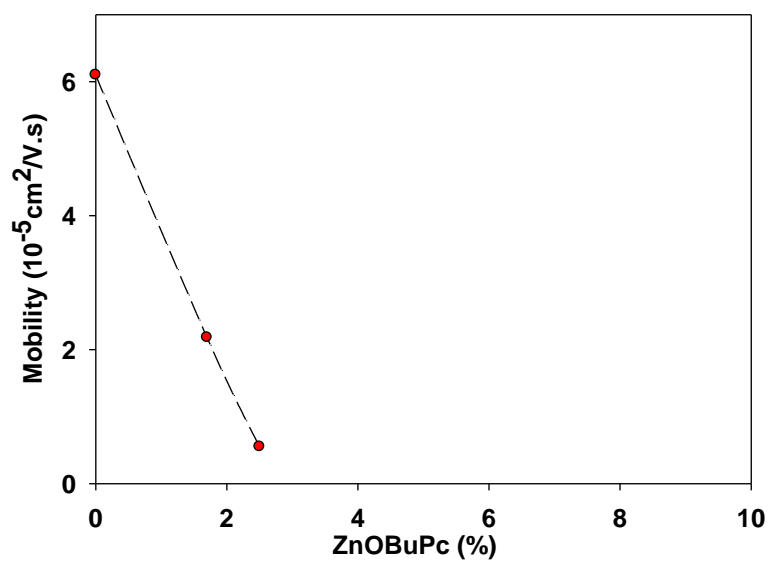
Figure D.4. Mobility with percentage of ZnOBuPc in the NiOBuPc/ZnOBuPc mixed films.

Tapping mode AFM images were obtained. Morphology and surface roughness of the different films were examined.
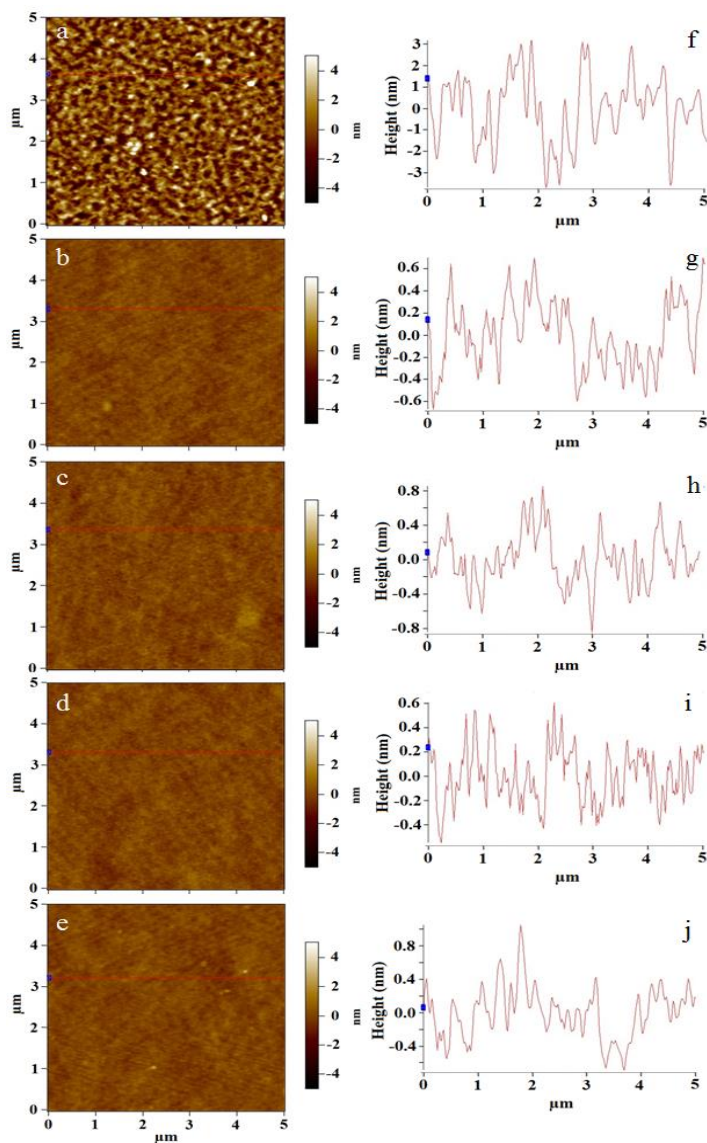
Figure D.5. AFM height images of samples containing OBuNc of a) 0%, b) 25%, c) 50%, d) 75%, and e) 100% and their corresponding section line (f-j).
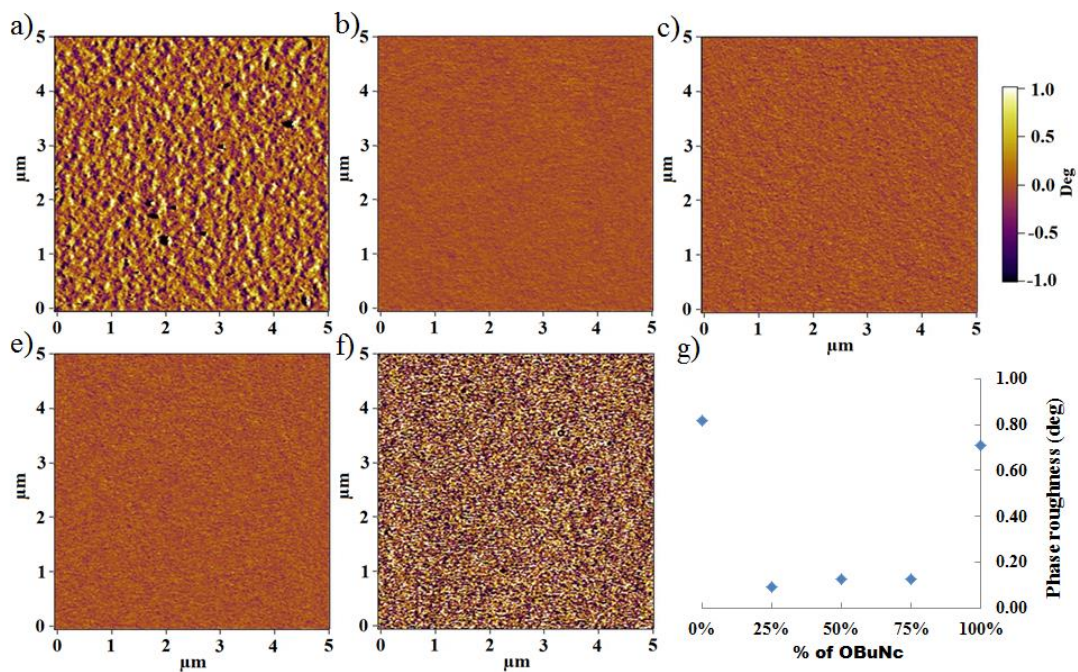
Figure D.6. AFM phase images of samples containing OBuNc of a) 0%, b) 25%, c) 50%, d) 75%, and e) 100%. Phase images were recorded simultaneously with height images in Figure D.37. Phase roughness is below 1˚, indicating composition homogeneity of all five films.

Appendix D.4 **MONTE CARLO SIMULATION**

The model consists of a coarse grained lattice of sites, each 1 nm^3 in size. A site represents a single, conducting organic molecule, such as phthalocyanine. The dimensions of the lattice can vary. In this work, we have simulated thin films with an area of 1024*256 nm^2 and thickness of 3 nm. Charge transport in OFETs occurs mainly within the first few layers, near the dielectric-semiconductor interface, so the difference in film thickness is not expected to be significant.

The molecular sites can be empty or occupied by a charge carrier, such as a hole. When a hole occupies a site, this corresponds to an electron being removed from the molecule's highest occupied molecular orbital (HOMO). Note that holes are more likely to move to molecules with higher HOMO energy. This is rationalized by imagining the electron that has to move to a lower energy when the hole moves to a higher energy.

In a pure system, all sites are assigned an equal HOMO energy. Traps (for holes) are introduced into the system by shifting the HOMO energy of a site up by some value, for example, 0.01 - 0.1 eV. Likewise, barriers (for holes) are introduced into the system by shifting the HOMO down by some value. Additionally, very large barriers, termed defects, can be added. Defects represent dust and unreactive chemical impurities. In the model, carriers cannot transport to defect sites. The assignment of trap and barrier energies is performed explicitly, unlike the traditional Gaussian Disorder Model (GDM), in which site energies are assumed to take on a Gaussian distribution. In this work, traps and barriers were placed homogenously at randomly chosen sites.

Site energies also explicitly incorporate the Coulomb interactions between charge carriers in the film. While most theoretical models do not include the detailed effects of Coulomb interactions between carriers due to computational cost, they prove to be very influential in the dynamics on mechanism of charge transport in the film. The Coulomb interaction is long ranged

and the static dielectric constant is small (~2-3.5) in the organic materials used in thin films. Similarly, the interactions are strong due to the localization of charges onto the molecular sites and the close proximity of charges.

On the left side of the lattice is a source electrode, which injects holes into the system at a constant probability (90%). Holes are injected into a site directly adjacent to the electrode, should it be unoccupied. On the right side of the lattice is a drain electrode. Holes which are adjacent to the drain can attempt to leave the lattice with a constant probability of success (90%). The choice of a constant probability for the injection and removal of charge carriers represents an assumption that the energetic barriers at the electrode-semiconductor interfaces are constant and small, as we have tested previously.

A potential is applied between the source and drain electrode (V_{DS}). This potential is assumed to be linear, and modulates the HOMO energy at each site. The model does not explicitly contain a gate electrode. However, the potential of the gate electrode can be treated by applying a field along the z-direction, which has the effect of moving charges into layers near the semiconductor-dielectric interface. Only 3 layers were used in the simulation, therefore no field in the z-direction was applied. Ample evidence suggests only the first 1-3 layers are involved in charge transport. The gate electrode also determines how many charge carriers are in the system. A constant charge carrier concentration of 1% (7864 carriers) was used here, matching on experimental gate voltage of 15.7 V through the 300 nm SiO_2 dielectric.

Initially, before the simulation starts, these charges are placed randomly. Randomly placed charges can be thought of as the result of the gate electrode oxidizing molecular sites or as residual charges present in the film. Although equilibration times are longer, identical long term behavior

is achieved by starting the simulation with no charges and allowing them all to be injected by the source electrode.

A typical simulation can be described as follows. Charges are first randomly placed. The movement of charges is assumed to occur via thermally activated hopping, which can be described using Marcus Hush theory. Hopping occurs because electronic states are localized on molecular sites in organic semiconductors, a result of the weak electronic interactions and disorder present in the system. At each step, charges attempt to hop to a randomly chosen adjacent site. The energy change, which includes the source-drain potential VDS, the trap energy, and the Coulomb interaction, is used in the Metropolis criterion to determine the probability of hopping. The criterion is modified by a coupling constant that enforces a small probability to remain on a site, even when the energy change is negative. A value of 33% is used. To maintain detailed balance, this coupling constant also multiplies the Boltzmann factor. As a result, moves to lower energy are accepted 1/3 of the time. At the end of each step, the source electrode attempts to inject new carriers.

A dynamic interpretation of the states produced is accomplished by associating a timescale with the moves, regardless of if they are accepted or rejected. For example, carriers will spend more time on states of low energy, like trap states, by nature of a small probability to move to higher energy states. The timescale chosen for a fundamental move is ~ 1 ps, and is consistent with quantum chemistry calculations and fast, efficient charge transfer. The charge transfer rate and the coupling constant only affect the magnitude of electrical currents calculated by our code and not the trends observed. The current is calculated by monitoring how many carriers exit the drain electrode. The process is repeated at different V_{DS} to construct a current-voltage curve.

Simulations of thin film OFETs with dimensions of 1024x256x3 nm^3 with 1% charge

carriers (7864 max carriers) were performed. Current was calculated for 0.5 μs and results

averaged over three simulation replicas. Only hole transport was considered. Coulomb

interactions were treated using point charges, delocalized Gaussian charges, and non-interacting

charges. For Gaussian charges, the standard deviation chosen was 1 nm, 1.25 nm, and 1.5 nm. IV

curves were calculated for systems with a mixture of 75% semiconductor and 25% shallow traps

(-0.05 eV), 25% high barriers (0.50 eV), and 25% defects. V_{DS} was varied between 0 and -150 V.

Additionally, the slope of the IV curve in the saturation region (differential conductance) was

measured as a function of trap/barrier energy (-1.0 to 1.0 eV) by calculating a few IV points in the

saturation region (120, 140, 150 V).
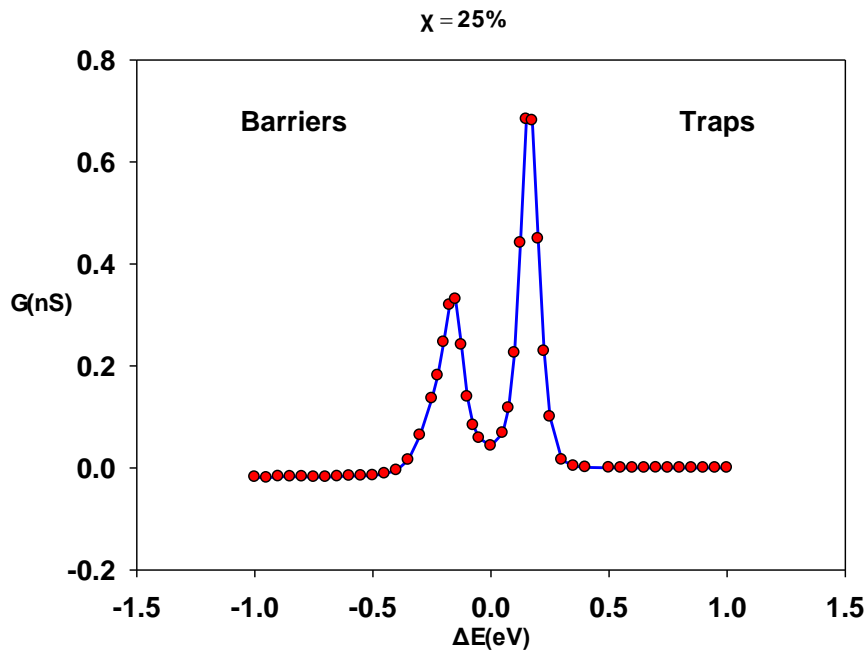
Figure D.7. The differential conductance in the saturation region as a function of trap or barrier energy for a system

with 25% traps or barriers

Figure D.7 shows the differential conductance in the saturation region as a function of trap

or barrier energy for a system with 25% traps or barriers. Differential conductance indicates how

128

the conductance is changing as the voltage increases and is simply the slope of the IV curve. When the trap energy is zero (pure system), the differential conductance is small and positive (0.04 nS). Ideal saturation would mean that the conductance does not change with voltage. This system is very near, but not completely saturated.

Interestingly, as the trap or barrier energy increases, the differential conductance reaches a maximum at +/- 0.16 eV. The peak for traps (0.68 nS) is nearly twice the height as the peak for barriers (0.32 nS). A larger differential conductance indicates a perturbed onset of ideal saturation. Therefore, this suggests that traps are a larger hindrance to charge transport than barriers, likely because it is thermodynamically favorable to fall into a trap. The peak location is near the energy associated with the potential difference between the source and drain electrodes at saturation for an adjacent site hop (e * 150 V / 1024 nm * 1 nm ~ 0.15 eV). It is this energetic driving force, along with the Columbic interactions between carriers, which drives carriers out of traps or into / past barriers. The presence of a peak indicates that traps / barriers are (at first) an increasing hindrance to ideal saturation.

As traps deepen beyond -0.16 eV, the differential conductance begins to fall and remains zero for traps deeper than -0.4 eV. Although the differential conductance calculated is zero beyond -0.4 eV, a saturated IV curve does not exist. When traps are this deep, there is no current, because nearly all carriers become trapped. There are many more trap sites than carriers. The simulation assumptions, such as constant carrier concentration, may be invalid in this region.

Barriers behave differently as they become larger than 0.16 eV. The differential conductance falls off, and becomes negative beyond 0.4 eV. At this energy, the barriers become insurmountable hills or defects.
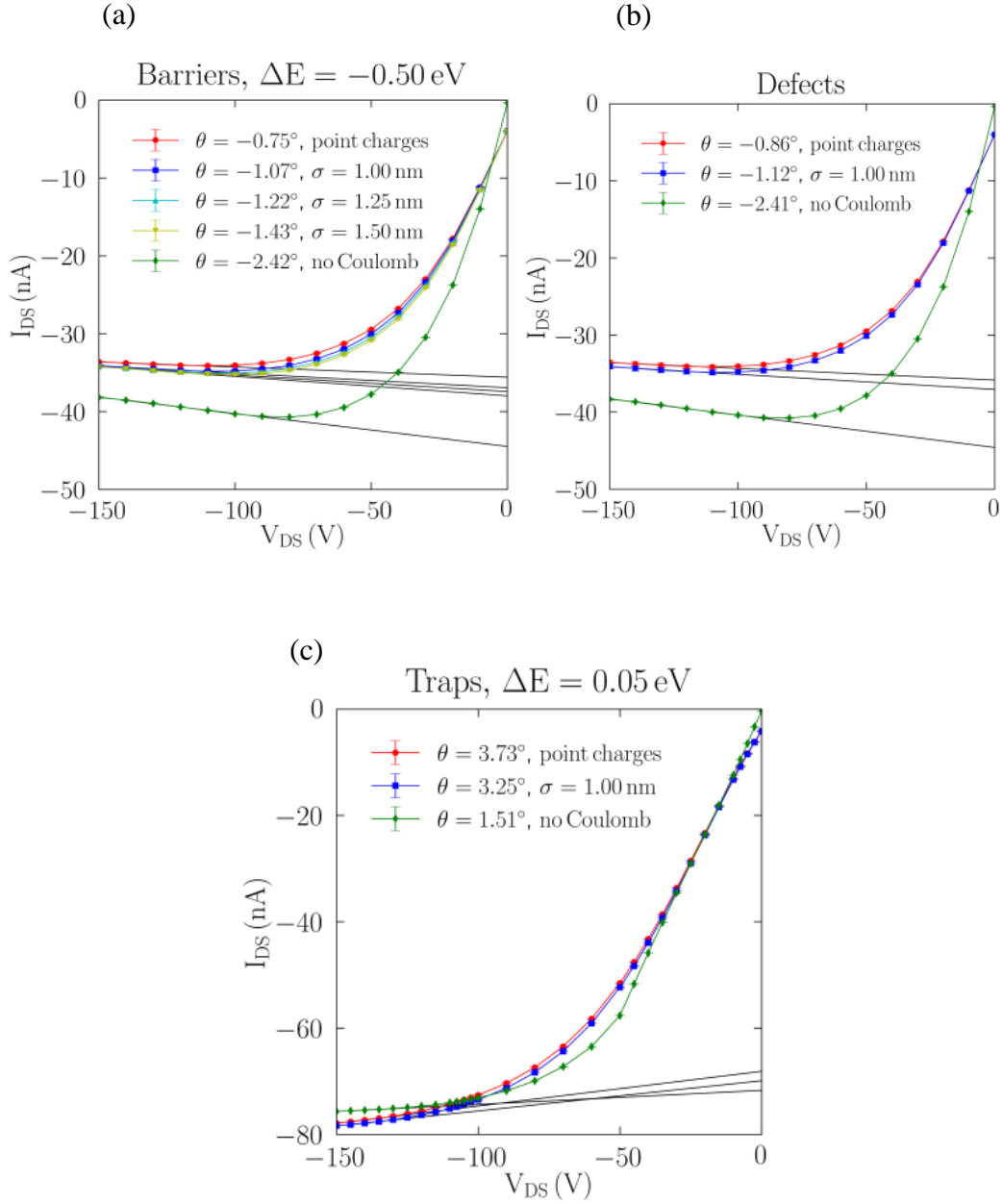
Figure D.8. The simulated I-V curves for systems with 25% barriers (a), defects (b) and traps (c).

Figure D.8 (a) shows IV curves for systems with 25% high barriers (+0.50 eV). Curves are shown for Coulomb interactions treated as point charges, delocalized Gaussian charges (sigma = 1.0, 1.25, 1.50 nm), and non-interacting charges. All curves exhibit negative differential conductance in the saturation region (-0.013, -0.019, -0.021, -0.025, -0.042 nS). As charge

interactions become weaker (higher sigma), the negative differential conductance becomes more negative and thus the system more resistive. A mechanism for defect induced negative differential conductance was proposed by Hanwell. Non-interacting carriers become blocked / immobilized by the presence of defects, leading to a negative differential conductance. However, when Coulomb interactions are present, other carriers are funneled around the defects by the Coulomb interaction with blocked carriers. This leads to a smaller differential conductance and faster onset of ideal saturation.

Figure D.8 (b) shows IV curves for systems with 25% defects. Again, curves are shown for the varying treatments of Coulomb interactions. Curves show a negative differential conductance in the saturation region (-0.015, -0.020, -0.042 nS) of similar magnitude to the corresponding curves for high barriers (-0.013, -0.021, -0.042 nS). This indicates that the barriers are behaving like defects.

Figure D.8 (c) (traps) shows IV curves for systems with 25% shallow traps (-0.05 eV). Curves are shown for Coulomb interactions treated as point charges, delocalized Gaussian charges with sigma = 1.00 nm, and non-interacting charges. All three exhibit positive differential conductance (0.065, 0.057, 0.026 nS), in agreement with Figure D.39. Non-interacting charges show the smallest differential conductance in the saturation region and reach near ideal saturation at lower voltages (~-100 V) than interacting charges (> 150 V). However, non-interacting charges show lower current (-75 nA) in the saturation region compared to interacting charges (-80 nA). This is a result of Coulomb interactions removing carriers from trap sites.
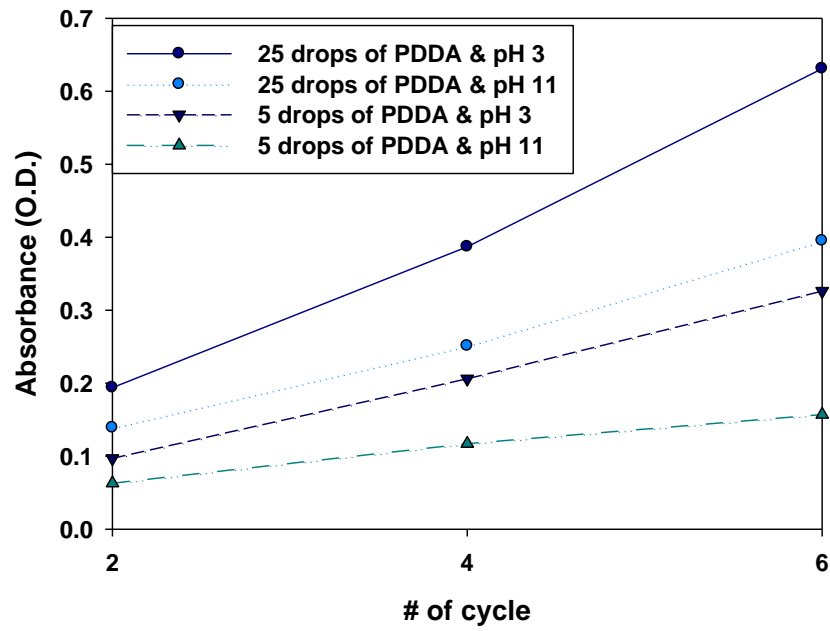
Figure E.1. The spectra data of CuPs solutions of different pH (pH 3, pH 11) and varying amounts of PDDA in the water bath for absorption at 328 nm.

(a)

(b)

(c)

(d)
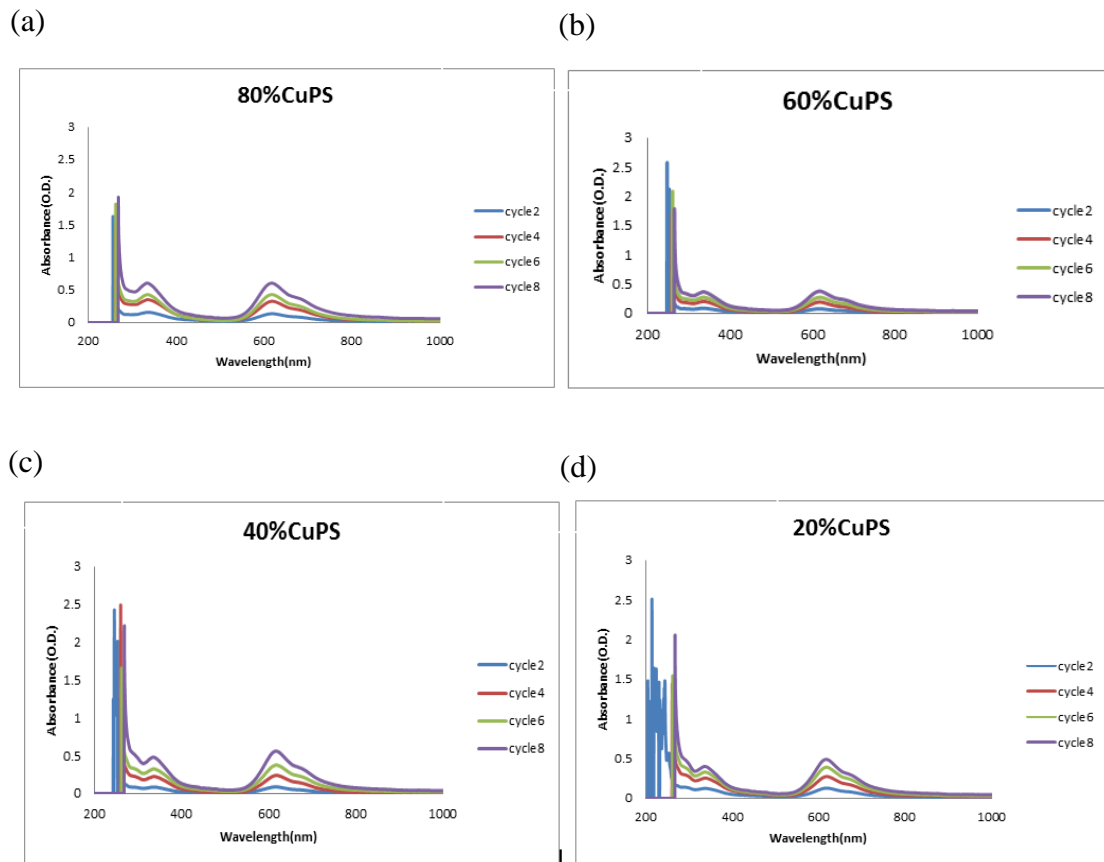
Figure E.2.UV-vis spectra of the mixed films with 80% (a), 60% (b), 40% (c) and 20% (d) of CuPs.

BIBLIOGRAPHY

1.   H. Shirakawa, E. J. Louis, A. G. Macdiarmid, C. K. Chiang and A. J. Heeger, *J Chem Soc Chem Comm*, 1977, 578-580.

2.   A. P. Kulkarni, C. J. Tonzola, A. Babel and S. A. Jenekhe, *Chem Mater*, 2004, 16, 4556-4573.

3.   J. Smith, W. M. Zhang, R. Sougrat, K. Zhao, R. P. Li, D. K. Cha, A. Amassian, M. Heeney, I. McCulloch and T. D. Anthopoulos, *Adv Mater*, 2012, 24, 2441-2446.

4.   B. C. Thompson and J. M. J. Frechet, *Angew Chem Int Edit*, 2008, 47, 58-77.

5.   G. Li, V. Shrotriya, J. S. Huang, Y. Yao, T. Moriarty, K. Emery and Y. Yang, *Nat Mater*, 2005, 4, 864-868.

6.   Z. Bao, A. Dodabalapur and A. J. Lovinger, *Appl Phys Lett*, 1996, 69, 4108-4110.

7.   B. A. Jones, A. Facchetti, M. R. Wasielewski and T. J. Marks, *J Am Chem Soc*, 2007, 129, 15259-15278.

8.   http://www.lg.com/us/tv-audio-video/premium-entertainment/oled-tv-features.jsp.

9.   http://www.agfa.com/sp/global/en/binaries/Orgacon%20OPV%20Flyer%20V2-07032013%20WEB_tcm611-97160.pdf.

10.   http://commons.wikimedia.org/wiki/File:Best_Research-Cell_Efficiencies.png.

11.   O. D. Jurchescu, J. Baas and T. T. M. Palstra, *Appl Phys Lett*, 2004, 84, 3061-3063.

12.   H. Bassler, *Phys Status Solidi B*, 1993, 175, 15-56.

13.   Marcus, R.A (1956). "On the Theory of Oxidation-Reduction Reactions Involving Electron Transfer. I". *J. Chem. Phys*. 24 (5): 966. Bibcode:1956JChPh..24..966M. doi:10.1063/1.1742723.

14.   S. L. M. van Mensfoort, S. I. E. Vulto, R. A. J. Janssen and R. Coehoorn, *Phys Rev B*, 2008, 78, 085207.

15.   V. Ambegaokar, B. I. Halperin and J. S. Langer, *Phys Rev B-Solid St*, 1971, 4, 2612-2620.

16.   V. Podzorov, E. Menard, A. Borissov, V. Kiryukhin, J. A. Rogers and M. E. Gershenson, *Phys Rev Lett*, 2004, 93, 086602.

17.   M. Chikamatsu, A. Itakura, Y. Yoshida, R. Azumi, K. Kikuchi and K. Yase, *Journal of Photochemistry and Photobiology A: Chemistry*, 2006, 182, 245-249.

18.   N. KARL, Mol Cryst Liq Cryst, 1989, 171, 157-177.

19.   L. B. Roberson, J. Kowalik, L. M. Tolbert, C. Kloc, R. Zeis, X. L. Chi, R. Fleming and C. Wilkins, *J Am Chem Soc*, 2005, 127, 3069-3075.

20.   R. Bonnett, *Chem Soc Rev*, 1995, 24, 19-33.

21.   J. J. Cid, J. H. Yum, S. R. Jang, M. K. Nazeeruddin, E. M. Ferrero, E. Palomares, J. Ko, M. Gratzel and T. Torres, *Angew Chem Int Edit*, 2007, 46, 8358-8362.

22.   M. O. Senge, M. Fazekas, E. G. A. Notaras, W. J. Blau, M. Zawadzka, O. B. Locos and E. M. N. Mhuircheartaigh, *Adv Mater*, 2007, 19, 2737-2774.

23.   G. de la Torre, C. G. Claessens and T. Torres, *Chem Commun*, 2007, 2000-2015.

24.   M. Bouvet, *Anal Bioanal Chem*, 2006, 384, 366-373.

25.   Y. H. Kim, C. Sachse, M. L. Machala, C. May, L. Muller-Meskamp and K. Leo, *Adv Funct Mater*, 2011, 21, 1076-1081.

26.   M. Mayukh, C. M. Sema, J. M. Roberts and D. V. McGrath, *J Org Chem*, 2010, 75, 7893-7896.

27.   S. Chen and J. Ma, *J Comput Chem*, 2009, 30, 1959-1972.

28.   A. M. Zhong, Y. X. Zhang and Y. Z. Bian, *J Mol Graph Model*, 2010, 29, 470-480.

29.   N. Kobayashi, H. Ogata, N. Nonaka and E. A. Luk'yanets, *Chem-Eur J*, 2003, 9, 5123-5134.

30.   R. A. Marcus, *J Chem Phys*, 1956, 24, 979-989.

31.   D. A. da Silva Filho, V. Coropceanu, N. E. Gruhn, P. H. de Oliveira Neto and J. L. Bredas, *Chem Commun (Camb)*, 2013, 49, 6069-6071.

32.   http://www.gaussian.com/.

33.   K. Kim and K. D. Jordan, *J Phys Chem-Us*, 1994, 98, 10089-10094.

34.   P. J. Hay and W. R. Wadt, *The Journal of Chemical Physics*, 1985, 82, 270-283.

35.   http://avogadro.openmolecules.net/wiki/Main_Page.

36.   N. M. O'Boyle, A. L. Tenderholt and K. M. Langner, *J Comput Chem*, 2008, 29, 839-845.

37.   D. Arican, M. Arici, A. L. Ugur, A. Erdogmus and A. Koca, *Electrochim Acta*, 2013, 106, 541-555.

38.   A. V. Soldatova, J. Kim, X. H. Peng, A. Rosa, G. Ricciardi, M. E. Kenney and M. A. J. Rodgers, *Inorg Chem*, 2007, 46, 2080-2093.

39.   H. Benten, N. Kudo, H. Ohkita and S. Ito, *Thin Solid Films*, 2009, 517, 2016-2022.

40.   D. M. D'Alessandro and F. R. Keene, *Chem Rev*, 2006, 106, 2270-2298.

41.   W. Kaim and G. K. Lahiri, *Angew Chem Int Edit*, 2007, 46, 1778-1796.

42.   P. Aguirre-Etcheverry and D. O'Hare, *Chem Rev*, 2010, 110, 4839-4864.

43.   M. H. Chisholm and B. J. Lear, *Chem Soc Rev*, 2011, 40, 5254-5265.

44.   V. N. Nemykin, G. T. Rohde, C. D. Barrett, R. G. Hadt, C. Bizzarri, P. Galloni, B. Floris, I. Nowik, R. H. Herber, A. G. Marrani, R. Zanoni and N. M. Loim, *J Am Chem Soc*, 2009, 131, 14969-14978.

45.   M. Fabre and J. Bonvoisin, *J Am Chem Soc*, 2007, 129, 1434-1444.

46.   S. N. Semenov, O. Blacque, T. Fox, K. Venkatesan and H. Berke, *J Am Chem Soc*, 2010, 132, 3115-3127.

47.   N. Vila, Y. W. Zhong, J. C. Henderson and H. D. Abruna, *Inorg Chem*, 2010, 49, 796-804.

48.   A. Hildebrandt, D. Schaarschmidt and H. Lang, *Organometallics*, 2011, 30, 556-563.

49.   T. Kundu, B. Sarkar, T. K. Mondal, J. Fiedler, S. M. Mobin, W. Kaim and G. K. Lahiri, *Inorg Chem*, 2010, 49, 6565-6574.

50.   C. J. Yao, Y. W. Zhong and J. N. Yao, *J Am Chem Soc*, 2011, 133, 15697-15706.

51.   C. J. Yao, L. Z. Sui, H. Y. Xie, W. J. Xiao, Y. W. Zhong and J. N. Yao, *Inorg Chem*, 2010, 49, 8347-8350.

52.   S. F. Nelsen, *Chem-Eur J*, 2000, 6, 581-588.

53.   J. Hankache and O. S. Wenger, *Chem Rev*, 2011, 111, 5138-5178.

54.   A. Heckmann and C. Lambert, *Angew Chem Int Edit*, 2012, 51, 326-392.

55.   R. C. Johnson and J. T. Hupp, *J Am Chem Soc*, 2001, 123, 2053-2057.

56.   S. F. Nelsen, D. A. Trieber, R. F. Ismagilov and Y. Teki, *J Am Chem Soc*, 2001, 123, 5684-5694.

57.   S. F. Nelsen and K. P. Schultz, *J Phys Chem A*, 2009, 113, 5324-5332.

58.   N. Gautier, F. Dumur, V. Lloveras, J. Vidal-Gancedo, J. Veciana, C. Rovira and P. Hudhomme, *Angew Chem Int Edit*, 2003, 42, 2765-2768.

59.   J. E. Almlof, M. W. Feyereisen, T. H. Jozefiak and L. L. Miller, *J Am Chem Soc*, 1990, 112, 1206-1214.

60.   S. F. Nelsen, M. N. Weaver and J. P. Telo, *J Am Chem Soc*, 2007, 129, 7036-7043.

61.   S. F. Nelsen, M. N. Weaver, J. I. Zink and J. P. Telo, *J Am Chem Soc*, 2005, 127, 10611-10622.

62.   C. Lambert and G. Noll, *J Am Chem Soc*, 1999, 121, 8434-8442.

63.   G. Zhou, M. Baumgarten and K. Mullen, *J Am Chem Soc*, 2007, 129, 12211-12221.

64.   B. He and O. S. Wenger, *J Am Chem Soc*, 2011, 133, 17027-17036.

65.   Z. J. Ning and H. Tian, *Chem Commun*, 2009, 5483-5495.

66.   J. Cremer, P. Bauerle, M. M. Wienk and R. A. J. Janssen, *Chem Mater*, 2006, 18, 5832-5834.

67.   S. Roquet, A. Cravino, P. Leriche, O. Aleveque, P. Frere and J. Roncali, *J Am Chem Soc*, 2006, 128, 3459-3466.

68.   L. A. Duan, L. D. Hou, T. W. Lee, J. A. Qiao, D. Q. Zhang, G. F. Dong, L. D. Wang and Y. Qiu, *J Mater Chem*, 2010, 20, 6392-6407.

69.   C. W. Chang and G. S. Liou, *J Mater Chem*, 2008, 18, 5638-5646.

70.   M. B. Robin, P. Day, Adv. Inorg. Chem. Radiochem. 1967, 8, 357-390.

71.   B. S. Brunschwig, C. Creutz and N. Sutin, *Chem Soc Rev*, 2002, 31, 168-184.

72.   B. J. Lear, S. D. Glover, J. C. Salsman, C. H. Londergan and C. P. Kubiak, *J Am Chem Soc*, 2007, 129, 12772-12779.

73.   I. Eryazici, C. N. Moorefield and G. R. Newkome, *Chem Rev*, 2008, 108, 1834-1895.

74.   E. C. Constable, *Chem Soc Rev*, 2007, 36, 246-253.

75.   E. A. Medlycott and G. S. Hanan, *Chem Soc Rev*, 2005, 34, 133-142.

76.   E. Baranoff, J. P. Collin, L. Flamigni and J. P. Sauvage, *Chem Soc Rev*, 2004, 33, 147-155.

77.   K. C. D. Robson, B. D. Koivisto, T. J. Gordon, T. Baumgartner and C. P. Berlinguette, *Inorg Chem*, 2010, 49, 5335-5337.

78.   Z. Q. Ji, Y. J. Li, T. M. Pritchett, N. S. Makarov, J. E. Haley, Z. J. Li, M. Drobizhev, A. Rebane and W. F. Sun, *Chem-Eur J*, 2011, 17, 2479-2491.

79.   H. J. Nie, C. J. Yao, J. N. Yao and Y. W. Zhong, *Chem-Asian J*, 2011, 6, 3322-3327.

80.   A. D. Becke, *J Chem Phys*, 1993, 98, 1372-1377.

81.   M. J. Frisch, G. W. Trucks, H. B. Schlegel, G. E. Scuseria, M. A. Robb, J. R. Cheeseman, J. A. Montgomery, T. Vreven Jr., K. N. Kudin, J. C. Burant, J. M. Millam, S. S. Iyengar, J. Tomasi, V. Barone, B. Mennucci, M. Cossi, G. Scalmani, N. Rega, G. A. Petersson, H. Nakatsuji, M. Hada, M. Ehara, K. Toyota, R. Fukuda, J. Hasegawa, M. Ishida, T. Nakajima, Y. Honda, O. Kitao, H. Nakai, M. Klene, X. Li, J. E. Knox, H. P. Hratchian, J. B. Cross, C. Adamo, J. Jaramillo, R. Gomperts, R. E. Stratmann, O. Yazyev, A. J. Austin, R. Cammi, C. Pomelli, J. W. Ochterski, P. Y. Ayala, K. Morokuma, G. A. Voth, P. Salvador, J. J. Dannenberg, V. G. Zakrzewski, S. Dapprich, A. D. Daniels, M. C. Strain, O. Farkas, D. K. Malick, A. D. Rabuck, K. Raghavachari, J. B. Foresman, J. V. Ortiz, Q. Cui, A. G. Baboul, S. Clifford, J. Cioslowski, B. B. Stefanov, G. Liu, A. Liashenko, P. Piskorz, I. Komaromi, R. L. Martin, D. J. Fox, T. Keith, M. A. Al–Laham, C. Y. Peng, A. Nanayakkara, M.

Challacombe, P. M. W. Gill, B. Johnson, W. Chen, M. W. Wong, C. Gonzalez J. A. Pople, Gaussian 09, Revision A.2, Gaussian, Inc., Wallingford CT, 2009.

82.   J. Andzelm, C. Kolmel and A. Klamt, *J Chem Phys*, 1995, 103, 9312-9320.

83.   V. Barone and M. Cossi, *J Phys Chem A*, 1998, 102, 1995-2001.

84.   M. Cossi, N. Rega, G. Scalmani and V. Barone, *J Comput Chem*, 2003, 24, 669-681.

85.   M. Renz, K. Theilacker, C. Lambert and M. Kaupp, *J Am Chem Soc*, 2009, 131, 16292-16302**.**

86.   Y. Sun, N. Ross, S. B. Zhao, K. Huszarik, W. L. Jia, R. Y. Wang, D. Macartney and S. N. Wang, *J Am Chem Soc*, 2007, 129, 7510-7511.

87.   H. J. Nie, J. N. Yao and Y. W. Zhong, *J Org Chem*, 2011, 76, 4771-4775.

88.   J. S. Yang, Y. H. Lin and C. S. Yang, *Org Lett*, 2002, 4, 777-780.

89.   Crystallographic data for 1: C38H34N4O4, M=610.69, orthorhombic,space group Pna2(1), a=15.075(4), b=10.227(3), c=20.695(6) ,a=b=g=908, V=3190.7(16) 3, T=173 K, Z=4, 2602 reflections measured, MoKa radiation (l=0.71073), final R indices R1=0.0694, wR2=0.1316, R indices (all data) R1=0.0779, wR2=0.1362. CCDC 887519 contains the supplementary crystallographic data for compound 1 . These data can be obtained free of charge   from   The   Cambridge   Crystallographic   Data   Centre   via www.ccdc.cam.ac.uk/data_request/cif.

90.   Y. Sun and S. N. Wang, *Inorg Chem*, 2009, 48, 3755-3767.

91. S. Adugna, K. Revunova, B. Djukic, S. I. Gorelsky, H. A. Jenkins and M. T. Lemaire, *Inorg Chem*, 2010, 49, 10183-10190.

92. H. Suzuki, T. Kanbara and T. Yamamoto, *Inorg Chim Acta*, 2004, 357, 4335-4340.

93. H. Y. Li, L. X. Cheng, J. Xiong, L. C. Kang, Q. L. Xu, Y. C. Zhu, Y. M. Tao, Y. X. Zheng, J. L. Zuo and X. Z. You, *Inorg Chim Acta*, 2011, 370, 398-404.

94. M. Matis, P. Rapta, V. Lukes, H. Hartmann and L. Dunsch, *J Phys Chem B*, 2010, 114, 4451-4460.

95. R. Reynolds, L. L. Line and R. F. Nelson, *J Am Chem Soc*, 1974, 96, 1087-1092.

96. Kc=10DE/59 for a room-temperature case. DE=200 mV for compound 1.

97. D. M. D'Alessandro and F. R. Keene, *Dalton T*, 2004, 3950-3954.

98. W. E. Geiger and F. Barriere, *Accounts Chem Res*, 2010, 43, 1030-1039.

99. S. H. Wu, H. D. Abruna and Y. W. Zhong, *Organometallics*, 2012, 31, 1161-1167.

100. T. Koopmans, *Physica* 1934, 1, 104-113.

101. M. A. Ratner, *J Phys Chem-Us*, 1990, 94, 4877-4883.

102. V. Coropceanu, M. Malagoli, J. M. Andre and J. L. Bredas, *J Am Chem Soc*, 2002, 124, 10519-10530.

103. C. Lambert, C. Risko, V. Coropceanu, J. Schelter, S. Amthor, N. E. Gruhn, J. C. Durivage and J. L. Bredas, *J Am Chem Soc*, 2005, 127, 8508-8516.

104. C. Patoux, J. P. Launay, M. Beley, S. Chodorowski-Kimmes, J. P. Collin, S. James and J. P. Sauvage, *J Am Chem Soc*, 1998, 120, 3717-3725.

105. K. Sreenath, T. G. Thomas and K. R. Gopidas, *Org Lett*, 2011, 13, 1134-1137.

106. K. Sreenath, C. V. Suneesh, V. K. R. Kumar and K. R. Gopidas, *J Org Chem*, 2008, 73, 3245-3251.

107. C. Risko, S. Barlow, V. Coropceanu, M. Halik, J. L. Bredas and S. R. Marder, *Chem Commun,* 2003, 194-195.

108. K. D. Demadis, C. M. Hartshorn and T. J. Meyer, *Chem Rev*, 2001, 101, 2655-2685.

109. A. V. Szeghalmi, M. Erdmann, V. Engel, M. Schmitt, S. Amthor, V. Kriegisch, G. Noll, R. Stahl, C. Lambert, D. Leusser, D. Stalke, M. Zabel and J. Popp, *J Am Chem Soc,* 2004, 126, 7834-7845.

110. S. Barlow, C. Risko, V. Coropceanu, N. M. Tucker, S. C. Jones, Z. Levi, V. N. Khrustalev, M. Y. Antipin, T. L. Kinnibrugh, T. Timofeeva, S. R. Marder and J. L. Bredas, *Chem Commun*, 2005, 764-766.

111. N. S. Hush, A. Edgar and J. K. Beattie, *Chem Phys Lett*, 1980, 69, 128-133.

112. K. Lancaster, S. A. Odom, S. C. Jones, S. Thayumanavan, S. R. Marder, J. L. Bredas, V. Coropceanu and S. Barlow, *J Am Chem Soc*, 2009, 131, 1717-1723.

113. B. X. Li, J. S. Chen, Y. B. Zhao, D. Z. Yang and D. G. Ma, *Org Electron*, 2011, 12, 974-979.

114.   C. Li, L. Duan, Y. D. Sun, H. Y. Li and Y. Qiu, *J Phys Chem C*, 2012, 116, 19748-19754.

115.   http://en.wikipedia.org/wiki/Van_der_Waals_force.

116.   S. Olthof, S. Mehraeen, S. K. Mohapatra, S. Barlow, V. Coropceanu, J. L. Bredas, S. R. Marder and A. Kahn, *Phys Rev Lett*, 2012, 109, 1076601.

117.   Chattopadh**y**ay, D. Electronics (fundamentals And Applications), pp. 224–225 (New Age International, New Delhi, 2006).

118.   L. L. Chang, L. Esaki and R. Tsu, *Appl Phys Lett*, 1974, 24, 593-595.

119.   C**.** W. Zhou, J. Kong, E. Yenilmez and H. J. Dai, *Science*, 2000, 290, 1552-1555.

120.   G. Buchs, P. Ruffieux, P. Groning and O. Groning, *Appl Phys Lett*, 2008, 93, 043113.

121.   T. A. Mad**is**on, A. G. Gagorik and G. R. Hutchison, *J Phys Chem C*, 2012, 116, 11852-11858.

122.   J. R. Anderson, D. T. Chiu, R. J. Jackman, O. Cherniavskaya, J. C. McDonald, H. K. Wu, S. H. Whitesides and G. M. Whitesides, *Anal Chem*, 2000, 72, 3158-3164.

123.   P. Paul, A. W. Knoll, F. Holzner and U. Duerig, *Nanotechnology*, 2012, 23, 385307.

124.   I. Y. Y. Bu and T. J. Hsueh, *Sol Energy,* 2012, 86, 1454-1458.

125.   M. D. Hanwell, T. A. Madison and G. R. Hutchison, *J Phys Chem C*, 2010, 114, 20417-20423.

126.   A. G. Gagorik and G. R. Hutchison, *J Phys Chem C*, 2012, 116, 21232-21239.

127.   M. Mottaghi and G. Horowitz, *Org Electron*, 2006, 7, 528-536.

128.   J. S. Jung, E. H. Cho, S. Jo, K. H. Kim, D. H. Choi and J. Joo, *Org Electron*, 2013, 14, 2204-2209.

129.   R. Zeis, T. Siegrist and Ch. Kloc, *Appl Phys Lett*, 2005, 86, 022103.

130.   A. Sastre, P. Bassoul, C. Fretigny, J. Simon, J. P. Roger and T. Thami, *New J Chem*, 1998, 22, 569-578.

131.   J. J. He, G. Benko, F. Korodi, T. Polivka, R. Lomoth, B. Akermark, L. C. Sun, A. Hagfeldt and V. Sundstrom, *J Am Chem Soc*, 2002, 124, 4922-4932.

132.   Z. Bao, A. J. Lovinger and A. Dodabalapur, *Appl Phys Lett*, 1996, 69, 3066-3068.

133.   J. Locklin, K. Shinbo, K. Onishi, F. Kaneko, Z. N. Bao and R. C. Advincula, *Chem Mater*, 2003, 15, 1404-1412.

134**.**   P. Bertoncello and M. Peruffo, *Colloid Surface A*, 2008, 321, 106-112.

135.   W. J. Doherty, R. Friedlein and W. R. Salaneck, *J Phys Chem C*, 2007, 111, 2724-2729.

136.   Z. H. Xu, H. H. Tsai, H. L. Wang and M. Cotlet, *J Phys Chem B*, 2010, 114, 11746-11752.

137.   R. Parashkov, E. Becker, G. Ginev, T. Riedl, H. H. Johannes and W. Kowalsky, *J Appl Phys*, 2004, 95, 1594-1596.

138**.**   Z. N. Bao, Y. Feng, A. Dodabalapur, V. R. Raju and A. J. Lovinger, *Chem Mater*, 1997, 9, 1299-1301.

139. H. Sirringhaus, T. Kawase, R. H. Friend, T. Shimoda, M. Inbasekaran, W. Wu and E. P. Woo, *Science*, 2000, 290, 2123-2126.

140. H. Lee, R. Mensire, R. E. Cohen and M. F. Rubner, *Macromolecules*, 2012, 45, 347-355.

141. P. Bertoncello and M. Peruffo, *Colloids Surf., A*, 2008, 321, 106-112.

142. K. Sugiyama, H. Ishii, Y. Ouchi and K. Seki, *J Appl Phys*, 2000, 87, 295-298.

143. Neil B. McKeown, Phthalocyanine Materials: Synthesis, Structure and Function, Cambridge University Press.

144. http://science.csustan.edu/CHEM1112_4/Diprotic/Diprotic%20inorganic%20acids%20 background%20F09.htm.

145. G. Sauvé and R. D. McCullough, *Adv Mater*, 2007, 19, 1822-1825.